The Effects of Separable Cores on High Power Transformer Design

by

Scott A. Rhodes

Submitted to the Department of Electrical Engineering and Computer Science

in Partial Fulfillment of the Requirements for the Degree of

Master of Engineering in Electrical Engineering and Computer Science

at the Massachusetts Institute of Technology

August 26, 1996

Author _____
Department of Electrical Engineering and Computer Science
August 26, 1996

Certified by _____
James L. Kirtley Jr.
Thesis Supervisor

and by _____
Steven B. Leeb
Thesis Supervisor

Accepted by _____
F.R. Morgenthaler
Chairman, Department Committee on Graduate Theses

The Effects of Separable Cores on High Power Transformer Design

by
Scott A. Rhodes

Submitted to the Department of Electrical Engineering and Computer Science
in Partial Fulfillment of the Requirements for the Degree of
Master of Engineering in Electrical Engineering and Computer Science
at the Massachusetts Institute of Technology

Abstract

The field of transformer design has experienced dramatic growth over the last decade with numerous advances in the area of high frequency, high power inductive energy transfer. However, for one subset of these new applications, traditional design procedures are proving inadequate. The very nature of a transformer with a separable core rules out many of the long-standing techniques used to ensure acceptable performance. The presence of an air gap in the high permeability magnetic path and the inability to interleave the primary and secondary windings have important ramifications on the values of magnetizing and leakage inductances which are realizable. These values in turn affect the parameters which make a product viable, power factor and efficiency. This paper describes an exploration into the fundamental concepts behind a power transformer and the associated conclusions about the design process when a separable core is present.

Thesis Supervisor: James L Kirtley Jr.
Title: Professor of Electrical Engineering

Thesis Supervisor: Steven B. Leeb
Title: Carl Richard Soderberg Assistant Professor in Power Engineering

Acknowledgments

It is with great pride that I put my name on the title page of this thesis as the author. After all, I wrote almost every word in it. However, my tendency is to think of the author as the originator of the work - the explorer, the discoverer, the inventor. Please refrain from reading this thesis with any such misconception. Most of the ideas presented here have been known for some time and were simply waiting for a person to apply them to new designs. Moreover, many of my conclusions would have remained speculative had numerous people been less willing to lend a hand with their experience and time.

My initial source of inspiration with this project was Steve Leeb, who got me involved and provided many of the initial questions which defined the playing field for a year's worth of research. In addition, his willingness at any time to offer advice on problems saved me countless hours of frustration and helped broaden my own perspective. Much the same can be said for Deron Jackson, whose participation in the transformer portion of this project was far more pragmatic than mine. While I was worrying over how to derive the transformer model, Deron was happy if his transformer worked. Surprisingly, this often provided just the type of perspective I needed to keep the project focused. Deron's knowledge of transformer theory also clarified numerous points of confusion and helped me ask the right questions, which was often harder than finding the right answers.

One person in particular allowed me to explore as far as I did, however, and without his help I would probably still be trying to mathematically formulate the various magnetic field models. This individual was my thesis advisor, Jim Kirtley. Although I'm extremely grateful for his input, I have to say that I entered his office more than once with a question about a derivation and left knowing that the derivation which prompted the question was incorrect to begin with. The word invaluable fails to do justice to the assistance he provided over the course of the project.

In the end, I always concluded that I had the right derivation for whatever effect I was analyzing, and this was usually because I had managed to verify the result through some means other than my pen and equations. Numerous methods were utilized to confirm or refute my mathematical results, and each was made possible through the assistance of people in the MIT community with no other reason to help me than simple kindness. Lorenzo Pires and Linda Audin both made life as easy as possible for me, providing access to delicate equipment and lending expertise which allowed me to get the most out of my measurements. In addition, my finite element analysis results were made possible through the countless pieces of advice from Marc Thompson.

On the technical side, this work could not have been accomplished without the generous donations of funding, equipment, and software from Amp, Ansoft, and Intel.

Table of Contents

List of Figures

List of Tables

Symbols

A	Cross sectional area
B	Magnetic flux density
β	Gap ratio
C	Capacitance
d	Depth of core material
δ	Skin depth (magnetic field penetration depth)
ε_0	Permittivity of free space
ε_r	Relative permittivity
ε	Absolute permittivity ($= \varepsilon_0 \cdot \varepsilon_r$)
f	Excitation frequency
Φ	Magnetic flux
g	Air gap between core pieces
g_{w1}	Air gap between conductors in the same winding
g_{w2}	Air gap between primary and secondary winding packs
H	Magnetic field strength
I,i	Current
J	Current density
k	Wave number
L	Inductance
l	Length along a line contour
λ	Flux linkage, wavelength
μ_0	Permeability of free space
μ_r	Relative permeability of a material
μ	Absolute permeability ($= \mu_0 \cdot \mu_r$)
N	Number of turns on a winding
n	turns ratio
R	Resistance
r	Radius
r_i, r_o	Inner radius (next to bobbin), Outer radius (next to side leg of core)
ρ	Resistivity
σ	Conductivity
t	winding conductor thickness
U	Stored magnetic energy
V	Voltage
ω	Angular frequency of excitation (radians per second)
y	Width of windings

Chapter 1

Introduction

Economical inductive power transfer is a technology which has been many years in the making. The simple transformer proved the undoing of Thomas Edison in the 1890's, allowing George Westinghouse's alternating current technology to become the backbone for America's electrical network. The unavailability of power electronics to boost Edison's DC voltages to levels feasible for long-distance transmission wiped out his chances of winning the fight to light up the countryside. As in most areas of technology, however, the world has moved on, and today a race is underway to develop feasible inductive power transfer systems which use both alternating and direct currents to transfer power across high frequency transformers. The challenge is hardly one of making a "better" transformer, however. A standard transformer is one of the most well documented pieces of electronics in existence, and while a complete description of its behavior is non-trivial, a designer has volumes of information at his disposal to help him in his efforts.

What has changed is that recent advances in power electronics have allowed transformers to be used in systems which would have been previously thought ludicrous. Rather than being used simply to step up or down voltage or isolate different parts of a circuit, transformers are now being used to replace metal contact electrical connectors. From robotics[1] to automobiles[2],[3], airplanes[4], and mining[5], inductive power systems are being used in places where designers wish to avoid the issues inherent in the use of a conductive socket. As a result, transformers are appearing which cannot be designed by conventional procedures. For example, splitting the primary and secondary windings into multiple layers and interleaving them is a common technique for improving

transformer performance. Such a technique would be useless to a designer for the Santa Barbara Electric Vehicle Project, which in the late 1980's explored the development of buses capable of being powered from a distributed transformer. While the secondary coils were located on the bottom of the bus, the primary coils were embedded in the roadway, allowing the bus's batteries to maintain their charge as the bus followed its route[6]! Such systems are only now appearing because only recently have economical power electronics been available to boost the operating frequency of power transformers into the kilohertz and megahertz regions. At these higher frequencies, the size of the magnetic core required to make a feasible transformer drops, which not only allows transformers to fit into much smaller spaces, but also makes possible the use of more expensive, high performance core materials. In this sense, the fields of DC and AC electronics have merged, since most inductive power transfer systems take AC wall current, rectify it into DC, and use an inverter to create a high frequency AC waveform. This waveform is fed into the transformer and rectified on the other side.

The advantages of inductive power transfer lie mainly in the areas of safety and system robustness. If power can be received inductively, the electrical interface can be insulated and the risk of electrical shock associated with metal contacts avoided. Also, the absence of mechanical contact between electrical parts reduces long term wear inherent in wires, brushes, and other forms of conductive connections. Finally, as in the case of the Santa Barbara buses, inductive power transfer offers completely new ways of thinking about the supply of power to industrial systems. Of course, these advantages come at a price. Unlike the electrical power cord, inductive systems require expensive power electronics which need digital control systems to function properly. Also, the transformers in many of the inductive power transfer systems suffer from poor performance due to the physical constraints placed on them. Finally, transformers have

been designed for many years using assumptions and design procedures which simply do not hold true for the newer systems.

The Santa Barbara bus system is an extreme case of the type of transformer which will be analyzed in this study. As in that system, the transformers in this study have magnetic cores which are divided into two pieces so that the primary can be physically separated from the secondary, although the air gaps in the systems examined here will not be as large. The physical constraints due to a separable core and the electrical effects of high frequency operation combine to make a quantitative picture of such systems very difficult to obtain and provide the motivation for the work presented here. The fundamental question which will be explored throughout this paper is how to build a separable core transformer. In some areas, the discussion will follow traditional transformer analysis quite closely, but in others the treatment will be very specific to this type of transformer.

First and foremost, it is important to gain an understanding of what makes a high frequency separable core transformer different from more traditional versions From a circuit perspective, a separable core transformer is no different from any other, and to this end, the various electrical parameters which are included in the standard model will be examined in Chapter 2 for the separable core case. Chapter 3 describes engineering considerations which must be taken into account in the design process, most notably modeling issues and high frequency effects. Chapter 5 introduces results from laboratory prototype transformers, so Chapter 4 first describes some of the pitfalls encountered while working in the lab. Numerous puzzling results were encountered throughout this work which were simply due to errors in experimental procedure. Chapter 4 is included in the hope that readers who would otherwise have been caught as well will be forewarned. Having covered all the parameters which comprise the electrical circuit

abstraction of a non-ideal transformer, Chapter 5 compares different ways in which a transformer can be physically constructed. Specifically, foil conductors can be used to reduce leakage inductance in separable core transformers, and Chapter 5 examines the effects of four ways of winding the foil around the core. It also presents computer simulation results and empirical measurements from laboratory prototypes corresponding to each of the four types. Very few inductive power transfer systems are actually at the point of commercial feasibility at this time, but there is one notable exception. General Motor's recently introduced EV-1 (developed as the Impact) uses an inductively coupled system to charge its battery at power levels up to 6.1 kilowatts. In addition, developers in conjunction with the General Motors effort have published information relating to a larger version of the same coupler capable of charging rates up to 120 kW[2]. Since [7] describes a 120 kW IGBT converter designed specifically for supplying power to the larger system, it seems likely that the 120 kW system is close to marketability, despite the fact that batteries may not currently exist which can receive power at 120 kW. The 6.1 kW system will be examined and some of the issues related to commercial feasibility explored.

Considering the varied physical constraints which are imposed upon separable core inductive power transfer systems, it is not possible to claim that the transformer parameter derivations given in this paper will hold for geometries other than the ones examined. In addition, important topics such as harmonic effects and the distribution of magnetizing and load currents between primary and secondary windings have been omitted entirely. Hopefully, the conditions examined will minimize the errors due to the omission of these effects. Transformer development will never be a straightforward venture, but as each new application emerges, it should be possible to quantify the criteria which are most necessary for a good design in each field.

Chapter 2

Transformer Models

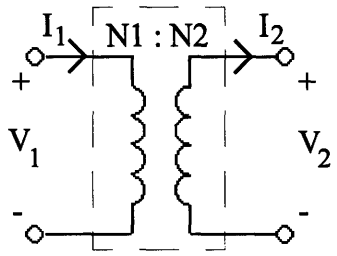

Figure 2.1: Ideal Transformer Circuit

The ideal transformer depicted in Figure 2.1 represents a hypothetical, lossless device that modifies the form in which power in a circuit is transferred. Using Faraday's law of induction, an ideal transformer modifies the voltage and current levels passing through the two terminal device according to the turns ratio, mathematically expressed as

$$\frac{V_2}{V_1} = \frac{N_2}{N_1} \qquad \textit{and} \qquad \frac{I_2}{I_1} = \frac{N_1}{N_2}. \tag{2-1}$$

Notice that these equations conserve power, since

$$V_1 \cdot I_1 = V_2 \cdot I_2. \tag{2-2}$$

In an ideal world, the voltage waveform applied to the primary winding determines a flux linkage which is perfectly coupled to the secondary winding. Varying the primary voltage as a function of time induces a voltage in the secondary, where the amplitude of the induced voltage depends on the number of primary and secondary turns which determine how many times the mutual flux is linked on each side. Circuit designers would be happy to rely on this input/output relationship, but the real world is rarely so

simple. Rather than retreat to Maxwell's equations and electromagnetic field theory to describe a transformer, however, engineers have found it more convenient to add electrical circuit elements to the ideal model to account for the various non-idealities present in actual systems. The results can be so complicated that just analyzing the transformer is a challenge.

A standard equivalent circuit model for a real transformer is provided by the American National Standards Institute in conjunction with the IEEE in standards document 390, "IEEE Standard for Pulse Transformers" [8]. This model is shown in Figure 2.2 and is far more complex than the simple, turns ratio-controlled model of the ideal transformer. Using the full IEEE model is not always necessary, however, and it is up to the system designer to determine which, if any, of the elements may be omitted.

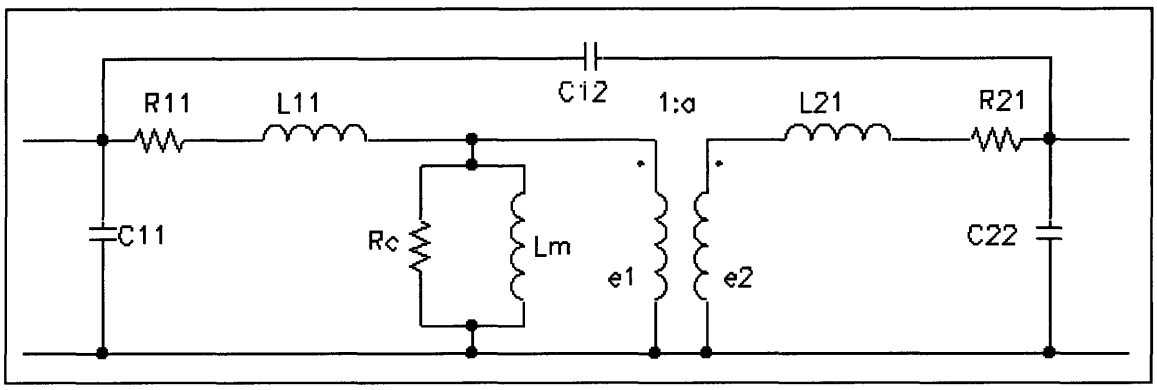

Figure 2.2: IEEE Equivalent Circuit Model for a Pulse Transformer

The additional features which appear in this model are the magnetizing and leakage inductances, the core and winding losses, and the interwinding capacitances. In order to decide which elements are necessary in any given analysis, their physical origins and relative importances must be understood. More comprehensive treatments of these issues can be found in a number of sources such as [9] and [10] but the descriptions here should

furnish a qualitative understanding and a sense of how the elements are affected by the presence of a separable core.

2.1 Core Geometry

It is convenient at this point to mention that there are a number of possible choices for the core geometry in a transformer. The core shape chosen affects many of the parameters of the transformer model as well as the methods used to calculate them. In this study, core geometries will be restricted to what is known as "shell" type, where there are multiple magnetic paths, and in general the windings are surrounded by core material. Another main type is called "core" type, which contains only one magnetic path. Examples of both are illustrated in Figure 2.3. Note that the restriction to shell type cores still leaves ample room for different geometries, such as E cores (Figure 2.3a) and pot cores (Figure 2.3b).

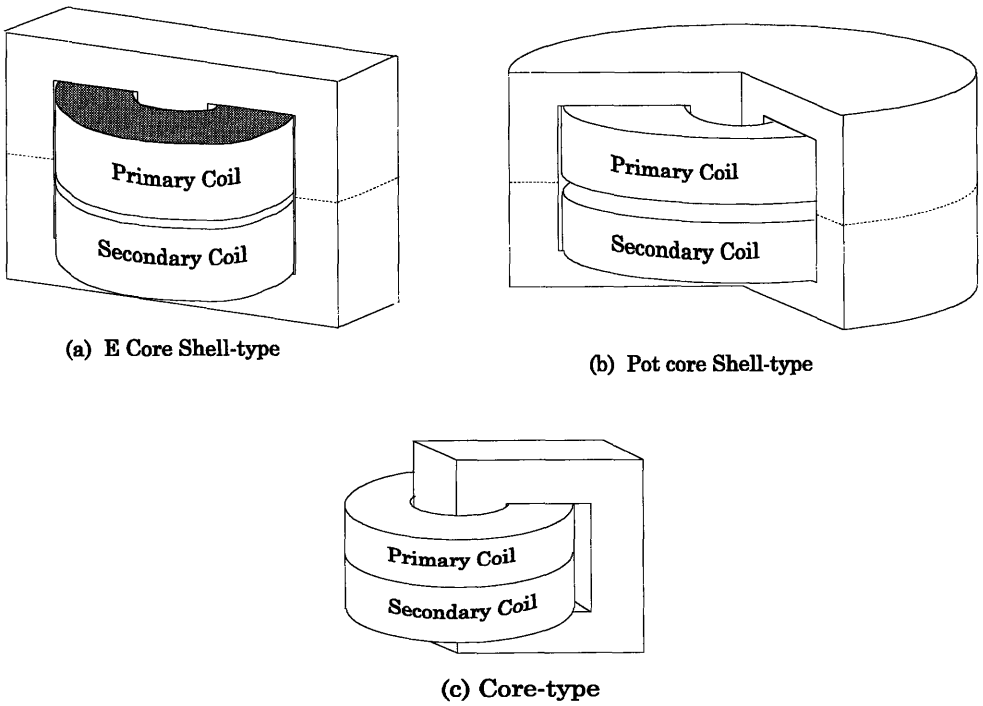

Figure 2.3: Shell and Core Type Transformers

2.2 Magnetizing Inductance

According to the ideal transformer model, no current should flow in the primary winding if the secondary winding is open-circuited, even if the primary has a voltage across it, but a quick measurement on any real transformer will show that this is not the case. This departure from ideality arises from the finite permeability of the core. If the value were infinite in magnitude, an infinitesimally small current in the primary would cause a finite magnetic flux in the core, and, by Faraday's law, the time rate of change in this flux density would induce the secondary voltage. With finite permeability, however, a finite level of magnetic flux density in the core requires a finite magnetic field and a finite primary current. This phenomenon is incorporated into the model as a shunt inductance.

In a shell type core, the magnetizing inductance can be approximated from a determination of the flux passing through the center core leg. This is justifiable because the magnetizing inductance is equivalent to the mutual inductance reflected to one side of the transformer, and the flux passing through the center core leg is linked by both sets of windings. As with the determination of many of the transformer model elements, the accuracy of this calculation depends on the person performing the analysis. One of the simplest methods of deriving the magnetizing inductance will be described first here, and then additional considerations will be taken into account to improve the results.

2.2.1 Derivation without an Air Gap

The quickest approximation of the magnetizing inductance uses the formula

$$\lambda = Li \tag{2-3}$$

where λ is the flux passing through the center leg linked by the number of primary turns. Thus, the flux linkage can also be expressed as

$$\lambda = N_1\Phi = N_1BA \tag{2-4}$$

where B is the flux density through any given cross-section of the center leg (assumed to be uniform), and A is the cross-sectional area of the leg. For cores with no air gap, calculation of the flux density is straightforward using Ampere's law in integral form. Assuming uniform fields throughout the core material, the flux density is

$$B_{core} = \frac{\mu_r \mu_0 N_1 I_1}{l_{core}} \tag{2-5}$$

making the magnetizing inductance equal to

$$L_{mag} = \frac{\mu_r \mu_0 N_1^2 A_{core}}{l_{core}}. \tag{2-6}$$

The flux density equation above has been derived assuming the permeability to be constant. This simplification replaces the well-known hysteresis characteristic of the magnetization curve for the core with a linear relationship between magnetic field strength and magnetic flux density. In reality, non-uniform magnetic field strength throughout the core can cause the non-linear magnetization characteristic to become important under certain conditions.

2.2.2 Derivation with an Air Gap

If an air gap is present in the core, the analysis is made considerably more complicated. As will be shown, however, an air gap has the useful side effect of stabilizing the magnetizing inductance by removing its dependence on the core permeability. Assume the core material to be a ferrite, for example a Manganese-Zinc (MnZn) combination, with relative permeability around 2000. Examining a cross-section of the gapped core in Figure 2.4, evaluation of Ampere's integral law along the contour shown yields the formula

$$H_{gap1} l_{gap1} + H_{gap2} l_{gap2} + H_{core} l_{core} + H_{puck} l_{puck} = N_1 I_1 \tag{2-7}$$

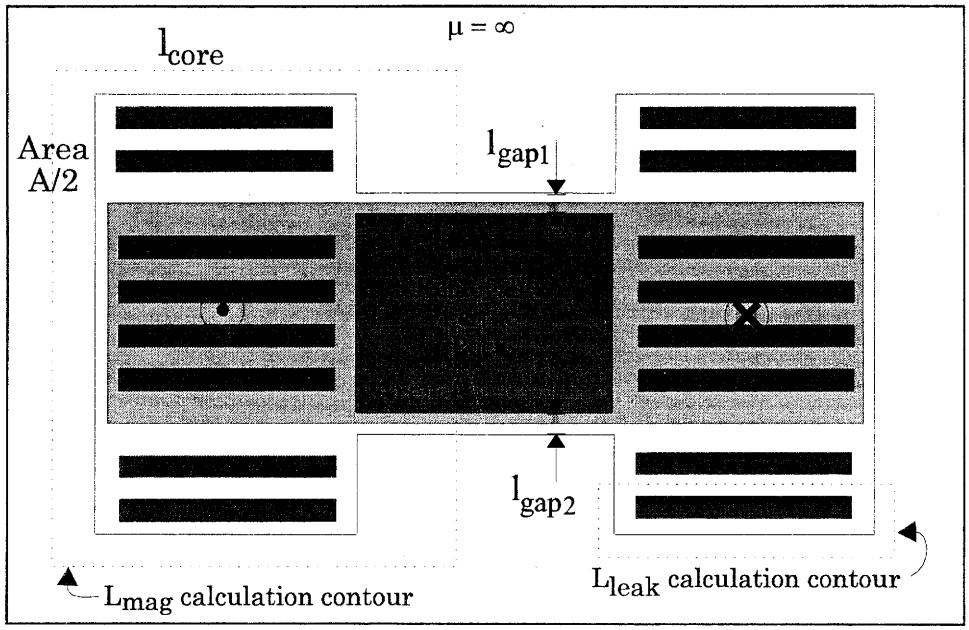

Figure 2.4: Gapped Core for Lmag Calculation

with the assumptions that the magnetic fields are uniform for the length of each section. Conservation of flux shows that the magnetic fields in both gaps are equivalent, and assuming that the center leg area is twice the area of each side leg, the magnetic field in the removable ferrite puck is the same as in the main core as well. This reduces the formula to

$$2H_{gap}l_{gap} + H_{core}(l_{core} + l_{puck}) = N_1 I_1. \qquad (2\text{-}8)$$

Finally, conservation of magnetic flux can be used to show that the ratio of the magnetic fields in the two materials (air and ferrite) is set by the ratio of their permeabilities according to the formula

$$B_{core} = \mu_{core}H_{core} = \mu_0 H_{gap} = B_{gap}. \qquad (2\text{-}9)$$

Since the permeability of the core is so much larger than that of air, it can be approximated that all the magnetic field is concentrated in the air gap. It is interesting to note that this simplification is equivalent to returning to the case where the core

permeability is assumed to be infinite, but the transformer is no longer ideal because of the air gap in the magnetic circuit. Thus, the total flux passing through the center leg of the core can now be calculated to be

$$\Phi = \frac{\mu_0 N_1 I_1 A}{2l_{gap}} \tag{2-10}$$

and the magnetizing inductance of the transformer becomes

$$L_{mag} = \frac{\mu_0 N_1^2 A}{l_{total\ gap}}. \tag{2-11}$$

The relative permeability of the core no longer affects the magnetizing inductance, which now depends on the length of the combined air gap. Considering the natural variations in permeability between different cores and the fact that even a single core's permeability will change slowly over time shows the usefulness of a gapped transformer design when stability is needed. The drawback of this approach is the corresponding reduction in the magnetizing inductance which removes the transformer even further from the ideal.

Realize that this value has been calculated from the perspective of the primary winding but does not have to be. Since the flux in the center leg is coupled to both windings, it can be calculated from the perspective of the secondary just as easily by replacing the number of primary turns in the formula with the number of secondary turns. This quantity can also be expressed as a mutual inductance

$$L_{mutual} = \frac{\mu_0 N_1 N_2 A}{l_{total\ gap}} \tag{2-12}$$

which can be reflected to either side of the transformer by multiplying or dividing by the turns ratio. As might be expected by its name, the mutual inductance expresses how much flux linkage will be induced in one winding by a current in the other.

2.2.3 Hazards of Large Cores and Small Air Gaps

There are a number of pitfalls with this approach to magnetizing inductance calculation. However, the likelihood of inaccuracies due to most of them are easily checked, and some are simple to incorporate into the model if higher precision is required. The first deals with the assumption of a zero-reluctance core, which restricts the magnetic field to the air gap. Reviewing (2-9), it is possible to see that the magnetic field in the core is not zero, but simply very small. Looking back at (2-8) reveals that it is possible for this small field to have a noticeable effect on the gap field if the length of the magnetic path through the core material is large. This type of error can be avoided while returning to the simpler non-gapped analysis at the same time by introducing the concept of effective permeability, defined by [11][1] as

$$\mu_e = \frac{\mu}{1+\mu\beta} \tag{2-13}$$

where the gap ratio is most simply defined to be $\beta = l_{total\,gap} / l_{core}$. Using the effective permeability, the magnetizing inductance is calculated as if no gap existed, and the length used is simply the average magnetic path length within the core material.

2.2.4 Fringing Effects along Air Gaps

The previous discussion brought up two issues which affect the magnetizing inductance even in small cores, the issues of fringing fluxes and non-uniform flux density. Unlike the ferrite portion of the center leg, the air gap has no clear boundary to define its cross-sectional area. When flux leaves the core and enters the low permeability area of the air gap, it spreads out before being trapped again by the core on the other side of the gap. This increases the effective cross-sectional area of the air gap which increases

[1] p. 133.

the magnetizing inductance. The amount of increase depends on such factors as the geometry of the contour, the length of the gap, and the actual cross-sectional area. For a given area with parallel faces, fringing is negligible for very short gap lengths, growing larger with increasing gap length. [10] suggests[2] increasing both dimensions of the cross-sectional area by one gap length to get a reasonable approximation for the effective area.

2.2.5 Reluctance and its Effects on Flux Distribution

In addition, all of the equations used so far have assumed that flux densities were uniform over the areas of interest, which is rarely the case. To see why, it is convenient to introduce the concept of magnetic reluctance, an abstraction which could have been used previously to derive the magnetizing inductance as well but is particularly effective here. Just as currents in purely resistive electrical circuits are calculated using network theory, flux can be calculated using network theory in a magnetic circuit. Instead of an electro-motive force of voltage, a magneto-motive force of ampere-turns is used, and instead of resistances, quantities called reluctances determine how much flux flows through various paths of the magnetic circuit. The formulation of a magnetic circuit is a direct analog of the electric circuit, however, and magnetic reluctances are a direct companion to electrical resistances. The electrical resistance and magnetic reluctance of a given volume of uniform material can be expressed as

$$R \equiv \frac{length}{\sigma \cdot Area} \qquad \text{and} \qquad \Re \equiv \frac{length}{\mu \cdot Area} \qquad \text{(2-14a,b)}$$

where the magnetic permeability, μ, is the direct analog of the electrical conductivity, σ. The reason magnetic materials cannot be modeled as simply as electrical resistors comes down to nothing more than the orders of magnitude involved in the two cases. While the

---

[2]p. 69.

difference in conductivity between a good electrical conductor and a good electrical insulator can be as much as 10^{20}, the difference between the permeability of an excellent ferromagnetic material and the permeability of free space is at most around 100,000. In comparing the two situations, it has been said that there are no magnetic insulators[9, p.7]. Considering that the permeability of free space corresponds to a lack of any magnetization at all (and considering diamagnetism to be a dead end), a more pragmatic statement might be that there are no real magnetic conductors!

Thinking of a magnetic material in terms of its reluctance, consider the difference between the effective path length for magnetic flux along the outer surface of the core versus the inner surface. In the electrical domain, a voltage potential placed across the core, for example with the positive terminal along one surface of the air gap and the negative terminal along the other, would cause less current to flow through the longer path than the shorter one. In the same way, the magnetic flux crowds to the inside of the magnetic core because of the lower reluctance of the inner path. Geometric effects such as this cause unwanted dissipation, leading to "hot spots." As would be expected, geometric effects increase with the core size due to the increasing difference between parallel path lengths.

Thus, there are a number of effects which are ignored in the treatment from Section 2.2.2. However, most are relatively small in comparison to the value derived from the simplistic, initial approach, and their importances are easily assessed with quick measurements of the core dimensions. Other effects which modify the magnetizing inductance, such as the level of flux density, temperature, and frequency of excitation, are not as simple to monitor and will be discussed in Chapter 3.

2.3 Leakage Inductance

Leakage inductance is another real world phenomenon which is incorporated into almost all equivalent circuit models for transformers. Thinking in graphical terms, leakage inductance is a measure of the number of primary flux lines which fail to couple to the secondary, and vice versa. It is a statement that even without any dissipative losses, not all of the voltage applied to the primary is transferred to the secondary terminals. Note that to be completely accurate, a leakage inductance must be referenced to two windings since it is a measurement of flux which links one winding but not another. For a transformer with more than two windings, different amounts of the leakage flux exist between each pair of terminals. However, in the case of a two-winding transformer, the assumption is that the primary leakage inductance is measured with reference to the secondary, and vice versa.

2.3.1 Leakage and the Equivalent Circuit Model

Analysis of the leakage inductance can be done in a number of ways. A useful way to start is to examine a simplified equivalent transformer (with unity turns ratio), such as the one in Figure 2.5, to see the effects of leakage inductance.

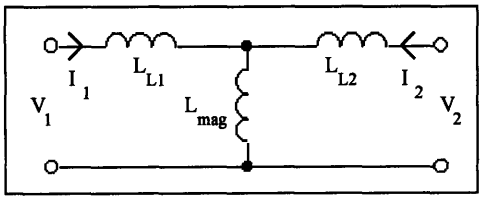

Figure 2.5: Simplified Equivalent Transformer

First notice that the primary leakage inductance and the magnetizing inductance form an impedance divider, even when no current flows in the secondary. This is exactly what was predicted at the beginning of this section. Next, notice what happens when both the primary and secondary are driven with equal and opposite currents. All of the current

flows from the primary terminals straight into the secondary, bypassing the magnetizing inductance completely. This agrees with the model that if equal and opposite currents are applied to two windings around the same core, the net number of ampere turns will be zero and no flux should be present in the core. However, the current flowing through the leakage inductances stores magnetic energy, and by estimating this energy, the value of the inductances can be calculated. To a first approximation, any fields in a system under equal and opposite excitation are not coupled and therefore can be counted as leakage.

A two port circuit equation describing Figure 2.5 quantifies this description. Using impedances to relate voltages and currents yields the relation

$$\begin{bmatrix} V_1 \\ V_2 \end{bmatrix} = \begin{bmatrix} (L_{L1} + L_{mag})s & L_{mag}s \\ L_{mag}s & (L_{L2} + L_{mag})s \end{bmatrix} \begin{bmatrix} I_1 \\ I_2 \end{bmatrix} \tag{2-15}$$

which can be converted into an inductance matrix relating currents and flux linkages:

$$\begin{bmatrix} \lambda_1 \\ \lambda_2 \end{bmatrix} = \begin{bmatrix} L_{L1} + L_{mag} & L_{mag} \\ L_{mag} & L_{L2} + L_{mag} \end{bmatrix} \begin{bmatrix} I_1 \\ I_2 \end{bmatrix}. \tag{2-16}$$

This matrix will be useful in Chapter 5. For situations where the turns ratio is non-unity, the inductances must be reflected to the correct sides of the transformer to produce

$$\begin{bmatrix} \lambda_1 \\ \lambda_2 \end{bmatrix} = \begin{bmatrix} L_{L1} + L_{mag} & \frac{L_{mag}}{n} \\ \frac{L_{mag}}{n} & L_{L2} + \frac{L_{mag}}{n^2} \end{bmatrix} \begin{bmatrix} I_1 \\ I_2 \end{bmatrix} \tag{2-17}$$

where the turns ratio here is n:1.

2.3.2 Field Theory and Leakage Inductance

Keeping these results in mind, the next step is to use field theory to develop a picture of a transformer system under equal and opposite excitation. Even with a core of infinite permeability, leakage flux must be present to satisfy Ampere's law. Examining Figure 2.4 again, notice that a contour can be drawn around the bottom secondary

winding, with all segments of the contour except the interwinding distance contained within the core. Assuming the core has infinite permeability and the magnetic field within the interwinding space to be uniform, the value of the field will be

$$H_{winding\_space} = \frac{I_2}{y}, \tag{2-18}$$

where y is the distance the field travels in the interwinding space. Similar contours can be drawn to pass through each of the interwinding spaces, and the resulting equations solved for the interwinding fields. Because these fields fail to couple all of the conductors from both the primary and secondary windings, they correspond to leakage flux, and therefore leakage inductance. There are at least two ways to calculate the leakage inductance from these fields. [12][3] and [10][4] calculate the total stored magnetic energy in these fields using the relation

$$U_m = \int_V \tfrac{1}{2}\mu_0 H^2 dv = \tfrac{1}{2} L_{eq} i^2 \tag{2-19}$$

to determine the total equivalent leakage inductance. This is the value obtained from the sum of both leakages reflected to the same side of the ideal transformer. In general, on the primary side, this value corresponds to

$$L_{total\_P} = L_{Lp} + n^2 L_{Ls} \tag{2-20}$$

where n is the turns ratio. Notice that for a unity turns ratio transformer with equivalent primary and secondary windings, the total equivalent leakage inductance is simply twice the leakage value of either side. [9][5] uses a slightly different method to arrive at the same result. He first calculates the flux in each of the interwinding spaces (which can be

---

[3]pp. 176-178.
[4]pp. 358-362.
[5]pp. 172-174.

equivalently derived from the magnetic fields as above or as he does from reluctance calculations). Then he adjusts for the fact that much of the leakage flux only partially links one or both of the windings, finding the equivalent flux which would link all of the primary and none of the secondary (and vice versa). Referring these to one side, he multiplies by the corresponding number of turns to find the total flux linkage and divides by the excitation current to find the equivalent leakage inductance. The results are identical to those derived from the previous calculations.

2.3.3 Reduction of Leakage Inductance

Reduction of leakage inductance is an important goal when air gaps are present in the magnetic core because the reduced magnetizing inductance exacerbates the voltage regulation problem as well as lowering the power factor of the system. A natural question, then, is what types of design modifications will lower leakage inductances. The most common means for doing this is to interleave the windings. With this technique, every conductor in the primary is in close proximity to a conductor of the secondary, maximizing coupling. Another way to view the strategy is that under equal and opposite current excitation, very few flux contours surround more than one net ampere. This minimizes the interwinding space magnetic fields and therefore the stored magnetic energy as well. Actually interleaving *every* conductor is rarely done because of the cost of insulating the primary from the secondary, but the optimal level of interleaving is still quite effective at reducing leakage inductance. When interleaving is not possible, such as the case where the primary must be physically separable from the secondary, it becomes worthwhile to examine other types of winding geometries to see if any can approach the type of leakage reduction seen through interleaving. A comparative analysis is presented for foil windings in Chapter 5. The conclusion is that there are three basic ways to reduce leakage. First, the leakage inductance is directly proportional to the volume of the

interwinding spaces, so reduce the distance between conductors whenever possible, especially between the primary and secondary winding packs. Unfortunately, this can come into conflict with the need to insulate the windings and therefore has limited practicality. The second method is to increase the width of the windings. This will cost more in terms of copper used, but the winding width is inversely proportional to the effective leakage inductance. The final method is to split one winding into two portions connected in series, and physically sandwich the other winding between the two halves. While this is effectively just a simpler attempt to interleave the windings it still has the largest impact of the three methods due to the quadratic nature of the dependence in this case.

Changes in the length of the air gap, while having an enormous effect on the magnetizing inductance, have almost no impact on the leakage inductance, explained by the lack of leakage flux in the center core leg. Also, the question arises whether it is better to have fewer or more turns on the transformer. Unfortunately, this question cannot be simply answered because the impact of the leakage and magnetizing inductances depends as much on how the transformer is used as their values. Often, the voltage regulation due to the impedance divider between them causes their ratio to matter more than the absolute value of either one. On the other hand, a resonant design can effectively eliminate the primary leakage altogether, making the value of the magnetizing inductance important. This question is considered further in Section 3.5.

2.4 Copper Losses: Winding Resistances

The series resistances in the IEEE model are due to the resistance of the windings, so one resistor appears on each side of the ideal transformer in the model. If the system of interest operates at only one frequency, the resistor values are constant, but if the system is multi-frequency, the skin effect can restrict the current to the outsides of the

conductors as the frequency increases, causing a nonlinear increase in winding resistance. Traditional transformers, which use many turns of solid wire, usually approximate the winding resistance based on the estimated length of wire and the resistance of the wire gage used. Nonlinear resistance is not a concern in such systems because of their low operating frequency. In this study, transformers with only a few windings will be used, but the windings will be made of foil copper, which complicates the calculation of resistance. Approximations of these resistances are derived from the dimensions and geometry of the windings in Section 3.4.

2.5 Core Losses

Core losses appear in the IEEE standard transformer model as a shunt resistor across the magnetizing inductance. This element is the result of the core's finite resistivity as well as the hysteresis losses in the magnetic material. The hysteresis losses are due to the B-H profiles of all cores' magnetization characteristics, which are not only non-linear, but exhibit hysteresis behavior for a varying applied H field. Unfortunately, material properties differ enough to prevent a universal formula for hysteresis loss. Various models have been proposed based on empirical measurements, but as core technologies improve, limitations in the formulas have been found [9]. The origin of the losses, however, is easily understood. The enclosed area in the magnetization curve is proportional to the energy lost over one oscillation of the H field, so the hysteresis losses are proportional to frequency, and because the loss is due to the magnetizing and demagnetizing of each core molecule, it is also proportional to core volume.

The resistivity of the core has two effects which can be important. Both arise from the fact that the changing magnetic flux in the finite resistivity core induces eddy currents in the same way as the skin effect in a conductor is caused by eddy currents due to the changing magnetic field from the source current. The first result of these eddy

currents in the magnetic material is power dissipation that is a function of the resistivity, the frequency of excitation, and the core geometry. Eddy current losses can be calculated by dividing the cross-section of the core into parallel resistive paths, determining the voltage induced in each and the resistance of the path, and using Ohm's law to find the power dissipation. An example of this for a laminated core geometry is presented in [9], and the treatment can be easily extended to any core geometry.

The second result of eddy currents in the core is the presence of magnetic shielding. Similar to the more familiar skin effect in conductors, shielding causes the magnetic flux to be attenuated toward the center of the core. Not only does this complicate the calculation of core losses since the voltages causing the eddy currents in the center are attenuated as well, but the magnetizing inductance of the transformer is reduced as well. This phenomenon is explored further in Section 3.3.

Because of the material and geometry dependent nature of these calculations, theoretical derivations for core losses are rarely very useful because of their limited validity. When appropriate, core manufacturer's listed core loss volume density values can be used to estimate the dissipation. The most common method of determining the value for any given system, however, is still to measure the losses empirically.

2.6 Parasitic Capacitances

Whenever there is a voltage difference between two charge carrying materials, there must be an associated capacitance, and the windings of a transformer are no exception. Parasitic capacitances exist between the turns of each winding as well as between the primary and secondary windings. Further, foil windings increase this capacitance by enlarging the area of the conductors and making the windings look like parallel plates. For a four-turn primary carrying 400 volts, the potential difference between two of the flat conductors will be 100 volts, and since the turns are separated

only by a thin layer of insulation, the capacitance in the system is significant. The distance of separation is of importance because a reduction in interwinding space will not only reduce the leakage inductance but increase the capacitance. This tradeoff is well known, leading to the suggestion that often it is not the leakage inductance or the capacitance which is most important to minimize, but some combination of the two [11, p. 229].

2.7 Formulation of a Useful Transformer Model

The only circuit element which will be ignored from the IEEE model is C_{12}, the parasitic capacitance between the two sets of transformer windings. The other parasitic capacitances were determined for the prototype systems through nonlinear regression on impedance measurements and begin to have noticeable effects above 100 kHz. When C_{12} was present in the model, the curve fit reported its value as being around 0.01 picoFarads, far below the level that it would be significant. Interestingly enough, the IEEE's analysis also ignores this element, assuming it to be negligible. The other parasitic capacitances in the model are also negligible over the frequencies of operation, but become significant near one MHz. The same result holds true for the shunt resistor representing core losses. For the values present in the prototype transformers, the core loss is negligible at frequencies below 100 kHz, and starts to become significant around one MHz. Since a driving waveform at 100 kHz can have significant harmonics near one MHz, all elements except the mutual parasitic capacitance C_{12} will be included in the model. It is reasonable, however, to omit the shunt resistance and parasitic capacitances when analyzing waveforms at or below 100 kHz (see Appendix E for comparisons). This yields the equivalent circuit model shown in Figure 2.6.

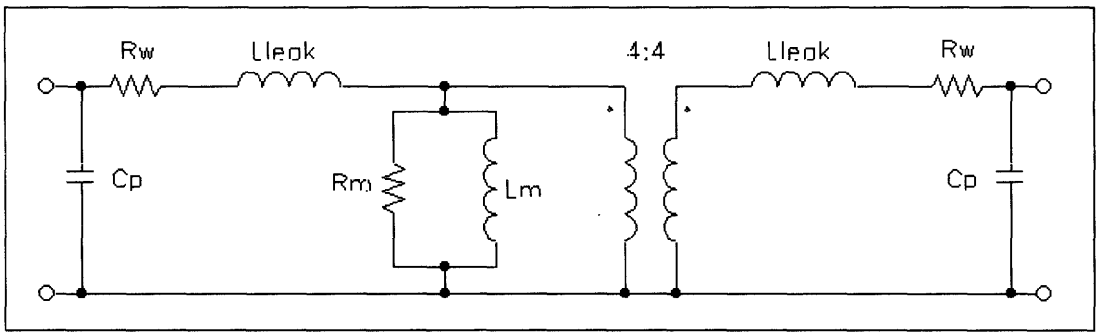

Figure 2.6: Simplified Standard Transformer Model

Whenever possible, measured or computer generated values will be compared to theoretically calculated values to verify accuracy.

Chapter 3

Engineering Considerations

Armed with an understanding of the origin of the electrical components in a non-ideal transformer, the system designer must then determine how various choices of core and winding geometries will affect the electrical characteristics of the system. In addition, the designer needs to understand how the model relates to the performance parameters of interest. Only with both levels of understanding present will the full effect of any given physical change in the system be clear.

3.1 Electrical Models of Non-ideal Transformers

The first engineering consideration which needs to be taken into account is the fact that not all transformer applications will use the standard IEEE equivalent circuit, or even a simplified version of it for the transformer model. The most frequently seen alternative to the "T" model is some form of an "L" model, which receives its name because the leakage inductance appears only on one side.

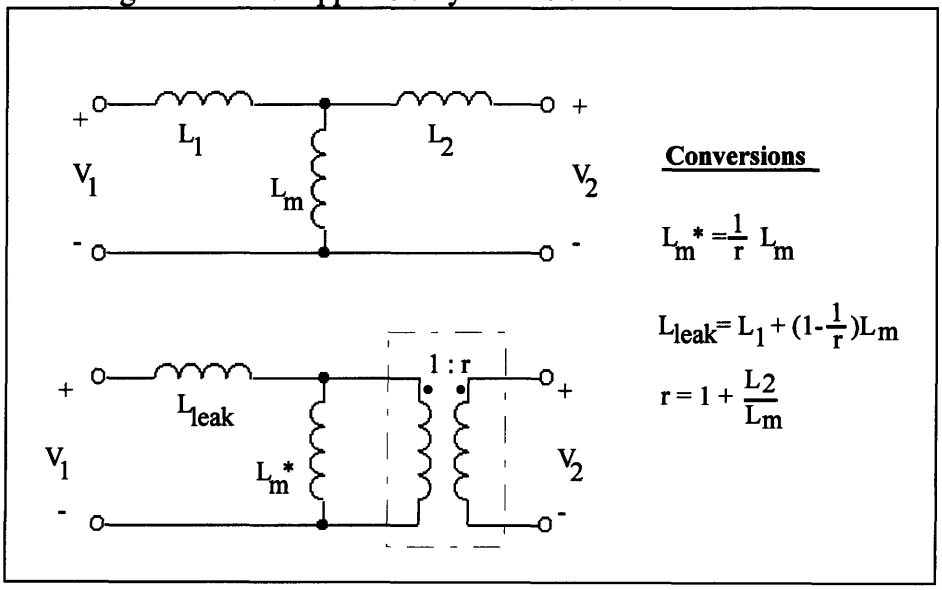

Figure 3.1: Equivalent Circuit Models - "T" and "L" Topologies

[13] demonstrates the equivalence of the inductive components of the "T" and "L" models, and provides the corresponding transformation which is shown in Figure 3.1. The transformation is based on the mathematical equivalence of the two port impedance matrices and is made possible by allowing the turns ratio to be a variable in the conversion. If the "T" model incorporates a turns ratios of 1:n, the conversion formulas must be altered to

$$r = n + \frac{L_2}{nL_m} \qquad L_m^* = \frac{n}{r} L_m \qquad L_{leak} = L_1 + L_m(1 - \frac{n}{r})$$

The result of this conversion is a cautious statement of equivalence between the two models. Using the transformation, it is possible to characterize a given transformer with either topology and then convert the model to the other topology. The most significant pitfall of the conversion is the tendency to claim the equivalence of "T" and "L" circuit models with the same turns ratio. For a unity turns-ratio "T" modeled system with a very small leakage to magnetizing inductance ratio, the equivalent "L" model essentially just ignores the secondary leakage. However, for large leakage values, the equivalent "L" model no longer has a unity turns-ratio. Note also that the equivalence of the two circuit models does not extend to the resistive or capacitive components from the IEEE model. Both the primary and secondary winding resistances must keep their positions on either side of the magnetizing inductance, although either one can be reflected through the ideal transformer portion of the model.

While the equivalence of the two topologies suggests that choice of model is simply one of personal preference, the use of the turns ratio in the conversion and the inability to completely reflect the winding resistances to the other side of the magnetizing inductance identify the "T" model as the more physically realistic circuit. For this reason, all modeling in this paper will utilize the IEEE based "T" model.

3.2 Parameter Estimation in the Lab

Using the working, simplified "T" model derived in Chapter 2, a reasonable question to ask would be whether it is possible to estimate the values of the major parameters based on a few simple tests on a transformer in the laboratory. The answer is yes, provided the parameters are "well-behaved." To explain the meaning of this qualification, consider the modeling reasons behind the inductive elements in the non-ideal transformer model. The magnetizing inductance is present because of the inevitable presence of stored magnetic energy in the transformer and the leakage inductances model the imperfect coupling between the primary and secondary windings. As the transformer approaches the ideal case, the leakage inductances shrink and the magnetizing inductance grows. Thus, the parameters in a transformer can be termed "well-behaved" to the extent that they approach the model of an ideal transformer. This is significant because the parameters in a well-behaved transformer can be estimated at a glance, but in a very non-ideal transformer, much more work is necessary.

To estimate the values of the magnetizing and leakage inductances, assume that all impedance measurements are taken at frequencies where capacitive effects are negligible. In the case where the transformer parameters are well-behaved, the leakage inductances are negligible when compared to the magnetizing inductance. Thus, with the secondary terminal short-circuited, the reactance measured is essentially just the sum of the primary leakage inductance and the secondary inductance reflected to the primary side. For a unity turns ratio system, the leakage inductances will be very similar, and their values can be estimated to be half the short-circuit reactance. With the secondary terminal open-circuited, the reactance measured will be the sum of the primary leakage inductance and the magnetizing inductance, and since the leakage inductance is already

known, the magnetizing value is easily calculated. These quick calculations are summarized as follows

$$\begin{aligned} L_{short} &= 2\, L_{leak} \\ L_{open} &= L_{mag} + L_{leak} \end{aligned} \tag{3-1}$$

As the system approaches the ideal, the open-circuit calculation can ignore the leakage inductance entirely, assuming the open-circuit reactance to be simply the magnetizing inductance. However, as the system becomes less ideal, the magnetizing inductance in the short-circuit measurement becomes more and more significant. This makes determination of the leakage inductance difficult, and without an acceptable estimate of the leakage inductance, all that can be stated about the magnetizing inductance through the open-circuit impedance test is an upper bound.

This method is essentially the one suggested by the IEEE in standards document 390 for determining the reactance values in a non-ideal transformer. The IEEE suggests similar tests for the determination of the remaining parameters in the standard model. However, all the methods suggested suffer from the same problem as the one described above, which is that assumptions are made as to the relative importance of the various parameters, such that some are neglected in every measurement. This type of characterization may perform admirably on the final, optimized design. However, for the inexperienced transformer designer building prototypes by hand, such assumptions may be too optimistic. In the case of a separable core transformer, for example, the presence of the air gap in the magnetic circuit immediately brings the assumption of negligible leakage inductance into question. Another method of determining the parameter values must be found.

Unfortunately, analytical solutions for the various model parameters are extremely difficult to determine. For this reason, nonlinear regression is an acceptable alternative

for determining more accurate estimates of the model parameters. It is obviously not guaranteed to provide the correct answer, but in most cases the circuit designer has some a priori estimate of the parameter values and will know when the numerical method fails. The most comprehensive way to perform this task would be to use the three independent functions from the two-port impedance model, since this is the model which completely defines the transformer's behavior from a terminal perspective. However, driving point impedances proved easier to measure, and therefore, the equations used in this paper for the regression analysis were the open-circuit and short-circuit driving point impedances as a function of frequency. There are a number of other reasons as well for using regression to determine model parameters. Using this method, not only is it much easier to calculate parameters such as the parasitic capacitances, but the relative significance of choosing one model over another becomes clearer. For example, the parameters of the most interest in this study were the magnetizing and leakage inductances. However, there was a possibility that the winding resistances and parasitic capacitances would affect the test systems enough to return incorrect values for the inductances if the secondary parameters were omitted from the model. Regression results showed, however, that the inductance values changed very little regardless of the complexity of the model used. These results will be presented in more depth in Chapter 5.

3.3 Frequency Effects in the Core

The limitations imposed by the choice of core material can also prove to be significant in the design of any transformer. Depending on the application, the choice of core material may have no effect on the electrical characteristics of the system, or it may dominate the behavior. This section will examine in more depth the effect of frequency upon a transformer's behavior.

3.3.1 Magnetic Diffusion: Derivation of Skin Depth

If the resistivity of the core material is low, the effects of magnetic diffusion (usually presented in the context of skin depth in conductors) can be seen even at the relatively low transformer frequencies. [2] provides an equation to determine if magnetic diffusion effects will be noticeable in a transformer core, and this equation is analyzed in this section along with its effects on transformer performance.

Magnetic diffusion effects can be seen when an electromagnetic field propagates into a conductive medium and is attenuated by the induced eddy currents. The depth of penetration is controlled by the inverse of the imaginary component of the wave number. In a conductor, this quantity is called the skin depth, and is given by

$$\delta = \sqrt{\frac{2}{\omega\mu\sigma}} \tag{3-2}$$

where ω is the angular frequency of excitation, μ is the permeability of the material, and σ is the conductivity of the material. However, this is an approximation of the actual value and is only valid when the conductivity is large, which results in a loss tangent, given by $\frac{\sigma}{\omega\varepsilon}$, much greater than one. The actual wave number in its full, complex form, can be found from the dispersion relation

$$k^2 = \omega^2\mu\varepsilon(1 - \frac{j\sigma}{\omega\varepsilon}) \tag{3-3}$$

for a uniform wave propagating in a lossy medium. ε in this formula is the permittivity of the material. Formula (3-4), provided by Severns and his associates, calculates the field penetration depth by means of the standard skin depth formula and a correction factor. The correction factor approaches unity as the loss tangent increases and becomes significant as the loss tangent decreases.

$$\delta = \sqrt{\frac{2\rho}{\omega\mu}} \cdot \left[\sqrt{(\omega\varepsilon\rho)^2 + 1} - \omega\varepsilon\rho\right]^{-\frac{1}{2}} \qquad (3\text{-}4)$$

They then provide a chart of the adjusted skin depth for MnZn ferrite cores at 80 kHz as a function of resistivity. This chart is reproduced in Figure 3.2 and demonstrates that it is possible to encounter non-uniform flux distributions in the center leg and even in the side legs of large cores such as the one described in [2]. However, high resistivity in the core material is already a priority, since the same eddy currents which cause magnetic field attenuation towards the center of the core material also cause power dissipation. Thus, avoidance of non-uniform flux distribution simply adds one more motivation to choose a core material carefully.

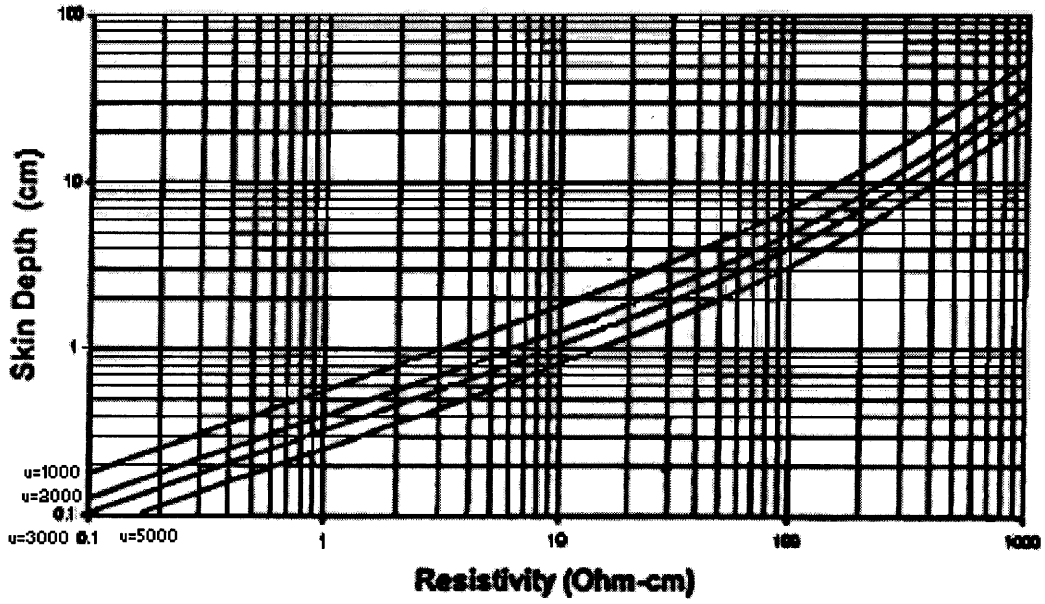

Figure 3.2: 80 kHz skin depth in MnZn ferrite[1]

[1]Figure 5 from [2]

In the system described in [2], the power dissipation problem is especially crucial since the core material in the center leg is difficult to cool. As examples, three commercial producers of magnetic cores offer the following materials:

Company	Material	Initial Permeability	ρ (Ωm)
Philips	3C85 (MnZn)	2000 μo	2
	3C90 (MnZn)	2000 μo	5
	3S4 (MnZn)	1700 μo	1000
TDK	PC44	2400 μo	6.5
	HS52	5500 μo	1
	H6B	2000 μo	45
Magnetics	F-Material	3000 μo	2
	R-Material	2300 μo	6
	K-Material	1500 μo	20

Table 3.1: Commercial Ferrite Core Data[2]

Figure 3.2 shows that to achieve a skin depth of 5 centimeters, which would place the center of the center leg at one half of a skin depth, a resistivity of 1.0 Ohm-meters is required. This value assumes a relative core permeability of around 2000, but Table 3.1 shows that such materials are not uncommon. Finally, [2] points out that nominal operating points are usually optimistic, since resistivity can drop with increased temperature, frequency, and flux density. A comprehensive examination of such dangers is difficult, since core manufacturers rarely provide extensive data on these dependencies. For temperature, the need to limit power dissipation for efficiency reasons as well as user safety reduces the danger that the material parameters will change much due to excessive heating. The authors of [2] cite 46 degrees Celsius as the maximum temperature of their center leg during full-power operation. Philips Soft Ferrites data book shows a drop of a

[2]from Magnetics, Philips, and TDK databooks

factor of two in resistivity between room temperature and 50 degrees Celsius. More generally, the temperature dependence of resistivity is given by [14] as

$$\rho = \rho_{\infty} e^{E_{\rho}/kT} \tag{3-5}$$

where ρ_{∞} is the resistivity extrapolated to $T \rightarrow \infty$, T is absolute temperature, k is Boltzman's constant, and E_{ρ} is the activation energy for the conduction process in electron volts. For frequency dependence, Phillips also reports resistivity dropping to a quarter of the nominal 100 kHz value by 1 MHz. The bottom line of the analysis is that designers must be careful when using a large core at high frequencies to limit as many of the dependencies as possible and choose a material whose nominal characteristics might seem like overkill. Operating at 50 degrees and 350 kHz might be enough to prevent usage of some of the more standard ferrites from Table 3.1, but a material such as TDK's H6B should have no trouble at these levels.

3.3.3 Magnetic Diffusion: Instantaneous Field Profile

In addition to the mathematical treatment of skin depth in ferrite cores, [2] presents two empirical graphs which illustrate how frequency affects magnetic flux penetration in a hypothetical core with a two inch diameter. Since the authors omit the material parameters of the core used to create their graphs, an analysis is provided here to allow designers to quantify this effect for their own systems. Appendix A of this paper describes the magnetic diffusion profile in the circular center leg of a magnetic core. The formulas are used here to recreate the flux density profiles of the two graphs from [2] in order to determine the values of the material constants in their core. Likely values of relative permittivity and permeability (10^5 and 2000) were chosen, allowing the published flux density profiles to be duplicated by varying the core resistivity. Figure 3.3 presents the recreated theoretical profile at 80 kHz.

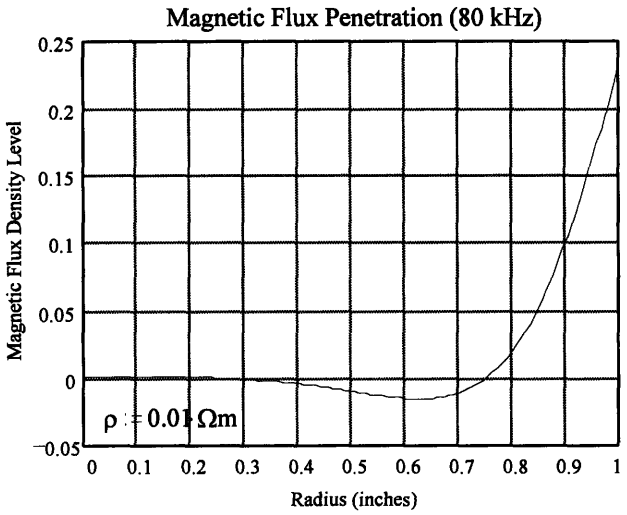

Figure 3.3: Magnetic Flux Density in 1" Radius Core at 80 kHz

Surprisingly, the profile above corresponds to a resistivity of 0.01 Ohm-meters, which, while available, is hardly typical. Figure 3.4 shows the profile for the same material parameters when excited at 1 kHz, . While not exactly corresponding to the 1 kHz graph in [2], Figure 3.4 is close enough to attribute the differences to the empirical nature of the published results.

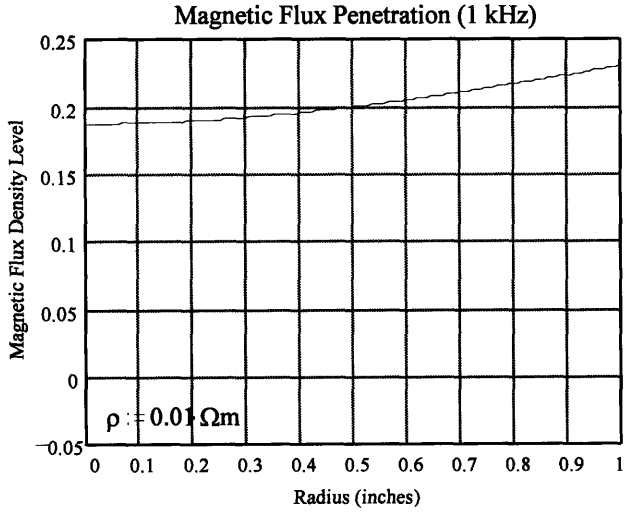

Figure 3.4: Magnetic Flux Density in 1" Radius Core at 1 kHz

For comparison, plots of magnetic diffusion at the same frequencies but more typical resistivities are presented in Figure 3.5. The upper set have a resistivity of 0.1 Ohm-meters, and the lower set correspond to 1.0 Ohm-meters. The only expected effect not captured by the plots is the possible decrease in resistivity as a function of frequency.

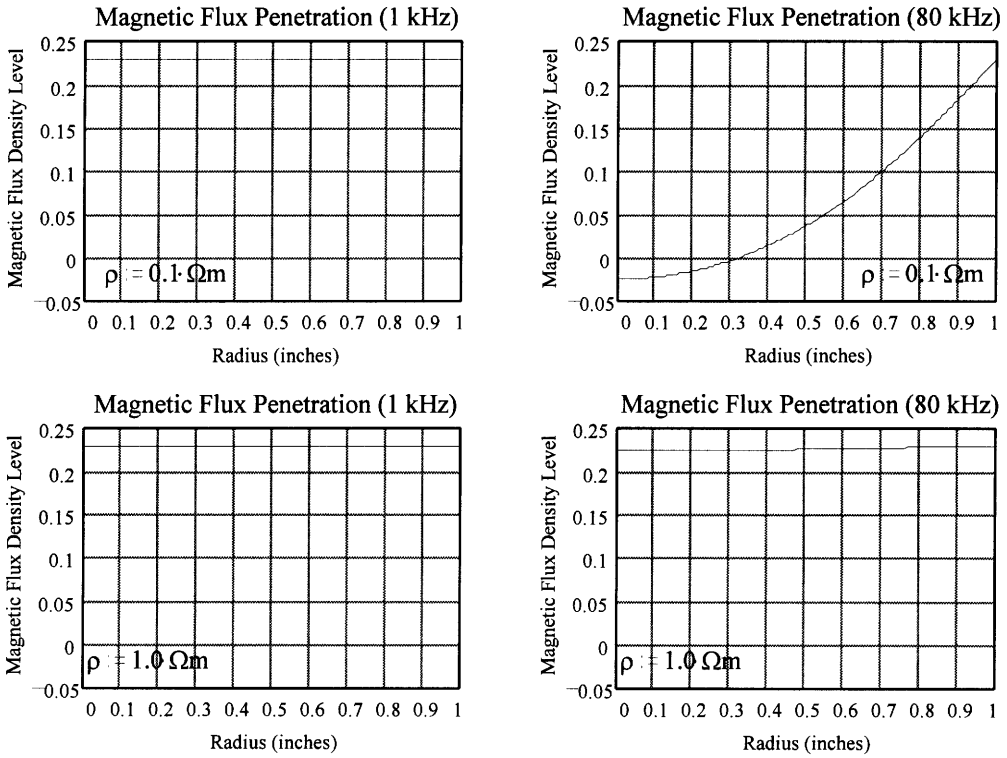

Figure 3.5: Theoretical Plots of Magnetic Diffusion for μ=2000

3.3.4 Magnetic Diffusion: Effect on Transformer Model

The attenuation of field strength toward the center of the core material can have a profound impact upon the magnetizing inductance of the system. [2] analyzes the case where the transformer is voltage driven and concludes that "the reduction of flux in one area requires an increase in another." The concern with higher flux is the creation of 'hot spots,' or localized areas of high power dissipation. However, a completely different problem arises if the system is current driven.

As was described in Section 2.2.5, an air gap's reluctance dominates the total equivalent reluctance of the core and thus determines the magnetizing inductance. For large cores, however, the flux in the core is restricted to flow near the surface. While this will not appreciably increase the overall reluctance of the core, it does prevent flux from entering the air gap from the center of the core, decreasing the effective cross-sectional area of the air gap. This increases the air gap's reluctance, causing a corresponding decrease in the transformer's magnetizing inductance.

Now it is clear how to analyze the flux in the system. With a voltage source, it *is* true that the flux linkage must be unaffected by any change in the magnetizing inductance, so the total flux in the core is also unchanged. (Upon closer examination, the reduction in the magnetizing inductance with no change in the leakage inductance will cause a small change in the voltage divider between the two, slightly lowering the voltage across the magnetizing inductance.) Note that because the overall impedance in the leakage and magnetizing inductances has dropped, *more* current actually flows through the circuit. It is this additional current which prevents the total flux in the core from dropping in spite of the increased reluctance. However, if the voltage source is replaced by a current source, the maximum possible current through the magnetizing inductance stays unchanged regardless of the skin effect. The reduction in magnetizing inductance lowers the voltage across the element, which thus reduces the flux in the core proportionally to the reduction in impedance.

When quantifying this effect, realize that as soon as the flux enters the air gap from the core, no eddy currents are present to attenuate it toward the center as they did in the ferrite. Thus, assuming that the attenuation profile holds for the air gap will yield a more conservative estimate of the magnetizing inductance than would actually be present, and the magnitude of the error depends on the size of the air gap.

Appendix A derives the conversion constant between the AC and DC magnetizing inductances, where

$$L_{AC\_mag} = K_{mag}(\delta, r_{core}) \cdot L_{DC\_mag}$$

This conversion constant, which is a function of the skin depth in the core and the core radius, is plotted in Figure 3.6 below.

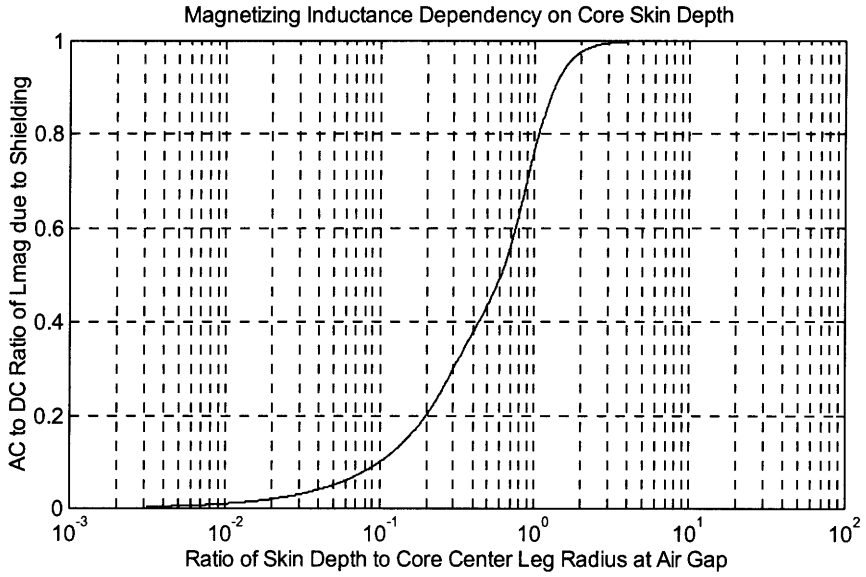

Figure 3.6: AC Magnetizing Inductance Dependence on Skin Depth

3.4 Frequency Effects on Windings

Analyses will be presented here to determine the effects of magnetic diffusion on horizontal foil windings as well. Foil windings are chosen for the analysis because they are most strongly affected by the high frequency changes in the field behavior.

3.4.1 DC Resistance of a Helical Winding

In order to determine the effect of high frequency excitation on resistance in a foil winding, a quantitative formulation of the resistance at DC must first be found.

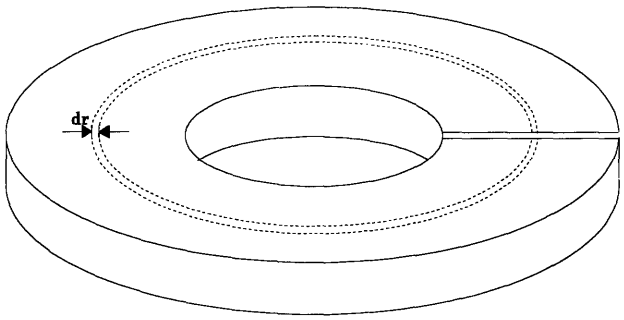

Figure 3.7: Idealized Turn of a Helical Winding

The derivation presented here is for the case of a helical winding with horizontally oriented foil windings. This geometry is common to one of the prototypes examined in Chapter 5 as well as the commercial system explored in Chapter 6. There are at least two simple methods of closely approximating the resistance of a helical winding, the first being a geometric approach. Consider one turn of a helical winding to be a centerless disk composed of an infinite number of differential shells, shown in Figure 3.7.

By symmetry, each carries an independent current proportional to the circumference of the ring, and the total current is set by the parallel combination of the differential resistances. The vertical displacement of the winding as a function of angle is ignored since its effect on the length of the differential ring is negligible. A geometric definition of resistance is given by

$$R = \frac{\rho l}{A} \tag{3-6}$$

where ρ is the material's resistivity, l is the length, and A is the cross-sectional area. However, this definition is not applicable in the case of the helical winding because the path lengths are different at the inner and outer radii. Looking at a thin ring, then, its differential resistance can be stated as:

$$dR = \frac{\rho 2\pi r}{t\, dr} \tag{3-7}$$

Since the difference between inner and outer radii is negligible for a differentially thin ring, $2\pi r$ is the path length, and dr multiplied by the thickness t is the area.

Combining these differential resistances in parallel yields:

$$R_{Total} = \left[\sum \frac{1}{dR}\right]^{-1} \tag{3-8}$$

and as dR $\rightarrow$0, in the limit this formula becomes

$$\frac{1}{R_{Total}} = \int_{r_i}^{r_o} \frac{t\,dr}{\rho 2\pi r} \tag{3-9}$$

to which the solution is $$R_{Total} = \frac{2\pi\rho}{t \ln(\frac{r_o}{r_{i1}})} \tag{3-10}$$

Alternatively, the resistance can be derived from an analysis of the fields within the structure. By symmetry, the potential around one turn of the helix cannot be a function of radius. Assume that around one turn the potential drop is V_0. Then, the electric potential in the winding is $$\Phi(\theta) = V_0 \frac{(2\pi - \theta)}{2\pi} \tag{3-11}$$

and since the electric field is the negative gradient of the electric potential, the electric field within the winding is $$\bar{E} = \frac{V_0}{2\pi r}\hat{\theta} \tag{3-12}$$

Since the system is electro-quasistatic, the following approximation holds between electric field and current density: $$\bar{J} = \frac{\bar{E}}{\rho} = \frac{V_0}{2\pi\rho r}\hat{\theta} \tag{3-13}$$

Finally, integrate over the cross-section of the winding to find the total current passing through and use Ohms Law with the total current and potential difference to find the resistance of the winding.

$$I_0 = \int_{r_i}^{r_o}\int_{0}^{t} \frac{V_0}{2\pi\rho r}\,dz\,dr = \frac{V_0 t}{2\pi\rho}\ln(\frac{r_o}{r_i}) \tag{3-14}$$

$$\therefore \quad R = \frac{2\pi\rho}{t\ln(\frac{r_o}{r_i})} \tag{3-15}$$

3.4.2: AC Resistance of a Helical Winding

This section provides a closed form solution for AC resistance to current in a winding which is recessed in a slotted magnetic material as shown in Figure 3.8. Proximity effects are then taken into account as well, but neither derivation necessarily holds for other systems because of the uniqueness of magnetic fields present in any given geometry. The derivation process follows the treatment in Appendix A of [15].

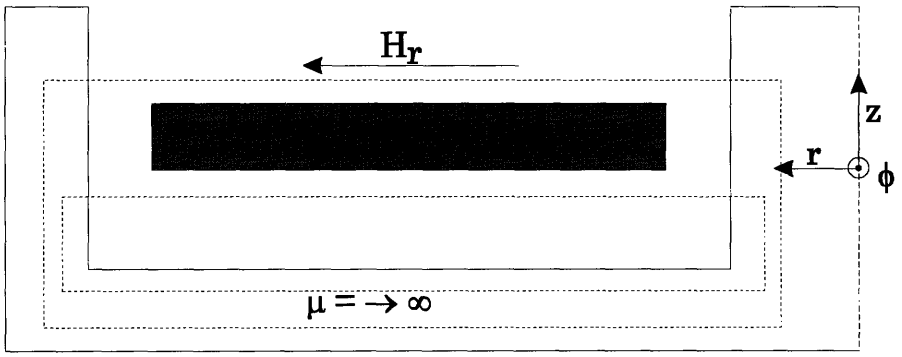

Figure 3.8: Recessed Winding for Calculation of AC Resistance

The AC resistance to current in the winding above depends on the distribution of the magnetic field within the winding, which must satisfy the magnetic diffusion equation,

$$\frac{1}{\mu\sigma}\nabla^2\overline{H} = \frac{\partial\overline{H}}{\partial t}. \tag{3-16}$$

For ϕ directed currents, there can be components of H in both the radial and z directions, making this a difficult problem to solve in general. However, within the slot in the magnetic material, the fields are assumed to be essentially horizontal. This simplifies the magnetic diffusion equation to scalar form:

$$\frac{1}{\mu\sigma}\nabla^2 H_r = \frac{\partial H_r}{\partial t} \tag{3-17}$$

which evaluates in cylindrical coordinates to

$$\frac{1}{\mu\sigma}\left[\frac{1}{r}\frac{\partial}{\partial r}\left(r\frac{\partial H_r}{\partial r}\right)+\frac{\partial^2 H_r}{\partial z^2}\right]=\frac{\partial H_r}{\partial t}. \tag{3-18}$$

The radial dependence of the magnetic field significantly complicates the situation. However, looking back at the current derivation in the helical geometry, it can be seen that the magnetic field will have an inverse r dependency. Therefore, any field solution of the form $\frac{H_0}{r}$ will make the first term in (3-18) proportional to $\frac{1}{r^3}$. Because of the inverse cubic nature of this term, it will be ignored in the analysis to follow, introducing a small but acceptable error into the final result. The equation then simplifies to one dimension:

$$\frac{1}{\mu\sigma}\frac{\partial^2 H_r(z)}{\partial z^2}=\frac{\partial H_r(z)}{\partial t}. \tag{3-19}$$

The one dimensional version of the magnetic diffusion equation has solutions of the form

$$H_r(z)=\mathrm{Re}\left\{\underline{H}_r(z)e^{j\omega t}\right\}. \tag{3-20}$$

Assuming $\underline{H}_r(z)$ to be of the form He^{-jkz} where k is the unspecified wave number, this solution can then be plugged into equation 3-19 to yield the dispersion relation

$$k^2 = j\omega\mu\sigma. \tag{3-21}$$

$$k=\frac{\pm(1+j)}{\delta} \tag{3-22}$$

satisfies the dispersion relation, where the skin depth δ is defined as $\delta \equiv \sqrt{\frac{2}{\omega\mu\sigma}}$.

Stating the full solution for the radial magnetic field to be the sum of the two possible components results in a magnetic field of

$$\underline{H}_r(z,r)=\underline{A}(r)e^{z(1+j)/\delta}+\underline{B}(r)e^{-z(1+j)/\delta} \tag{3-23}$$

Boundary conditions are needed to find the solution coefficients. Ampere's law can be used with the contours in Figure 3-8 to show that there is no magnetic field below the winding and a non-zero field above the winding, assuming there is a secondary above the conductor of interest. These two contours yield boundary conditions of

$$\underline{H}_r(0,r) = \underline{A} + \underline{B} = 0 \tag{3-24}$$

and

$$\underline{H}_r(t,r) = \underline{A}e^{t(1+j)/\delta} + \underline{B}e^{-t(1+j)/\delta} = \underline{H}_0(r) \tag{3-25}$$

where t is the thickness of the winding, and the origin is aligned with the lower winding surface.

This system can be solved in exponential form as [15] does for the special case where $t = \delta$. In general, the winding will not be exactly one skin depth, especially when the excitation frequency can change. A more general solution is given by

$$\underline{H}_r(z) = \frac{\sinh(z(1+j)/\delta)}{\sinh(t(1+j)/\delta)}\underline{H}_0(r). \tag{3-26}$$

Thus, the current flowing in the conductor is distributed according to

$$\underline{J}_\phi = \nabla \times H = \frac{\partial \underline{H}_r}{dz} = \frac{(1+j)}{\delta}\left[\frac{\cosh(z(1+j)/\delta)}{\sinh(t(1+j)/\delta)}\right]\underline{H}_0(r) \tag{3-27}$$

and power dissipation density is given by

$$P_{dd} = \frac{1}{2\sigma}\int_0^t \left(\underline{J}_\phi \cdot \underline{J}_\phi^*\right)dz, \tag{3-28}$$

leading to an actual power dissipation of

$$P_d = \int_0^{2\pi r_o}\int_{r_i} P_{dd}(r,\phi) r\, dr\, d\phi. \tag{3-29}$$

The product of J_ϕ and its complex conjugate is

$$\underline{J}_\phi \cdot \underline{J}_\phi^* = \frac{2}{\delta^2}\left[\frac{\cosh(2z/\delta)+\cosh(j2z/\delta)}{\cosh(2t/\delta)-\cosh(j2t/\delta)}\right]\left|H_0(r)\right|^2 \tag{3-30}$$

Plugging this expression into (3-28) results in

$$P_{dd} = \frac{1}{2\sigma\delta}\left[\frac{\sinh(2t/\delta) - j\sinh(j2t/\delta)}{\cosh(2t/\delta) - j\cosh(j2t/\delta)}\right]\left|H_0(r)\right|^2 \tag{3-31}$$

This can be simplified to remove imaginary terms, yielding

$$P_{dd} = \frac{1}{2\sigma\delta}\left[\frac{\sinh(2t/\delta) + \sin(2t/\delta)}{\cosh(2t/\delta) - \cos(2t/\delta)}\right]\left|H_0(r)\right|^2. \tag{3-32}$$

Note that when t = δ, the power dissipation matches the value reported in [15],

$$P_{dd} = \frac{1}{2\sigma\delta}\left|\underline{H}_0(r)\right|^2 \cdot 1.09. \tag{3-33}$$

In order to simplify the expression further, let

$$K_{skin} = \left[\frac{\sinh(2t/\delta) + \sin(2t/\delta)}{\cosh(2t/\delta) - \cos(2t/\delta)}\right]. \tag{3-34}$$

Thus, the power dissipation density equation becomes

$$P_{dd} = \frac{K_{skin}}{2\sigma\delta}\left|H_0(r)\right|^2. \tag{3-35}$$

Integrating in the radial and angular directions as indicated in (3-29) and replacing $H_0(r)$ with the value for the helical geometry magnetic field which is derived in Section 5.3.1.2 produces the total power dissipation,

$$P_{total} = \frac{\pi K_{skin} I_0^2}{\sigma\delta\ln(r_o/r_i)}, \tag{3-36}$$

which makes

$$R_{AC} = \frac{2\pi K_{skin}}{\sigma\delta\ln(r_o/r_i)} \tag{3-37}$$

since

$$P_{total} = \tfrac{1}{2}(I_0 \cdot I_0^*)R_{AC}, \tag{3-38}$$

Engineering Considerations

The magnetic field boundary conditions are identical for each winding layer located completely within the slot, so the total resistance of the coil can be found by multiplying the single layer resistance by the number of turns.

Comparing this resistance to the DC value derived in the previous section produces

$$\frac{R_{AC}}{R_{DC}} = K_{skin}\frac{t}{\delta}. \tag{3-39}$$

Note that for the case analyzed in [15], the AC resistance is again exactly K_{skin}, or 1.09, times larger than the DC resistance. For other thicknesses, the relationship becomes more complicated. The effect of winding thickness, normalized to the AC skin depth, on resistance can be seen in Figures 3.9 and 3.10. Both figures are normalized for the case where the thickness equals one skin depth.

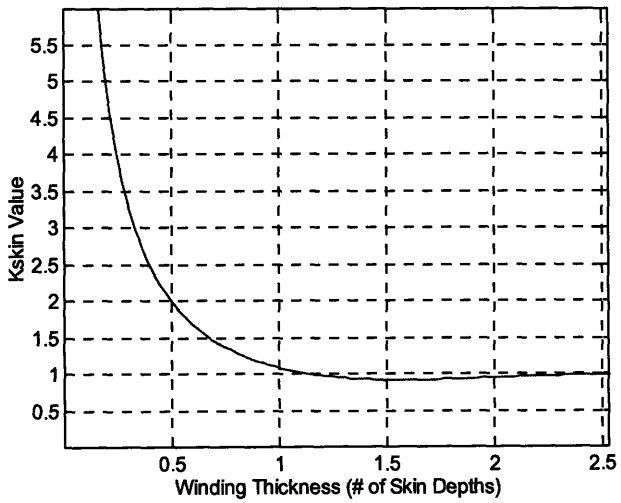

Figure 3.9: AC Self Resistance vs. Winding Thickness

Figure 3.10: DC Resistance vs. Winding Thickness

These graphs may be simply interpreted in terms of the two limiting cases. For extremely thick windings, the current can be modeled as a uniform density for one skin depth and nothing beyond - yielding the same value as a winding of one skin depth thickness at DC. On the other extreme, as the thickness of the AC winding is reduced, the magnetic field profile becomes increasingly linear between the two boundary conditions. This creates a current density which becomes more uniform as the thickness is decreased, which makes sense since the field is able to penetrate through a greater percentage of the winding. Thus, for thin windings, the AC and DC resistances become identical, and for thick windings, the ratio becomes t/δ, making the AC resistance many times the DC value.

It is important to realize that the accuracy of this derivation is reduced when the assumption of horizontal magnetic fields no longer holds. If the geometry of the core is changed so that the main fields in the gap are vertically oriented, as they are in the sandwich transformer of [15], the whole derivation is incorrect. In addition, the accuracy of the calculation decreases as the windings approach the edge of the core air gap where fringing fields begin to introduce vertical components to the magnetic field.

However, eddy currents within the current carrying conductor are not the only source of AC resistance. Load or magnetizing currents in one conductor can induce eddy currents in nearby conductors which feel the generated magnetic field. These currents dissipate power and thus increase the effective resistance of the system. Appendix A of [15] examines this proximity effect for the case of an open circuited secondary winding with thickness equal to one skin depth. Goldberg reports that eddy currents in the secondary increase the effective primary resistance by 32% of its DC value.

Again, it is possible to extend Goldberg's results to the general case of arbitrary thickness. As before, the origin will be located in line with the bottom of the winding rather than the top. Goldberg derives the boundary conditions as being equal on the top and bottom surfaces of the secondary conductor and proportional to the total number of ampere-turns in the primary. As before, the error due to the radial dependence will be ignored to allow use of the standard dispersion relation. This results in the magnetic field distribution within the secondary winding looking like

$$\underline{H}_r(z) = \frac{\sinh(z(1+j)/\delta) - \sinh((z-t)(1+j)/\delta)}{\sinh(t(1+j)/\delta)} \underline{H}_1(r) \qquad (3\text{-}40)$$

in sinusoidal form rather than the exponentials used in [15]. The current density becomes

$$\underline{J}_\phi(z) = \left(\frac{1+j}{\delta}\right) \frac{\cosh(z(1+j)/\delta) - \cosh((z-t)(1+j)/\delta)}{\sinh(t(1+j)/\delta)} \underline{H}_1(r). \qquad (3\text{-}41)$$

This expression is then substituted into (3-28) to yield

$$P_{dd} := \frac{\left(\left|H_1(r)\right|\right)^2}{2\cdot\sigma\cdot\delta} \cdot \left[\frac{2\cdot\sinh\left(\frac{2\cdot t}{\delta}\right) + 2\cdot\sin\left(\frac{2\cdot t}{\delta}\right) - 4\cdot\cos\left(\frac{t}{\delta}\right)\cdot\sinh\left(\frac{t}{\delta}\right) - 4\cdot\sin\left(\frac{t}{\delta}\right)\cdot\cosh\left(\frac{t}{\delta}\right)}{\cosh\left(\frac{2\cdot t}{\delta}\right) - \cos\left(\frac{2\cdot t}{\delta}\right)} \right] \qquad (3\text{-}42)$$

which can be likened to the previous formulation of the AC resistance by defining

$$K_{proximity} := \frac{2\cdot\sinh\left(\frac{2\cdot t}{\delta}\right) + 2\cdot\sin\left(\frac{2\cdot t}{\delta}\right) - 4\cdot\cos\left(\frac{t}{\delta}\right)\cdot\sinh\left(\frac{t}{\delta}\right) - 4\cdot\sin\left(\frac{t}{\delta}\right)\cdot\cosh\left(\frac{t}{\delta}\right)}{\cosh\left(\frac{2\cdot t}{\delta}\right) - \cos\left(\frac{2\cdot t}{\delta}\right)} \tag{3-43}$$

and restating the power dissipation density as

$$P_{dd} = \frac{|H_1(r)|^2}{2\sigma\delta} K_{proximity} \tag{3-44}$$

Since this has the same form as the previous case, $K_{proximity}$ will affect the AC resistance in exactly the same way as K_{skin}, although the corresponding magnetic fields will differ.[3]

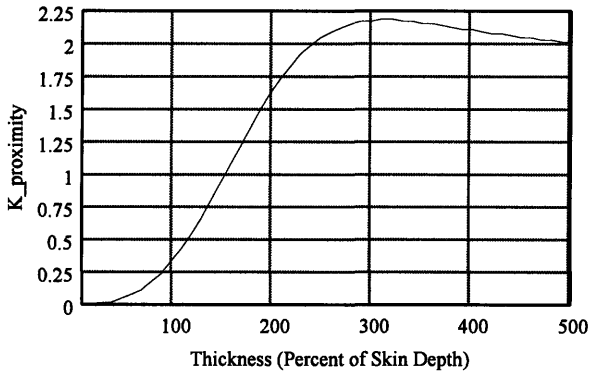

Figure 3.11: Winding Thickness Effect on AC Proximity Resistance

What is important to determine is whether the AC resistance effects significantly alter the value of the winding resistance in the IEEE transformer model. If it does, accurate prediction of the transformer performance becomes more difficult. The single-sided secondary helical prototype described in Chapter 5 will be used as a test case.

In the case where the secondary is left open-circuited, the resistive component of the driving point impedance is essentially just the winding resistance, modeled by a constant. While impedance analyzer measurements show that the resistive portion of the impedance becomes insignificant when compared to the reactive portion at high

[3] For a similar derivation of AC resistances, see [19]

frequencies, it still more than doubles by 100 kHz and increases by a factor of 172 above its DC value by 1 MHz. These increases at higher frequencies can be accounted for (while maintaining constant winding resistance in the model) with the core losses and parasitic capacitances which are included in the IEEE standard model. When nonlinear regression was performed on the measured driving point impedance values from the open-circuit Helical prototype to find values for the transformer model, the resulting winding resistance (25 mΩ) predicted 62 mΩ for the resistive portion of the impedance at 100 kHz as compared to the measured value of 58 mΩ. At one MHz, the predicted value was 3.94 Ω, compared to the measured 3.96 Ω. A key question is whether the unmodeled eddy current effects would reduce the discrepancy if added to the model or whether they would prove the regression procedure worthless because nonlinear effects dominate the system.

In order to answer this question, the total AC resistance for the primary winding is calculated taking the sum of the two components, self-induced and proximity skin effects. The self-induced portion of the total resistance was given by (3-39). Starting from the conductor closest to core, however, each turn feels the field from all outer conductors as well as the field due to its own source current and this results in proximity effects proportional to the experienced field. Each field can be referred to a single turn field by squaring its relative strength. Thus, the proximity effects felt by the primary conductors can be expressed as an extension of (3-39) as well and results in

$$R_{AC2} = \frac{R_{DC}}{4}\left[K_{proximity}\frac{t}{\delta}(1+2^2+3^2)\right] = \frac{R_{DC}}{4}\left[14K_{proximity}\frac{t}{\delta}\right]. \qquad (3\text{-}45)$$

Finally, it is possible for all four turns of the open-circuited secondary to feel the full field from all four primary turns. If the secondary is positioned correctly on the other side of the air gap (as it would be in a commercial model), the fields felt by the secondary should

be negligible leakage fields only. However, for the prototypes, the exact placement of the primary on one side of the gap and the secondary on the other was not guaranteed. If all four secondary windings are located on the same side of the gap as the primary, Ampere's law can be used as in the derivation of (3-40) to find that a similar horizontal magnetic field generated by the four primary windings surrounds each of the secondary turns. This yields a third AC resistance component which is given by

$$R_{AC3} = \frac{R_{DC}}{4}\left[4K_{proximity}\frac{t}{\delta}(4^2)\right] = \frac{R_{DC}}{4}\left[64K_{proximity}\frac{t}{\delta}\right]. \qquad (3\text{-}46)$$

At this point, all derived sources of AC resistance have been accounted for. Summing the three components, the final relation becomes

$$R_{AC} = \frac{R_{DC}}{4}\left[\frac{t}{\delta}\left(4K_{skin} + 78K_{proximity}\right)\right]. \qquad (3\text{-}47)$$

Plugging in values for the prototype windings at 100 kHz yields parameter values of

t = 0.051 mm
δ = 0.206 mm
K_{skin} = 4.054
$K_{proximity}$ = 0.005.

The resulting AC resistance is only 2.78% higher than the DC resistance of 23.6 mΩ, basically because the conductor thickness is only one quarter of the skin depth at 100 kHz. As presented in the section describing the self-induced skin effect dissipation, at this thickness the fields are able to fully penetrate the conductor, so very little extra dissipation results. For the proximity effect components, eddy currents which are induced on the top and bottom surfaces are so close together that they practically cancel, leading to the low proximity constant. Note that when the windings are a full skin depth thick, which happens in this system at around 1.6 MHz, the AC resistance is over 7 times the DC value.

Although Goldberg explores the AC resistive component added by external vertical magnetic fields, that source is insignificant in this case because the core geometry prevents the vertical fields from having much amplitude. Even around the air gap between the two core halves, the vertical fields seen by the windings are only fringing fields and are much lower than the full-strength fields used by Goldberg in his derivations.

Thus, for the frequency region around 100 kHz, the linear model of winding resistance has been shown to be quite accurate. Conversely, for winding thicknesses approaching a full skin depth, such as at frequencies near a megahertz, the linear model is poor. This conclusion is reflected in Figure 3.12, which shows the ratio between the AC winding resistance and DC winding resistance at frequencies up to 2 MHz.

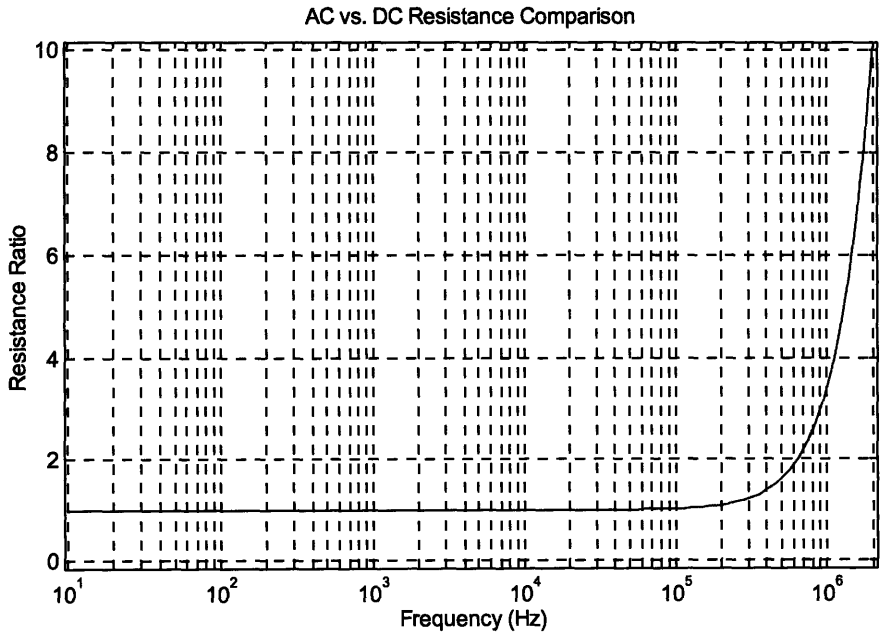

Figure 3.12: AC to DC Resistance Ratio

3.5 Power Transfer Considerations

In the end, the evaluation of the design process comes down to answering one question. Will this design efficiently transfer enough power to meet the needs of the load? Two measurements of the effectiveness of power transfer are the power factor and efficiency. As in other fields, efficiency is simply the proportion of the power supplied which is received by the load. This value increases with lower winding resistances and higher core resistance. More than simply being a benchmark for how much energy is being wasted, the efficiency is important because the transformer heats up due to the dissipation, creating the need for expensive cooling systems to avoid safety hazards during use. The power factor is more complicated, being defined as the ratio between real and apparent power. For low power factors, much of the energy in the system is reactive and sloshes between internal energy storage elements rather than being transferred to the load. This has two effects, the first being that for a given maximum power level being drawn from the source, it takes longer to transfer energy to the load, the second effect being that the efficiency decreases as well. The efficiency decrease is due to the fact that current corresponding to reactive power still flows through the windings and dissipates real power, even though the power carried by the reactive current never makes it to the load. The purpose of transformer design, therefore, is to develop systems which approach the ideal as closely as possible. This is done through minimizing core losses, winding losses, parasitic capacitances, and leakage inductances while maximizing the magnetizing inductance, which is why this paper attempts to quantify these parameters. Once a design is completed, however, the question returns - how good a design is it?

Unfortunately, without further information, such an evaluation is impossible. As shown in Appendices D and E, the driving point impedance of the transformer depends

on the load and is a function of frequency. Worse yet, high frequency transformers are rarely attached directly to their loads, usually having a rectifier or other power electronics devices in between. Reactive elements in the power electronics surrounding the circuit can resonate with elements in the transformer coupling and modify the harmonics which would have otherwise flowed in the system. Each harmonic exists at a different frequency and has a corresponding amplitude, so the true system efficiency and power factor is a superposition of the various components present (assuming a linear model). Empirically, it is reasonable to apply power with the load present and monitor the currents which flow as a result. Either directly from the resulting waveforms or using Fourier analysis, it is possible to then determine the power transfer characteristics of the system, but without this knowledge it is fruitless to make claims about the system performance. Without such analysis, the best designs will be those which maintain high efficiency and power factor over a wide range of frequencies starting from the switching frequency near the lower end.

Since the fundamental and harmonics which combine to determine the final system performance can be thought of as independent excitations in a linear system, it is instructive to look at the power factor and efficiency as a function of frequency. It was stated that those designs which maintain high efficiency and power factor over a wide range should have better overall performance than the designs which have only a narrow bandwidth of good behavior. Figure 3.13 presents a sample system with the measurements of interest over two decades of frequency. It was chosen to clearly show the major features which affect system performance, not because it is a typical design. The electrical circuit which created the plots is shown in Figure 3.14, a simplified version of a standard, unity turns-ratio transformer model, where both leakage inductances and winding resistances are matched, and the capacitances and core losses have been omitted.

The upper plot presents real power in and real power out as a function of frequency while the lower plot presents the efficiency and power factor of the circuit. A resistive load is used.

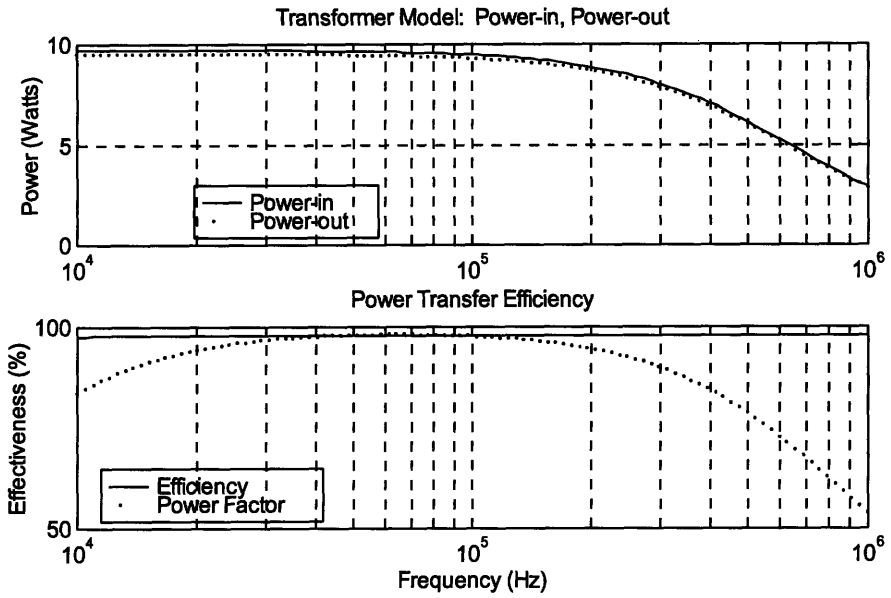

Figure 3.13: Example Power Transfer Plot

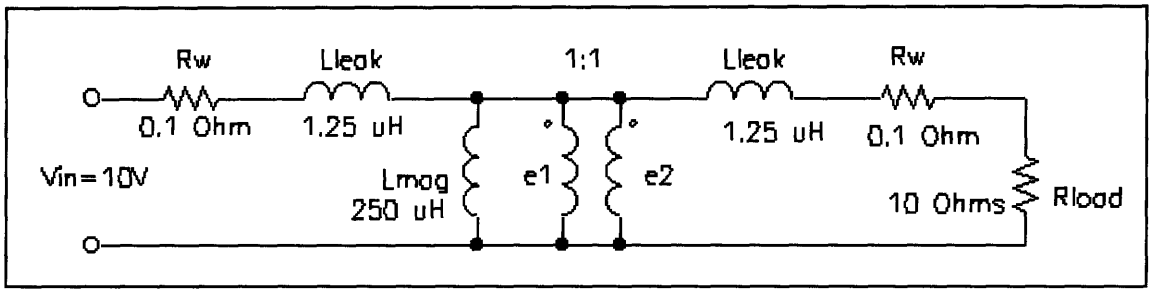

Figure 3.14: Electrical Circuit for Power Transfer Analysis

At low frequencies, the impedance of the magnetizing inductance is small compared to the load impedance, so much of the power is recycled through the magnetizing inductance, lowering the power factor. As the frequency increases, the magnetizing impedance grows to the point where little magnetizing current flows, forcing

most through the load. However, the leakage inductance prevents this from being a straightforward process. The leakage inductance increases proportionally to frequency as well, reducing the fraction of the secondary voltage seen across the load. The larger the ratio between the magnetizing and leakage inductances, the higher the frequency may be pushed before the leakage inductance becomes significant. For a given winding geometry, the ratio between the magnetizing and leakage inductances is fairly constant, so this value is a good measure of the system performance. For high ratios, the power factor can be high even for multiple harmonics above the switching frequency, thereby optimizing overall performance. For low ratios of the inductances, the power factor may be good at the switching frequency, but poor at higher harmonics, reducing the total real power transferred for a given level of apparent power.

It is of interest that the ratio between magnetizing and leakage inductances still generally holds as the number of turns on the transformer is modified. Both increase with the square of the number of turns. This provides a qualitative answer to the question of whether it is better to have more or fewer turns - the result being that neither extreme is advantageous in a nonresonant topology. Just it did when the frequency was varied, minimization of the leakage inductance through reduction in the number of turns can eventually lead to the load impedance dominating the magnetizing impedance, preventing power transfer. Similarly, striving for a huge magnetizing inductance forces all the current across the load, but the leakage impedances dominate over the load, preventing much voltage from appearing across the load. Again, the optimal value is in between and depends on the ratio between magnetizing and leakage inductances, and between either the magnetizing or leakage inductance and the load. For this simple topology, these two ratios define the peak power factor achievable regardless of the absolute values involved.

The caveat to the preceding discussion, of course, is the resonant design. If the load is known and fairly constant, it is possible to use resonant capacitors to remove the effects of the reactive power from the system. In this situation, it is much better to maximize the magnetizing inductance and set the power transfer level by varying how far off resonance the system is driven.

Chapter 4

Measurement Hazards

For many of the analytical calculations made in this paper, laboratory measurements were taken in order to verify or refute the myriad assumptions which were usually necessary to arrive at useful formulas. Occasionally, the laboratory measurements exposed faulty logic and prompted a new derivation. Quite often, however, measurement artifacts were present which prevented the results from being useful. In the most straightforward of these cases, the measurement actually included multiple known phenomena which could be separated and the desired result extracted. Sometimes, however, the artifacts were unquantifiable and unavoidable, forcing the process in question to be abandoned. Unfortunately, in some cases, the presence of the artifacts was not recognized immediately, which led to faulty conclusions about the physical system. Some of these artifacts are described here in the hopes that future designers might avoid their pitfalls.

4.1 Lead Inductances

The determination of the leakage inductances for the prototype transformers in this study was a case where the order of magnitude of the results was the same with and without the measurement artifacts so the inaccuracy was not caught immediately. The measurement in question was an impedance measurement of the primary winding with the secondary short circuited, and the problem was due to excessively long lead wires. Because a loop of wire with current running through it is effectively a one-turn, air-filled inductor, this effect was added to the desired leakage inductance of the system, giving erroneously high results. The eventual solution was to strip a section of each lead flush

against the transformer coil and perform a four-wire measurement. Thus, the current was supplied through the regular leads, but the impedance measurement was taken without the leads having any effect. With a two wire measurement, even leads of about one and a half inches added enough additional leakage inductance to mask the true value.

The extent of this effect was discovered because of the fact that both the leakage and magnetizing inductances should be proportional to the number of turns squared. While the magnetizing inductances seemed to do so, the leakage inductances did not show the same dependency at first, and it wasn't until the four-wire measurement was taken that the inconsistencies disappeared.

4.2 Fringing Fields

The next artifact was encountered while trying to validate simulated field values using a gaussmeter on the actual system which was the model for the computer simulation. The results of finite element analysis can be highly dependent on the mesh used to divide the simulation volume, and since the user can control the mesh refinement, there is a distinct possibility that improper refinement can produce inaccurate simulation results. For this reason, confirmation of simulation methods on a test case which can actually be measured in the lab is a good idea before proceeding to a system whose results cannot be verified. In this case, the problem which caused the discrepancy between the computer simulation proved to be fringing fields and a small inaccuracy in the computer model.

The system was a prototype transformer with horizontal, helical windings. The actual transformer was wound around a central spool which could be separated from the EE core. This was so that the same EE core could be used to test multiple winding systems with little reconstruction effort. However, the diameter of the spool was

significantly larger than the diameter of the central core leg, as shown in Figure 4.1, and this difference was forgotten when the model was transferred to the computer.

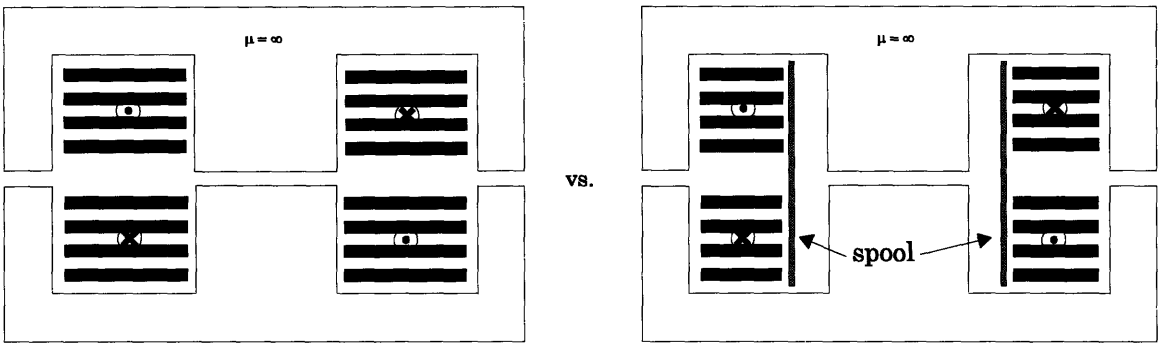

Figure 4.1: Discrepancy between Transformer Models

The difference was purely one of fringing fields, as the computer model incorrectly forced interwinding fields to remain between the windings right up to the core material while the actual system allowed the fields to spread out before entering the core. The measurement in question was the magnetizing inductance of the transformer, which appeared to be correct. As it turns out, the artifact had no effect on this value. (It did have an effect on the leakage inductance, since the width of the windings was incorrect. This dependency was presented in Chapter 2.) However, rather than simply accept the simulated inductance value as being within the experimental error of the measured value, a logical test is to compare the magnetic fields in the simulated and actual systems. For this reason, the fields in the center and side legs' gaps were measured in both systems.

The results led to a series of bizarre conclusions about the effects of fringing fields. A quick estimate of the fields can be performed, which ignores fringing fields, simply using conservation of flux, and this value was used as the comparison for both systems. This was a mistake, for as will be shown, the fringing fields in this case have a significant effect on these fields. When fringing is ignored, the three dimensional

problem is reduced to two dimensions. Assuming that the core has no reluctance and that the air gaps in the core material have equal lengths, a contour can be drawn through the center leg and one of the side legs which, using Ampere's Law while driving only the primary, fixes the sum of the magnetic fields in the two gaps.

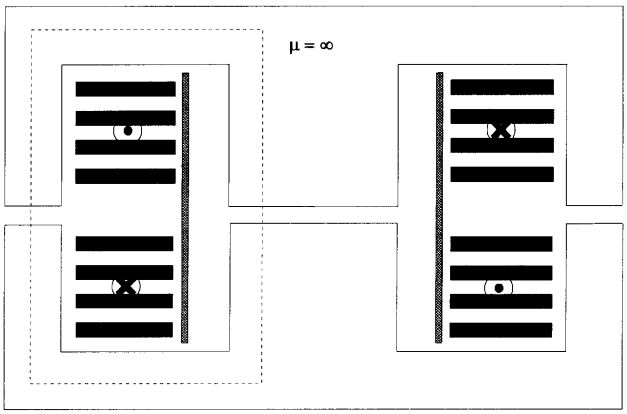

Figure 4.2: 2-D Field Approximation Method

Referring to the field in the center as H_c and the field in the side leg as H_{leg}, where both fields are considered positive in the direction of the contour, this is expressed by

$$H_c + H_{leg} = \frac{I}{l_{gap}}. \tag{4-1}$$

Then, using conservation of flux, the ratio of the two field values can be found. Assuming a symmetrical core, conservation of flux dictates that the magnetic flux density in each gap is inversely proportional to the ratio of the cross-sectional areas of the gaps, stated by

$$\Phi_c = \Phi_{leg} \quad \Rightarrow \quad \frac{H_c}{H_{leg}} = \frac{A_{leg}}{A_c}. \tag{4-2}$$

What this predicted for the laboratory system was approximately equal fields in both air gaps, since each side leg of the core is designed to have approximately half the area of the center leg.

What the computer showed was almost 60% higher field levels in the center leg, and to complicate matters, when an identical setup was measured experimentally, the empirical ratio seemed to increase with flux level. The eventual conclusion was that both calculations were in error. The laboratory measurements were inaccurate because they were being taken at DC, as in the computer model, but unlike the computer model, the actual core experiences magnetism retention which interferes with the measurements. Switching to alternating current excitation, the field ratio stabilized at a constant 40% difference, independent of flux level.

The error in the computer model proved to be the final discrepancy. The extra space between the windings and the center core leg in the laboratory system increased the fringing fluxes around the core, increasing the effective area of the center gap slightly and reducing the ratio from 60% to 40%. As predicted by the computer, the center field was larger than the side leg fields in the first place because of fringing around the side legs and some fringing in front and behind the core. Another way to illustrate this effect is to use the analogy of water for the magnetic flux. All the flux must flow through the center leg, so a measurement of the flux in the center leg air gap is fairly accurate. However, once the flux is through the air gap, there are many ways to return to the other side again, only one of which is through the side legs. Because of the inevitable fringing, a significant amount of flux is not captured in the side leg air gaps and is therefore not measured.

4.3 Ghost Gaps

Before measurements were being taken with a gap in the cores, the results were susceptible to another error. It was observed that the results were not always repeatable when measuring the magnetizing inductance of a core under different winding conditions. In fact, the magnetizing inductance was occasionally inexplicably low, but when the setup was reassembled and measured again, the inductance had been restored to its full value. The cause turned out to be nothing more than grease from the lab environment collecting on the surfaces of the cores, which, when placed together, created an effective air gap of a few mils. Besides just being a reason to maintain a clean lab environment, this underscores the use of air gaps in transformer cores for stability. Not only does the introduction of an air gap prevent tiny fluctuations in the surface contact of the two core halves from affecting its magnetizing inductance, but it actually reduces the effects of any natural fluctuations of the core's intrinsic permeability. The use of series air gaps to stabilize magnetizing inductance is described in more detail in [11, p.136] and [10, p.228].

4.4 AC Inductance Simulation Artifact

Some of the most interesting effects observed in this study were variations in the equivalent circuit parameters at high frequencies. Eddy current simulations were used to verify these frequency dependencies, but incorrect interpretations of initial simulation results caused as much confusion as enlightenment. Inductances are calculated from the simulation results through energy methods as described in Section 2.3.2. The formula is

$$\int_V \tfrac{1}{2}\mu_0 H^2 dv \;=\; \tfrac{1}{2} L i^2 \qquad (2\text{-}19)$$

and can be used to determine either the leakage inductance, as in Chapter 2, or the magnetizing inductance if the leakage value is already known.

The computer simulation returns the total stored magnetic energy, calculated from the left side of (2-19). The eddy current simulations showed that the magnetic energies corresponding to both the leakage and magnetizing inductances were significantly reduced at high frequencies. This made sense since magnetic shielding would increase the effective air gap reluctance for the magnetizing case and increase the average flux path around the individual windings for the leakage case. However, while the energy values being returned by the eddy current simulations were around half the DC values, the peak fields were the same strength as in the DC simulations. A closer inspection of the leakage derivation shows that the energy difference is due to the need to take the time average of the field values in the AC case. Since the stored energy is proportional to the square of the field values, the time average of a sinusoid squared is one half the square of the peak value. However, the same relationship is true of the average current in the system, so while the lowered stored energy values appeared to suggest that the inductances had decreased, in reality, all that had changed was the formula needed to calculate the inductance from the energy value. Thus, for the DC system, $L = \frac{2U_m}{I^2}$, but for the AC system, $L = \frac{2\langle U_m \rangle}{\langle I^2 \rangle} = \frac{4\langle U_m \rangle}{I_{peak}^{\ 2}}$.

Chapter 5

Winding Geometry Comparison

How to wind the conductors around the core is a more complicated problem than it might initially seem. Most texts on transformer design focus on the packing factors of various gage copper wire and their resistance per kilometer in order to fit the number of required windings within a maximum low frequency resistance. This approach is not suitable for small, electronic transformers whose winding resistance is intrinsically low and where packing factor is not significant for determining the number of turns used.

The most important variable ignored by the traditional design procedure is the leakage inductance - probably because the ratio between leakage and magnetizing inductances is small enough to be ignored. However, for a separable core transformer where the magnetizing inductance may be limited by the necessary insulation between primary and secondary windings, the leakage inductance may be very important. If winding volume is not a critical constraint, foil windings solve the problem by forcing the magnetic field at high frequencies to flow parallel to the conductors. This increases the minimum path length the flux follows, reducing the magnitude of the leakage fields.

5.1 Foil Windings: Geometry Matters

The decision to use foil windings, however, introduces new decisions relating to the positions and orientations of the foil conductors. Three main geometry variables immediately suggest themselves, with many variations possible as well. First, the conductors can be oriented either horizontally or vertically. Second, the conductors can be wrapped around the core either concentrically or adjacent to each other. Finally, the primary and secondary windings can be located either concentrically or adjacent to each other around the core. A comprehensive naming convention could list the three variables

that define the geometry, such as [External style-Internal style-Orientation]. Although this yields eight different geometry types (assuming both windings have the same orientation) it will be shown that all eight can be classified as one of two simple types. The position of the air gaps in the core will be shown to have negligible effects upon the leakage inductance. This allows the air gaps to be ignored during leakage calculations, which reduces the number of unique derivations to three, two of one type and one of the other. Even with identical derivations, however, differences in dimensions between the geometries cause the leakage fields and leakage inductance to be different for each.

The two basic types can be described as distributed field and concentrated field transformers, the difference being that the concentrated types have only one non-zero field located between the primary and secondary windings and essentially no fields in the interwinding spaces located within each winding pack. In contrast, the distributed types have a maximum field between the two winding packs and lower fields to either side. Cross-sections of the eight types are presented in Figure 5.1, which also shows each leakage field profile with a solid line in the core next to the windings. In dashed lines are possible locations where the core may be cut to allow separation of the primary from the secondary. As a general rule, all geometries with concentric primary and secondary packs must be cut such that part of the shell is removed, and geometries with adjacent packs can also be cut so as to remove only a portion of the center leg if an EE-type core is used. The first four geometries in Figure 5.1 will be analyzed mathematically. These were chosen on the basis of fabrication ease, but also present one example of each unique leakage derivation and an example of how dimensions can be just as important as geometry in determining the leakage inductance. Also, these four types have been given nicknames for easy identification, listed in quotation marks beneath each geometry.

Figure 5.1: Transformer Winding Geometries in Cross-Section

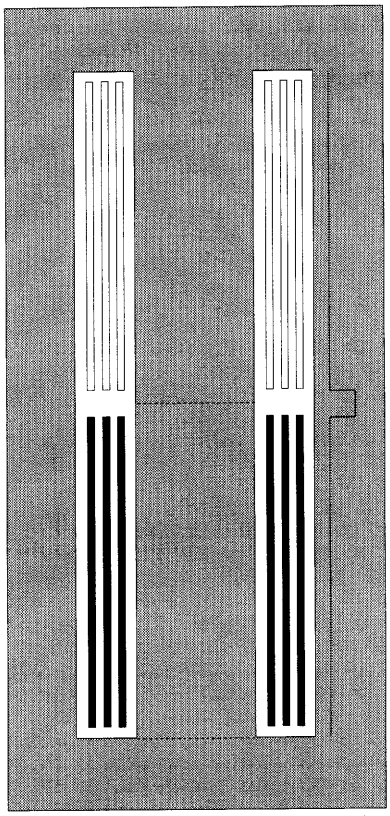

(a) Adjacent-Concentric-Vertical ("Adjacent")

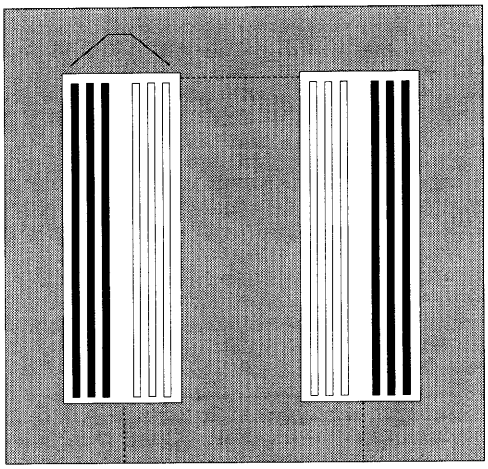

(b) Concentric-Concentric-Vertical ("Concentric")

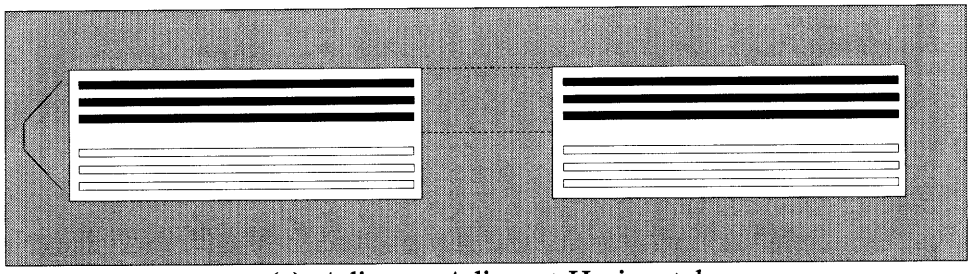

(c) Adjacent-Adjacent-Horizontal ("Helical")

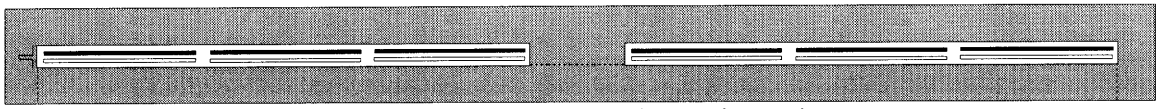

(d) Adjacent-Concentric-Horizontal ("LPKF")

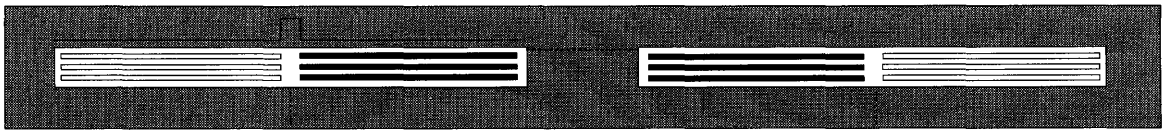

(e) Concentric-Adjacent-Horizontal

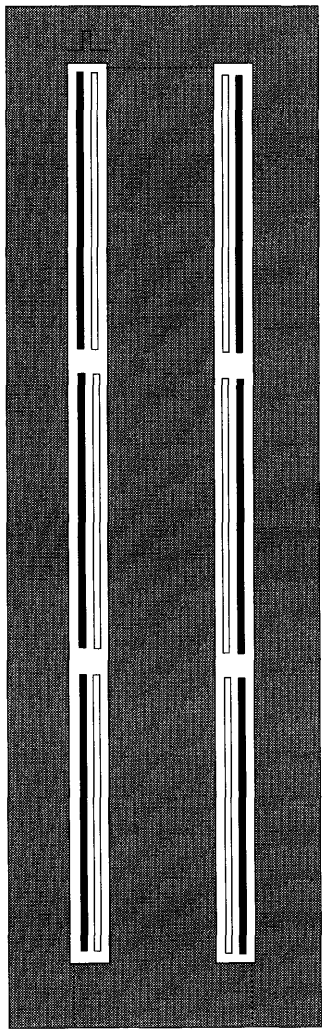

(f) Concentric-Adjacent-Vertical

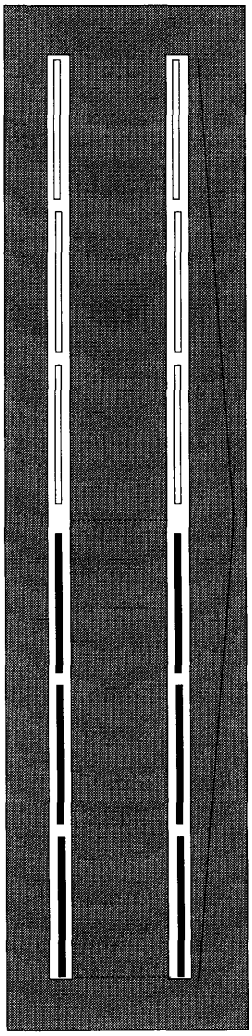

(g) Adjacent-Adjacent-Vertical

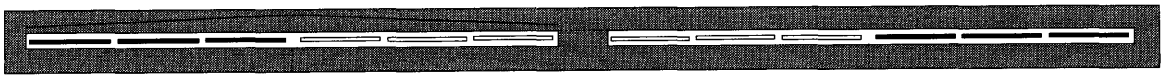

(h) Concentric-Concentric-Horizontal

5.2 Prototype Measurements and Computer Analysis

The mathematical derivations of leakage in this chapter are evaluated using a set of hypothetical dimensions comparable to those found in the MagneCharge charging system. In order to verify the accuracy of the calculations, however, prototype transformers were built in the lab corresponding to each of the winding geometries. Because all were built to fit on the same core, the winding dimensions differ, leading to leakage differences due to the dimensions as well as winding geometry. Equivalent circuit transformer models for each of the prototype systems are developed through a number of measurements, including open and short-circuited secondary driving point impedance values from 5 Hz. to 1.6 MHz. The results from these tests are used to derive values for the elements in the IEEE standard equivalent circuit and show which elements in the model are significant. The raw data from the driving point impedance tests are located in Appendix D.

Magnetizing and leakage measurements are commonly extracted from open-circuit and short-circuit impedance tests, where the short-circuit value yields the total equivalent leakage, and the open-circuit value is approximately the magnetizing plus the primary leakage, as described in Chapter 2. The HP 4192A can increase the accuracy of this calculation somewhat by returning just the reactive portion of the impedance, treating the circuit as a simple series LR circuit. Since this approximation holds for a good transformer, these results will be acceptable in most cases. However, there was no guarantee that the prototypes built were, in fact, "good" transformers, so this level of complexity was insufficient. The goal of the measurements was to derive an equivalent circuit model for each transformer that would include the resistances and capacitances as well, however, so nonlinear regression was used to obtain all the equivalent circuit values at the same time. The results of the regression provide the best approximation for the

system that an equivalent circuit with constant component values can provide. What the circuit does not represent, however, is the frequency dependence of many of the element values, such as variations in the magnetizing inductance and series resistances due to skin effects. As was shown in Chapter 3, these values can be calculated as functions rather than constants, but standard circuit techniques will not be able to take these variations into account. These deficiencies in the model should be considered when evaluating the results of the prototype analyses. The regression was performed using MATLAB, and the relevant code is provided in Appendix E.

The core used for the prototypes was an EC90 TDK core with an initial permeability of 2500 and nominal resistivity of 10 Ohm-meters[1]. Figure 5.2 shows the relevant core dimensions. The prototypes were wound on a plastic bobbin with a 1.75 inch diameter and the core gap used was 1 mm.

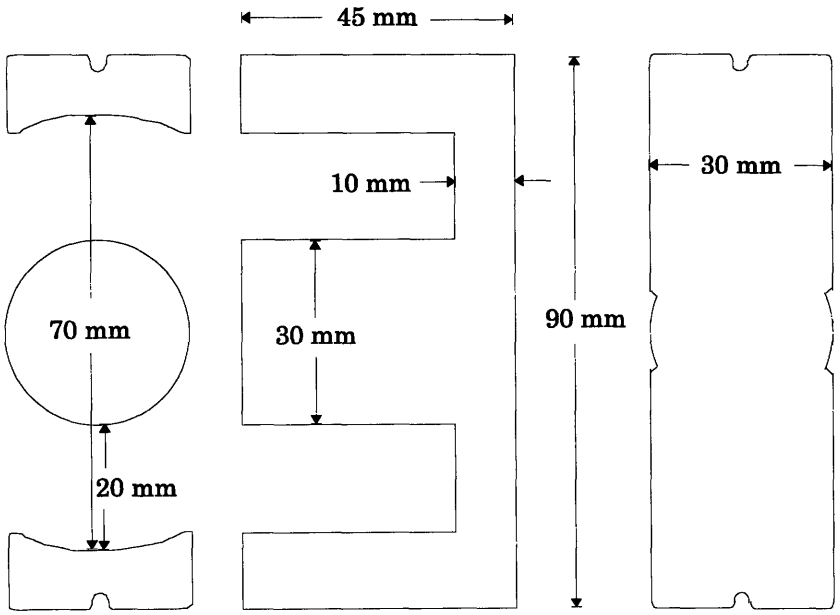

Figure 5.2: EC90 Core Dimensions

[1]made of discontinued PC-30 ferrite (MnZn).

For the computer analysis, two simulations, corresponding to the open and short circuit secondary tests, were done for each model in Ansoft's 3-D finite element simulation package, Maxwell. Given the total amount of stored energy in the system, which is a parameter returned by the simulation, approximate values for the two inductances can be determined as previously described. In addition, Maxwell will calculate the inductance matrix for any set of conductors, as described in Chapter 2. In order to use this feature of the software, all conductors of the two winding packs must be combined into one volume, since the computer does not know that four conductors stacked on top of one another are actually all part of the same winding, connected in series. The resulting flux distribution will be almost identical to the actual system as long as the same number of ampere-turns are maintained. Therefore, four amperes would be applied to a single conducting block representing four turns of a single winding.

5.3 Helical Winding

The Helical winding geometry is an example of a distributed leakage field transformer. As will be discussed in Chapter 6, this is the type that is being used by General Motors in the MagneCharge battery charging system. The windings themselves can be made using a number of fabrication processes, one of which being printed circuit board technology. At high frequencies, the skin effect in the windings force the magnetic fields in the interwinding spaces to flow parallel to the wide dimension of the conductors. This effect, and its corresponding manifestations in each of the other types, will be the basis of the mathematical derivation of the leakage fields.

5.3.1 Leakage Derivations:

The following three derivations demonstrate a number of ways the same geometry can be analyzed. In fact, the first leakage calculation shows a commercially implemented version of the Helical design which differs from Figure 5.1c by separating the secondary

windings into two groups. The second derivation uses a more complex field analysis on the same system and compares the results. Finally, the third calculation evaluates the setup shown in Figure 5.1c and demonstrates the improvement due to the split secondary.

5.3.1.1 Split Secondary, Rectangular Field Geometry

The choice of an EE core geometry with a circular center leg for these derivations originates from the Society of Automotive Engineers Electric Vehicle Inductive Coupling Recommended Practice Document (SAE J-1773) draft from February 1995. The portion of the center leg surrounded by the primary windings (called the puck because of its shape) is removable, introducing an air gap on either side of the puck. The windings for this calculation are helical, with the primary windings located in the shaded, removable section of Figure 5.3 and the secondary windings split into two symmetric groups above and below the primary. The secondary windings are electrically in series. Figure 5.3 represents a cut-away view along the long axis of the core. Note that the relative width of the center leg to either outer leg in the figure is more than two to one due to the circular geometry for the center leg and the rectangular geometry for the outer legs.

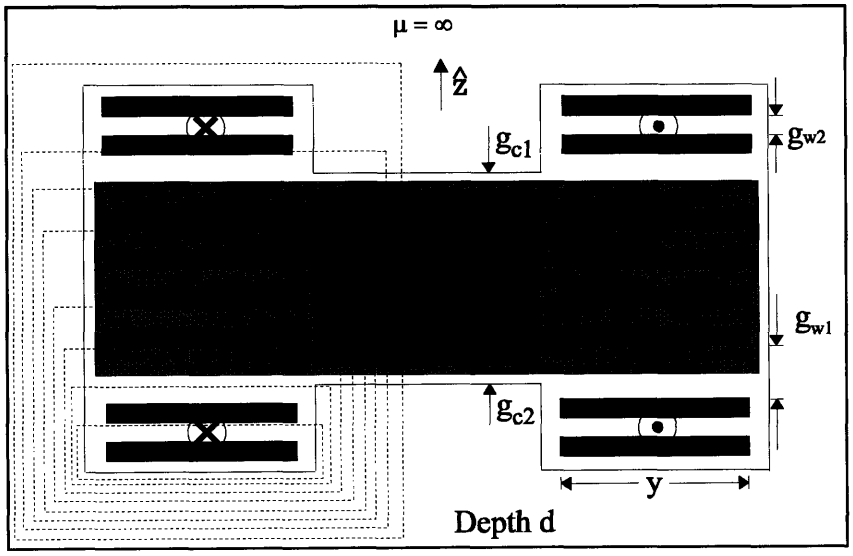

Figure 5.3: Split Secondary Helical Winding Geometry

An exact analytical formula for the leakage inductance in this system is impossible without an analytic field solution, which could then (in theory) be used to find the inductance matrix. However, as described in Chapter 2, the use of the integral forms of Ampere's and Gauss's Laws combined with a number of simplifying approximations facilitates a solution for the fields between the individual windings. Understanding these approximations is an important part of the process, since not all may hold in all cases. The most important of the approximations is that the field strength within any given interwinding space is constant. This is not really the case due to the circular geometry of the windings. As is shown in Section 3.4.1, the current density within the windings is proportional to *1/r*. The crowding of the current toward the inside indicates that the field strength will be larger near the center as well. The radial dependence is restored in the next section for comparison. It is also assumed that the windings extend to within a negligible distance of the core material to eliminate fringing.

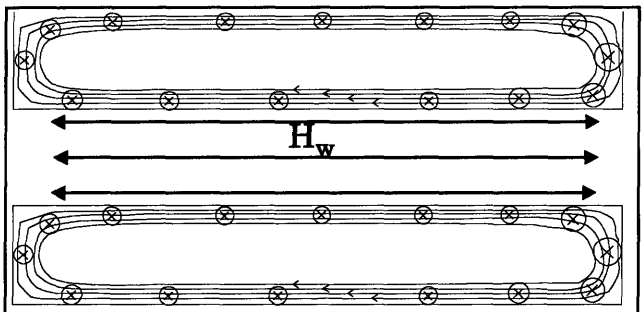

Figure 5.4: Interwinding Field Structure with Skin Effect

In addition, it is assumed that the interwinding fields have no vertical components. This is most accurate at high frequencies or with thick windings when the skin effect prevents the field from penetrating the windings, as shown in Figure 5.4. At lower frequencies or with thinner

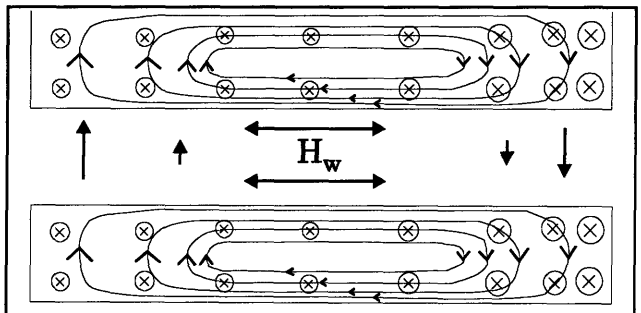

Figure 5.5: Interwinding Field Structure without Skin Effect

conductors, the vertical field component becomes significant, as shown in Figure 5.5.

Finally, in order to simplify the expression of Ampere's Law, it is assumed that the core has no reluctance. While not precisely true, it is a sensible assumption to make because the actual permeability of the core is greater than 1000 times that of air, while the path lengths in both sections are roughly equivalent. Thus, there are nine magnetic field variables to solve for in this simplified system corresponding to the seven interwinding spaces and the two core gaps. The nine equations used to solve the system are as follows: Ampere's Law can be applied in integral form around eight contours that surround one to eight of the windings. These contours are shown in Figure 5.3. The ninth equation is conservation of magnetic flux, where the contour used is a closed surface around the puck. The dimensions of the system are also given in Figure 5.3, and for the purposes of this derivation, the assumption is made that $g_{c1} = g_{c2} = g$. The gap measurements include both the air gap between primary and secondary windings and the insulation over the four core faces.

Taking the contour surrounding all eight windings first, Ampere's Law states that

$$H_{g1}g + H_{g2}g = 0 \qquad \Rightarrow \qquad H_{g1} = -H_{g2} \tag{5-1}$$

where both gap fields are defined as positive in the +z direction. The interwinding fields are defined to be positive in the -r direction, and the remaining seven Ampere's Law contours give the following results:

$$H_{w1} = \frac{I}{y} \qquad\qquad H_{w7} = \frac{-I}{y}$$

$$H_{w2} = \frac{2I}{y} \qquad\qquad H_{w6} = \frac{-2I}{y}$$

$$H_{w3} = \frac{I}{y} + H_{g1}\frac{g}{y} \qquad\qquad H_{w5} = \frac{-I}{y} + H_{g1}\frac{g}{y}$$

$$H_{w4} = H_{g1}\frac{g}{y}$$

Next, the statement of conservation of magnetic flux around the removable puck is:

$$\mu_0\left[H_{g1}A_{puck} - H_{g2}A_{puck} - 2H_{w3}g_{w2}d - 2H_{w4}g_{w2}d - 2H_{w5}g_{w2}d\right] = 0$$

$$\therefore\ 2\left[H_{g1}A_{puck} - g_{w2}d(H_{w3} + H_{w4} + H_{w5})\right] = 0$$

$$\therefore\ \left[H_{g1}A_{puck} - g_{w2}d(3H_{g1}\tfrac{g}{y})\right] = 0$$

$$\therefore\ H_{g1}A_{puck} = H_{g1}3g_{w2}d\tfrac{g}{y} \qquad (5\text{-}2)$$

Since the field variables cancel out of the equation, it must be concluded that

$$H_{g1} = H_{g2} = 0. \qquad (5\text{-}3)$$

Note that the symmetry of the system averted a problem with a simplifying approximation. The ferrite puck actually overlaps the interwinding space between windings two and three and between six and seven. However, since the fields in those spaces are equal in magnitude and opposite in direction, their contributions to the flux through the puck surface cancel. Complications like this are avoided solely because of the symmetry of the field values. Thus, the seven interwinding fields become

$$H_{w1} = \tfrac{I}{y} \qquad H_{w7} = \tfrac{-I}{y}$$
$$H_{w2} = \tfrac{2I}{y} \qquad H_{w6} = \tfrac{-2I}{y}$$
$$H_{w3} = \tfrac{I}{y} \qquad H_{w5} = \tfrac{-I}{y}$$
$$H_{w4} = 0$$

Calculating the total stored magnetic energy in the system is simply a matter of adding the contributions from each non-zero field. However, keeping in mind the fact that this derivation assumed zero reluctance return in the core, it appears that these fields correspond to only the shaded portions of Figure 5.6, where the contours can be completed within the core material as soon as the interwinding space is exited.

For the areas where the winding is only partially surrounded by core material, a new field derivation must be obtained. The analysis to calculate the fields in the remaining areas takes advantage of the fact that both primary and secondary are being equally driven.

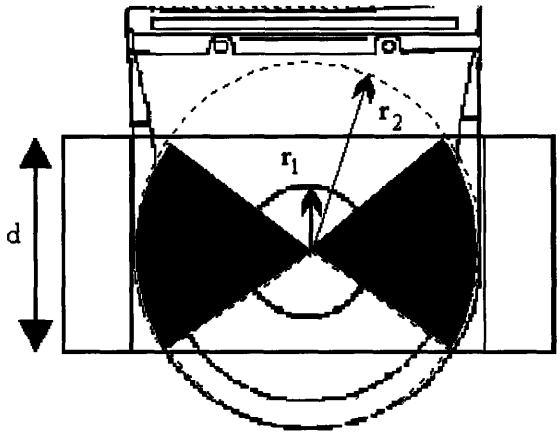

Figure 5.6: Limitations of Circular Field Value Accuracy

$$\theta_{\min} = \sin^{-1}(\tfrac{d}{2r_2}) = 0.69870\ radians = 40\ degrees \qquad (5\text{-}4)$$

Examining Figure 5.7 and choosing a contour around both the primary and secondary coils, thus enclosing the entire current carrying portion of the transformer, results in no net enclosed current. This shows that while there might be residual fields due to the separation of the current sources, in general, there cannot be much field outside the transformer.

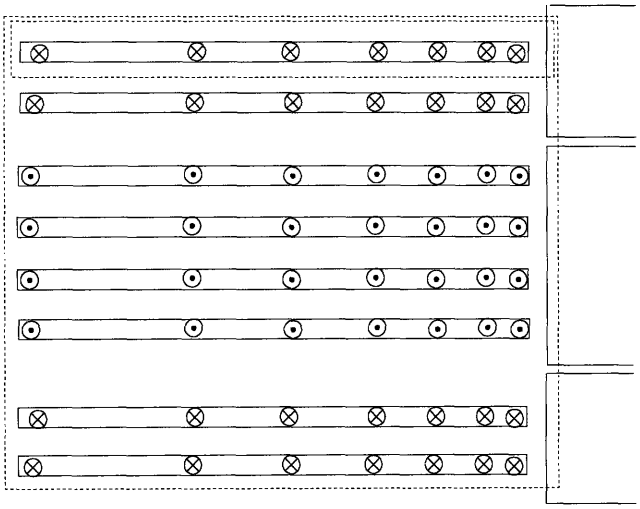

Figure 5.7: Field Approximation Outside Core Material

In addition, there is no field between the outer coils and the core material, so any field that exists in the section not surrounded by core material must go to zero near the core to

satisfy continuity. The analysis that follows will pretend that these residual fields are small enough to be negligible. The error due to this assumption will give falsely high field values, so the leakage inductance value eventually reached will be an upper bound. Again assume that the significant fields are only in the horizontal direction. Taking the same contours as in the previous derivation, the answer turns out to be exactly the same. This makes sense because the only differences between this case and the previous one were any vertical fields at the outer edge of the windings (which are assumed to be zero) and the upper and lower borders, which were enclosed in core material before, and which are now being assumed to be negligible.

Therefore, when the fields previously calculated are integrated, rather than using the depth of the core, the length of the winding will be used. If the field varied as a function of radius (as it actually does) this would require a cylindrical geometry integration to consider the difference between the inside and outside circumference. However, the constant field approximation simple multiplication by the winding area to be used for the horizontal integration. Performing this integration yields

$$U_{total} = \tfrac{\mu_0}{2} A_{winding} (H_{w1}^2 g_{w2} + H_{w2}^2 g_w + H_{w3}^2 g_{w2} + H_{w5}^2 g_{w2} + H_{w6}^2 g_{w1} + H_{w7}^2 g_{w2}) \quad (5\text{-}5)$$

which simplifies by symmetry to

$$U_{total} = \mu_0 A_{winding} \left[H_{w1}^2 g_{w2} + H_{w2}^2 g_{w1} + H_{w3}^2 g_{w2} \right] \quad (5\text{-}6)$$

Plugging in the formulas for the interwinding fields , the equation becomes

$$U_{total} = \mu_0 A_{winding} \left[2 \tfrac{I^2}{y^2} g_{w2} + \tfrac{4I^2}{y^2} g_{w1} \right] = \frac{2\mu_0 A_{winding} I^2}{y^2} (g_{w2} + 2g_{w1}) \quad (5\text{-}7)$$

and from Section 2.3.2, we have that

$$L = \frac{2U_{total}}{I^2} \quad (5\text{-}8)$$

Therefore, the formula for the total equivalent leakage inductance in this system becomes

$$L_{equivalent\_leakage} \approx \frac{4\mu_0 A_{winding}}{y^2}(g_{w2} + 2g_{w1}). \tag{5-9}$$

Dividing this value by two yields the leakage inductance for either side.

$$L_{leakage} \approx \frac{2\mu_0 A_{winding}}{y^2}(g_{w2} + 2g_{w1}). \tag{5-10}$$

Finally, find a numeric value using probable dimensions for the Hughes charging system:

$$\begin{aligned}
&y = 0.02m && (r_i = 38.3mm,\ r_o = 58.3mm)\\
&d = 0.075m && (\approx 3")\\
&g = 0.000375 && (total\ gap = 0.75mm)\\
&g_{w1} = 0.0045m && (g_{w1} \approx 8mm - 3.5mm)\\
&g_{w2} = 0.0012m && (g_{w2} \approx \tfrac{8mm-3.5mm}{3\ spaces})\\
&A_{winding} = 0.00607m^2
\end{aligned}$$

$$L_{leakage} = 0.39\ \mu H.$$

5.3.1.2 Split Secondary, Cylindrical Field Geometry

It is useful to examine the leakage inductance when the simplifying approximation of constant interwinding fields is removed. The derivation in Chapter 3 demonstrates that the current density within each turn of a helical winding is approximately given by

$$\bar{J} = \frac{I_0}{t \ln(r_o / r_i) r}\hat{\theta}. \tag{5-11}$$

Using this formula, it is theoretically possible to find a solution using magnetoquasistatic field theory for the magnetic field within each conductor of the Helical winding as well as the interwinding spaces. First, a particular solution would be found that satisfies the current source given above in (5-11). Next, boundary conditions would be set up to partition the interwinding spaces into manageable pieces. These conditions would require

that the tangential magnetic field be zero at the surfaces of the ferrite core, and that all magnetic fields be continuous across the boundaries between sections. The homogeneous portion of the total field solution could be derived from a magnetic vector field that satisfies Laplace's equation as long as the total field satisfies the boundary conditions.

This process could be simplified slightly by neglecting the difference between conducting areas and interwinding space areas. This simplification would model the winding volume as a continuous field of current density such that the current's radial dependence as well as the total was identical to the actual case. However, one drawback of this method would be that the field solution would be continuous as well, while the actual solution would be discontinuous since the current density is discontinuous. An alternate approximation takes advantage of the geometric structure of the winding as well as the results of the skin effect upon the problem. Within the bulk of the winding pack, most of the volume is actually filled by interwinding insulation rather than conductor. In addition, the formula given for the current density within the windings assumed no variation in the z direction. Because of these modeling approximations, the conductor can be treated essentially as a current sheet when solving for the fields, eliminating the need for a particular solution. The influence of the skin effect upon the field solution is to make the magnetic field essentially horizontal for most of the distance between the windings. Vertical fields can only penetrate into the conductor up to about one skin depth on each edge, leaving the fields in the main center region primarily horizontal. Because the fields inside and outside the conductor must be continuous at the surface, the fields between the windings will also be primarily horizontal.

Once the system has been simplified this far, the only variable that must be solved for is the strength of the horizontal field between the conductors, which can be done by

calculating Ampere's Law in integral form over a continuous range of contours surrounding progressively more of one winding, as shown in Figure 5.8.

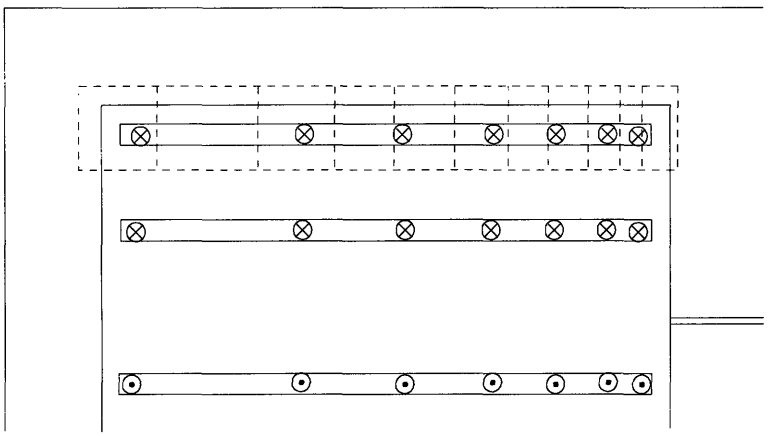

Figure 5.8: Circular Field Approximation for Helical Winding Structure

As before, the core is assumed to have no reluctance, and the space between the windings and the core on either side is negligible. This series of calculations results in the following set of formulas for the horizontal magnetic fields:

$$H_{w1} = \frac{I_0}{\ln(r_o / r_i) r}\hat{r} \qquad H_{w5} = \frac{-I_0}{\ln(r_o / r_i) r}\hat{r}$$

$$H_{w2} = \frac{2I_0}{\ln(r_o / r_i) r}\hat{r} \qquad H_{w4} = 0 \qquad H_{w6} = \frac{-2I_0}{\ln(r_o / r_i) r}\hat{r}$$

$$H_{w3} = \frac{I_0}{\ln(r_o / r_i) r}\hat{r} \qquad H_{w7} = \frac{-I_0}{\ln(r_o / r_i) r}\hat{r}$$

The next step in the leakage calculation is to find the total stored magnetic energy due to these fields. As in the case of the rectangular field geometry analysis, the contours which derived these field values were placed within the core material on three sides. However, the same set of assumptions that extended the field values in that case from the enclosed areas to the open ones are valid here as well. However, because of the radial

dependence, the integral must be evaluated in cylindrical coordinates. Calculating the energy in the magnetic fields becomes simple once the symmetry is taken into account. The equation for stored energy in this case is:

$$U_{total} = 2\left[\tfrac{\mu_0}{2}\int H_{w1}^2 \cdot dV_1 + \tfrac{\mu_0}{2}\int H_{w2}^2 \cdot dV_2 + \tfrac{\mu_0}{2}\int H_{w3}^2 \cdot dV_3\right] \tag{5-12}$$

$$U_{total} = 2\left[\tfrac{\mu_0}{2}\int \frac{I_0^2}{\ln(r_o/r_i)^2 r^2}\cdot rdzdrd\theta + \tfrac{\mu_0}{2}\int \frac{4I_0^2}{\ln(r_o/r_i)^2 r^2}\cdot rdzdrd\theta + \tfrac{\mu_0}{2}\int \frac{I_0^2}{\ln(r_o/r_i)^2 r^2}\cdot rdzdrd\theta\right]$$

$$= \mu_0 I_0^2\left[2\int \frac{dzdrd\theta}{\ln(r_o/r_i)^2 r} + \int \frac{4dzdrd\theta}{\ln(r_o/r_i)^2 r}\right]$$

$$= \mu_0 I_0^2\left[\frac{2g_{w2}(2\pi)}{\ln(r_o/r_i)} + \frac{4g_{w1}(2\pi)}{\ln(r_o/r_i)}\right] = \frac{4\pi\mu_0 I_0^2}{\ln(r_o/r_i)}\left[g_{w2} + 2g_{w1}\right] \tag{5-13}$$

As in the case of the rectangular geometry derivation, note that the accuracy of this calculation in the case of the MagneCharge charger is reduced slightly due to the fact that the windings don't reach to the outer edge of the paddle. Using the same dimensions as before for all other variables, the resulting stored energy is

$$U_{total} = 3.834 \times 10^{-7}\ Joules$$

and the leakage inductances values are

$$L_{leak} = 0.38\ \mu H.$$

5.3.1.3 Single Secondary, Rectangular Field Geometry

For comparison, it is useful to examine the case where the secondary is not separated into two pieces. All the same approximations will be made as in the previous cases, and the same dimensions will be used for consistency. Because of the negligible differences between the cylindrical and rectangular geometry results already derived, rectangular dimensions will be used here for simplicity. All significant differences in the

derivation for this geometry result from the lack of symmetry that proved so useful before. Figure 5.9 shows the cross-section of the core used in this analysis.

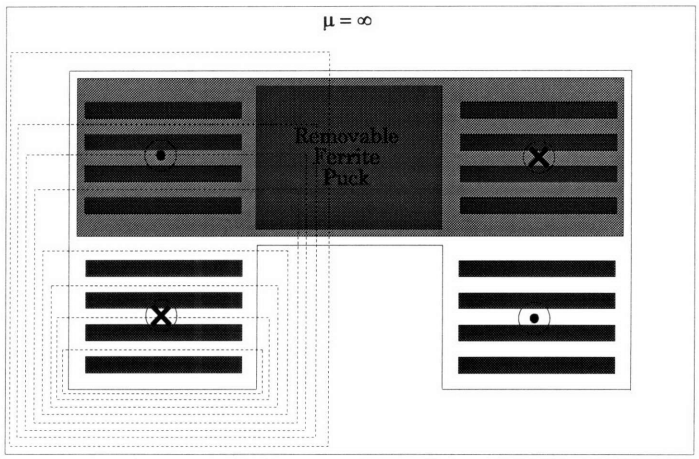

Figure 5.9: Single Sided Helical Winding Geometry

It will be found that the peak fields are higher, resulting in much larger leakage inductance. In addition, the confidence level in the result is lower since symmetry is not present to cancel out many of the unmodeled effects. As before, there are seven interwinding fields to solve for, as well as the two fields in the core gaps. Using the same process as before, Ampere's Law can be used to state that:

$$H_{w1} = \frac{I}{y} \qquad H_{g1} = -H_{g2}$$
$$H_{w2} = \frac{2I}{y} \qquad H_{w5} = \frac{3I}{y} - H_{g1}\frac{g}{y}$$
$$H_{w3} = \frac{3I}{y} \qquad H_{w6} = \frac{2I}{y} - H_{g1}\frac{g}{y}$$
$$H_{w4} = \frac{4I}{y} \qquad H_{w7} = \frac{I}{y} - H_{g1}\frac{g}{y}$$

Once again using conservation of flux through the surface of the puck with the approximation of rectangular geometry and ignoring the field contribution of H_{w4},

$$\mu_0\left[H_{g1}A_{puck} - H_{g2}A_{puck} - 2g_{w2}d(H_{w5} + H_{w6} + H_{w7})\right] = 0 \qquad (5\text{-}14)$$

Plugging in the formulas for the interwinding fields simplifies the equation to

$$2A_{puck}H_{g1} = 2g_{w2}d(\tfrac{6I}{y} - 3H_{g1}\tfrac{g}{y})$$

$$\therefore\ H_{g1}(2A_{puck} + 6\tfrac{g_{w2}dg}{y}) = 12\tfrac{g_{w2}dI}{y}$$

$$\therefore\ H_{g1} = \frac{6g_{w2}dI}{yA_{puck} + 3g_{w2}dg} \qquad (5\text{-}15)$$

This formula for the field in the core gap can be plugged into the interwinding field formulas to specify their values completely in terms of geometry and the driving current. However, it is simpler in this case to find field values for a unit current input and use numerical values to calculate the leakage. Because the area of the puck cross-section appears in the expression for the core gap field, this dimension must be measured as well.

$$A_{puck} = 0.00312\ m^2 \qquad (r_{puck} = 0.0315\ m)$$

Plugging in the dimensions, the field values are found to be (in amperes per meter):

$$H_{g1} = -H_{g2} = 8.65$$

$H_{w1} = 50$		$H_{w7} = 49.84$
$H_{w2} = 100$	$H_{w4} = 200$	$H_{w6} = 99.84$
$H_{w3} = 150$		$H_{w5} = 149.84$

Note that the effect of the nonzero fields in the core gaps is negligible, causing errors of less than one percent in the interwinding field values if ignored. The energy in the gap fields may also be ignored when calculating the leakage inductance. The presence of the fields signifies coupling between the primary and secondary windings, but the contribution of the energy due to the fields is negligible as the energy is proportional to the square of the field strength. The formula for the total stored magnetic energy here is

$$U_{total} = \tfrac{\mu_0}{2} A_{winding}\left[g_{w2}(H_{w1}^2 + H_{w2}^2 + H_{w3}^2 + H_{w5}^2 + H_{w6}^2 + H_{w7}^2) + g_{w1}H_{w4}^2\right] \qquad (5\text{-}16)$$

which at one ampere yields 1.01×10^{-6} Joules. Thus, the leakage inductances are

$$L_{leakage} = 1.01\ \mu H$$

which is more than double the value calculated for the split secondary case. Note that the core gap fields were not included in the final energy calculation. Their contribution would have been 1.10×10^{-10} Joules, or 0.22 nanoHenries, which explains why they were left out. Looking at the difference between the interwinding fields affected by the core gaps and the ones which weren't suggests that this effect was negligible as well.

5.3.2 Prototype and Simulation Analysis

Because of the bobbin, the 2.6 mil thick copper windings in the Helical prototype were only 1 cm wide with an inner radius of 2.25 cm. The windings were insulated from each other with 2 mil plastic tape, although the curvature of the helix was erratic enough to cause some buckling in the structure that increased the interwinding gaps to approximately 0.5 mm. The primary was separated from the secondary by about 3 mm.

Since the dimensions vary for each prototype, theoretical values will be derived for each of the circuit elements before the measurement results are presented. Parasitic capacitances and core losses were considered too negligible at the operating point to attempt direct measurements, and their measured values will be taken on faith.

The theoretical magnetizing inductance is common to all four prototypes, so the derivation is presented in Appendix B. The result, ignoring fringing, is **6.68 μH** for an air gap between the two core halves of 1 mm, and rises to **7.90 μH** if some of the fringing is accounted for. To estimate the Helical prototype leakage inductance, the derivation from Section 5.3.1.3 will be used because the prototype had a single-sided secondary. This results in a total equivalent leakage inductance of 1.35 μH, or **0.67 μH** on each side of the circuit model. Using the formula provided in Chapter 3 for determining the DC resistance of a coil, the resistance of each winding is **22.9 mΩ**.

Using the MATLAB script to curve fit the driving point impedance functions to the data, with the assumptions that values were identical on both sides of the transformer, the following values were obtained.

Magnetizing Inductance:	**8.2 μH**
Leakage Inductance:	**0.62 μH**
Winding Resistance:	**25 mΩ**
Core Losses:	**761 Ω**
Shunt Capacitance:	**53 pF**

Note that although the resistance value found by the regression procedure was slightly above the predicted value, the DC resistance value measured by the HP 4192A impedance analyzer, to its precision, was exactly the expected value.

For the simulations done without eddy current analysis, the total energy in the full system with an open secondary and one ampere in the primary was 4.6688×10^{-6} Joules, making $L_{open} = 9.34\ \mu H$. With one ampere in both primary and secondary, but opposite directions, the total energy was 4.4692×10^{-7} Joules. This results in inductance values of

$$L_{mag} = 8.89\ \mu H \qquad \textit{and} \qquad L_{leak} = 0.45\ \mu H.$$

The inductance matrix returned by Maxwell gave identical results.

When 80 kHz eddy currents in the core material were included in the computer simulation, the total stored energy in the system dropped to 2.3722×10^{-6} Joules. This is just over half the previous value but taking into account the AC inductance calculation described in Chapter 4, actually corresponds to a slight increase in the inductance to a value of $L_{open} = 9.49\ \mu H$. The resistivity value used in the simulation was 1.0 Ohm-meters, which assumes quite a bit of degradation from the nominal value of 10 Ohm-meters. Unfortunately, the aspect ratio limit of 10:1 for simulation mesh generation prevented accurate modeling of the individual conductors. Assuming that at higher frequencies, the leakage fields are forced around the windings rather than penetrating

through them, the winding blocks must be split into the individual conductors to get a true field distribution. This created volumes with such extreme aspect ratios that the iterative solution process was unable to converge on a stable field distribution. Since the change was a reduction in leakage inductance, the DC value will be used as an upper bound. This places the 80 kHz magnetizing inductance around **9.04 μH**.

This is not the expected result, until it is noted that the skin depth of the fields in the core is 5 cm for the resistivity and frequency chosen, but the core radius is only 1.5 cm. Thus, there is essentially no magnetic shielding present at all and the inductance discrepancy arises solely from inherent inaccuracies due to the coarser mesh resolution in the eddy current simulation. The same phenomenon will be seen in Chapter 6 with simulations of the commercial system. In that case, the simulated resistivity will be lowered still further to demonstrate the effects of magnetic shielding in the core. For now, however, the simulation has shown that operation at 80 kHz has little effect upon the magnetizing inductance of the prototype transformers due to the small core size and high resistivity.

5.3.3 Flux Tube Simulation

In order to investigate the problem with the center and side leg field levels described in Chapter 4, a flux tube model of the system was created and evaluated in Spice to determine the flux levels through various parts of the system. The flux tube model is essentially just a three-dimensional reluctance network where the core and surrounding air regions are broken into many volumes, or "tubes," and the reluctance of each is inserted as a resistor into the network. For any reasonably accurate model of a system, this requires a large number of reluctances, so the network was analyzed by Spice rather than by hand. In addition, flux is constrained to go in only one direction, forcing the designer to simplify the model if the actual field vectors have multiple components.

One drawback to the flux tube analysis method is that the designer's intuition about where the flux is traveling has a large effect on calculated results, so this type of analysis is probably only good for determining whether another measurement, such as from a prototype or computer, is reasonable. In the case studied, however, the model proved useful by verifying the experimental result that fringing fields can have a major impact upon the field distribution.

The flux tube simulation found in Appendix C reflects one possible level of model complexity for the Helical geometry. It assumes that only the primary is driven and therefore corresponds to the open-circuit leakage inductance test. The results show significantly higher flux density in the center leg than the outside legs, and also give the total flux in the system as 4.969×10^{-7} webers. However, only one quarter of the system was modeled, taking advantage of two planes of symmetry. This adjustment raises the total system flux to 1.988×10^{-6} webers. This flux is linked by the four turns of the primary, making the flux linkage 7.950×10^{-6} webers and since the electric current flowing in the circuit is only 1 ampere, the predicted open circuit inductance value is 7.950 μH.

5.4 Concentric Winding

In contrast to the helical structure of the previous section, in which the conductors were horizontally wrapped around the core with all conductors adjacent to one another, Figure 5.1b shows a configuration where all conductors are vertically oriented and concentrically wrapped. To separate the primary winding from the secondary, the core must be cut so as to slide the inner winding out along the long axis of the core's center leg.

As shown in the previous leakage derivations, there are two main parts to the calculation. First, the interwinding fields must be calculated using Ampere's law and

conservation of flux. Next, the fields are integrated to find the stored magnetic energy. Examining the cross-sections of this Concentric geometry in comparison to the Helical geometry, it becomes clear that the field derivations in both cases are similar, since rotation by 90 degrees of the conductor cross-sections in the Helical case (single sided secondary) produces the cross-section of the Concentric case. The only questionable difference is the fields in the core gaps. In the Helical geometry, it was demonstrated that the air gap fields were negligible, both in terms of their effect on the interwinding fields, and in their contribution to the total stored magnetic energy. The Concentric geometry will take these fields into account as well and show that once again they are negligible, although larger than in the Helical case because of the way the core is cut.

Having shown the interwinding field derivation in the Concentric geometry to be identical to the derivation in the Helical case, the stored energy must be found, and here the two cases differ. Both geometries are distributed leakage transformers, but in the Helical case, the integration volumes were cylinders of the same inner radius and thickness but different heights. In the Concentric case, the cylinders have constant height, but different radii and thicknesses. These dimensional differences highlight the advantage of using one geometry over the other, since physical constraints might make the aspect ratio more favorable to one geometry.

5.4.1 Leakage Derivation

Using the same dimensions as in previous derivations, a clockwise traversal, with Ampere's Law, of the contours shown below yields:

$$H_{g1} = -H_{g2} \qquad H_{w4} = \tfrac{4I}{y} - H_{g1}\tfrac{g}{y}$$
$$H_{w1} = \tfrac{I}{y} - H_{g1}\tfrac{g}{y} \qquad H_{w5} = \tfrac{3I}{y} - H_{g1}\tfrac{g}{y}$$
$$H_{w2} = \tfrac{2I}{y} - H_{g1}\tfrac{g}{y} \qquad H_{w6} = \tfrac{2I}{y} - H_{g1}\tfrac{g}{y}$$
$$H_{w3} = \tfrac{3I}{y} - H_{g1}\tfrac{g}{y} \qquad H_{w7} = \tfrac{I}{y} - H_{g1}\tfrac{g}{y}$$

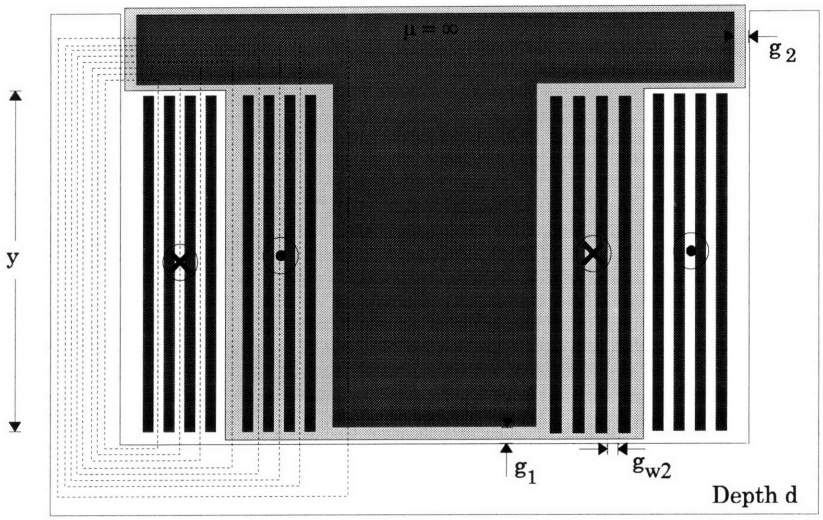

Figure 5.10: Concentric Winding Geometry

In this derivation, the fields in the core gaps are still defined as positive for a flux path going up through the center leg and down the outer legs. The interwinding fields have been defined as positive in the -z direction, however.

Again surrounding the removable ferrite core with a closed surface contour, conservation of flux states that

$$\mu_0\left[H_{g1}A_{puck} - 2H_{g2}A_2 - 2g_{w2}d(H_{w1}+H_{w2}+H_{w3}+H_{w5}+H_{w6}+H_{w7}) - 2g_{w1}dH_{w4}\right] = 0$$

A_{puck} and A_2 are not specified in the drawing, but assume that $A_{puck} = 2A_2$ for simplicity.

$$\therefore\ H_{g1}A_{puck} = g_{w2}d(H_{w1}+H_{w2}+H_{w3}+H_{w5}+H_{w6}+H_{w7}) + g_{w1}dH_{w4} \qquad (5\text{-}17)$$

Plugging in the formulas for the interwinding fields results in

$$H_{g1}A_{puck} = (\tfrac{12I}{y} - \tfrac{6g}{y}H_{g1})g_{w2}d + (\tfrac{4I}{y} - \tfrac{g}{y}H_{g1})g_{w1}d$$

$$\therefore\ H_{g1}(A_{puck}+\tfrac{6g_{w2}gd}{y}+\tfrac{g_{w1}gd}{y})=(\tfrac{12g_{w2}d}{y}+\tfrac{4g_{w1}d}{y})I$$

$$\therefore\ H_{g1}=\frac{12g_{w2}d+4g_{w1}d}{A_{puck}y+6g_{w2}gd+g_{w1}gd}I \tag{5-18}$$

Again, this can be plugged back into the formulas for the interwinding fields, and again, it is simpler to solve numerically from here on. For one ampere of driving current in both primary and secondary windings, the fields in the system are (in amperes per meter):

$$\begin{aligned} H_{g1} &= -H_{g2} = 33.31 & H_{w4} &= 199.38 \\ H_{w1} &= 49.38 & H_{w5} &= 149.38 \\ H_{w2} &= 99.38 & H_{w6} &= 99.38 \\ H_{w3} &= 149.38 & H_{w7} &= 49.38 \end{aligned}$$

The calculation of stored energy follows a slightly different path this time, since the windings are oriented vertically instead of horizontally. Assume that the innermost winding is at a radius corresponding to the inner radius of the flat windings. This sets r_i to 38.3 mm. Once again, adding the stored energies from the interwinding fields results in

$$U_{total}=2\pi(2r_1+6g_{w2}+g_{w1})g_{w2}y\left[\tfrac{\mu_0}{2}H_{w1}^2+\tfrac{\mu_0}{2}H_{w2}^2+\tfrac{\mu_0}{2}H_{w3}^2+(\tfrac{\mu_0}{2}H_{w4}^2\tfrac{g_{w1}}{2g_{w2}})\right]$$

$$\therefore\ U_{total}=\mu_0\pi(2r_1+6g_{w2}+g_{w1})g_{w2}y\left[(H_{w1}^2+H_{w2}^2+H_{w3}^2)+\tfrac{1}{2}H_{w4}^2\tfrac{g_{w1}}{g_{w2}}\right] \tag{5-19}$$

$$\therefore\ U_{total}=9.13\times10^{-7}\ \text{Joules}$$

$$L_{leakage}=0.91\,\mu H.$$

Once again, the core gap fields were not included in the final calculation. In this case, their contribution would have added 1.63×10^{-9} Joules to the total energy, which increases the total equivalent leakage by 3 nanoHenries. Ignoring them altogether in the calculation would have added at most 1.2 percent error to the interwinding field values, which is quite reasonable considering the other approximation errors present.

Although the 9.4 percent leakage difference between the corresponding Helical and Concentric cases might suggest that the Concentric geometry is superior, the difference turns out to be purely due to volume differences. For the same dimensions of thickness, winding width, and inner radius, it turns out that the Concentric geometry takes up ten percent less volume, and this is exactly the difference between the leakage values.

5.4.2 Prototype and Simulation Analysis

The Concentric prototype transformer used 50 mm wide copper strips that were insulated by standard photocopying paper. Again, winding imperfections increased the interwinding spacing somewhat, to around 0.4 mm. The space between the two winding packs was the same as between the individual conductors.

As with the Helical prototype, the predicted magnetizing inductance is **7.90 μH**. Because the total thickness of the conductors and the insulation is so thin, 45 mm was used as the diameter of all windings in the leakage inductance and winding resistance derivations. The resulting leakage inductance values are **0.031 μH,** assuming that both primary and secondary leakages are identical, and the predicted winding resistance is **3.8 mΩ**. The results of the regression curve fit for the 4:4 Concentric prototype were

Magnetizing Inductance:	**8.3 μH**
Leakage Inductance:	**0.04 μH**
Winding Resistance:	**6 mΩ**
Core Losses:	**791 Ω**
Shunt Capacitance:	**233 pF**

As predicted in [11], the reduction in leakage inductance (due to the increased winding width) was accompanied by an increase in the parasitic capacitance value. Also note that again, the computer generated winding resistance value is slightly higher than the

predicted value, even though the lowest frequency data point corresponded to the predicted value exactly.

Maxwell simulation of the system without eddy currents yielded 4.4420×10^{-6} Joules for the open circuit case. Unfortunately, the simulation was unable to converge on a value for the case where both the primary and secondary were driven equally, even with the windings modeled as single blocks. This was probably due to the large aspect ratio of the windings and the high concentration of the magnetic field within the narrow space between the conductors. On three passes of adaptive mesh generation, the system energies returned were 2.4308×10^{-8} Joules, 9.2202×10^{-8} Joules, and 5.5184×10^{-8} Joules for the full system. Assuming that the largest value places a bound on the actual leakage inductance, the result for equal primary and secondary leakage values would be less than 0.092 μH. This would yield values of

$$L_{mag} = 8.82\ \mu H \qquad and \qquad L_{leak} = 0.09\ \mu H.$$

For another estimate of the inductance values, the inductance matrix produced by the software can be calculated. Since the simulation takes into account the difference in radius between the primary and secondary windings, the leakage inductances are slightly different for the two sides when calculated using the inductance matrix. Maxwell returns an inductance matrix that, when adjusted for symmetry and the number of turns in each winding pack gives

$$L_{matrix} = \begin{bmatrix} 8.896\mu H & 8.864\mu H \\ 8.864\mu H & 8.960\mu H \end{bmatrix}.$$

which results in circuit inductance values of

$$L_{mag} = 8.86\ \mu H, \qquad L_{leak_p} = 0.032\ \mu H, \quad and \qquad L_{leak_s} = 0.096\ \mu H.$$

The difference between the primary side leakage and secondary side leakage reflects the asymmetry in the system that the theoretical and prototype calculations couldn't take into

account. Although there is no guarantee that the inductance matrix converged more accurately than the energy method, it does correctly reflect the larger leakage value due to the larger secondary radius. Whether the actual difference is 300 percent is unknown.

For high frequency analysis of the system, the open-circuit value for total stored energy can be taken as the value calculated in the Helical case, since the open-circuit energy is relatively independent of winding geometry. No high frequency leakage inductance estimate was even attempted since the simulation failed at DC.

5.5 Adjacent Winding

So far, two geometries have been analyzed that, ignoring core gap fields, had the same leakage field derivations but different volume integrations. The Adjacent winding geometry is a case where the field derivation is quite different with very different results as well. Once again, however, the basic assumption will be that fields have only one component in any one interwinding space. Considering the aspect ratios involved, this may not seem like a very good approximation, but simulation will be used to show that this is reasonable.

5.5.1 Leakage Derivation

The structure of the Adjacent geometry transformer creates a two dimensional network of interwinding fields. This poses a slight problem in the formulation of contours around which to apply Ampere's law. A vertical contour running through both windings, as shown on the right side of Figure 5.11, only shows that the fields in the primary interwinding spaces are equal and opposite to those of the secondary. Assuming that there are non-zero horizontal fields between the primary and secondary, contours can be placed around just one quadrant of windings, as shown on the left side of the figure. In reality, the field strength between the primary and secondary coils could be a complex function whose horizontal component fluctuates as a function of radius.

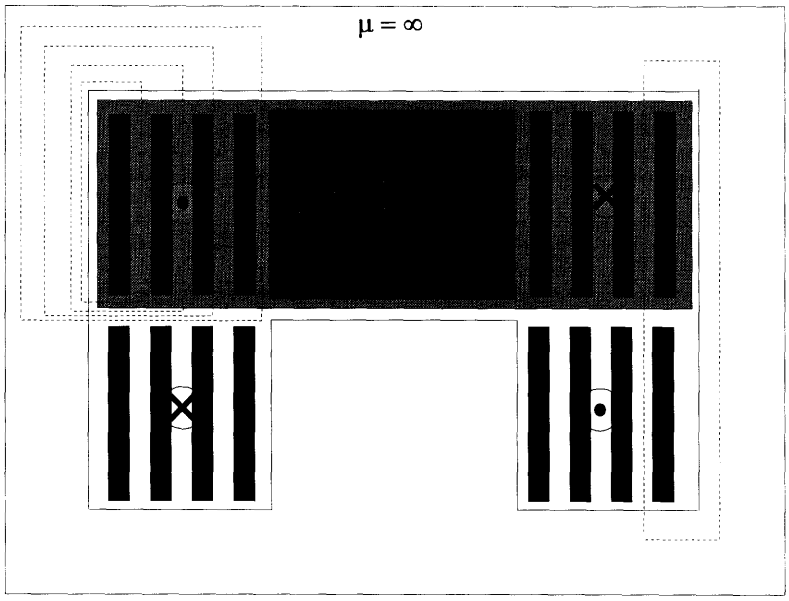

Figure 5.11: Adjacent Winding Geometry

For the sake of making reasonable approximations, it is assumed that the horizontal field takes only four values, corresponding to its strength between each of the four pairs of primary/secondary windings. This division of the horizontal fields is shown in more detail in Figure 5.12. In this derivation, the vertical interwinding fields will be assumed to be positive in the direction leading away from the center, and the horizontal fields will be positive in the negative radial direction. As before, the fields in the core gaps will be positive in the +z direction.

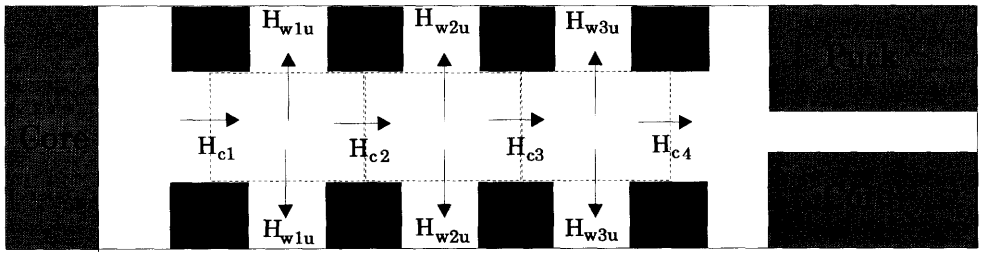

Figure 5.12: Field Analysis for Adjacent Concentric Geometry

There are nine unknowns in the system: three vertical interwinding fields, four horizontal interwinding fields, and two core gap fields. Four independent equations can be derived from contours around the four primary windings. In addition, three equations

can be found from applying conservation of magnetic flux to the three volumes shown in Figure 5.12. Since none of the seven equations listed so far use either of the two core gap fields, this forms a system of seven equations in seven unknowns, and at least within the approximations made so far, the gap fields are independent of the other seven. Because these fields proved negligible in previous calculations, they will be ignored completely here. It is convenient to solve this system in matrix form. The system looks like

$$\begin{bmatrix} y & 0 & 0 & (t+g_{w2}) & 0 & 0 & 0 \\ 0 & y & 0 & (t+g_{w2}) & (t+g_{w2}) & 0 & 0 \\ 0 & 0 & y & (t+g_{w2}) & (t+g_{w2}) & (t+g_{w2}) & 0 \\ 0 & 0 & 0 & (t+g_{w2}) & (t+g_{w2}) & (t+g_{w2}) & (t+g_{w2}) \\ 2g_{w2} & 0 & 0 & -g_{w1} & g_{w1} & 0 & 0 \\ 0 & 2g_{w2} & 0 & 0 & -g_{w1} & g_{w1} & 0 \\ 0 & 0 & 2g_{w2} & 0 & 0 & -g_{w1} & g_{w1} \end{bmatrix} \begin{bmatrix} H_{w1u} \\ H_{w2u} \\ H_{w3u} \\ H_{c1} \\ H_{c2} \\ H_{c3} \\ H_{c4} \end{bmatrix} = \begin{bmatrix} I \\ 2I \\ 3I \\ 4I \\ 0 \\ 0 \\ 0 \end{bmatrix} \quad (5\text{-}20)$$

where t is the thickness of the winding, and g_{w2} is the thickness of the interwinding space. Notice that the horizontal fields are multiplied by $(t+g_{w2})$ in Ampere's Law. This assumes that the windings are one-half of the interwinding thickness away from the ferrite core, making the horizontal path traverse half an interwinding thickness, then a full winding thickness, and then another half interwinding thickness before turning and following the winding vertically.

Plugging in the same values as before, assume that the vertical distance between the primary and secondary windings is g_{w1}. Most likely, the conductors in an actual system will be significantly thinner than the interwinding space or insulation that surrounds them. Assume the winding thickness t to be one-tenth of a millimeter, or 4 mils. Assume that the previous calculations had included the winding thickness as part of the interwinding space because the windings were so thin. Thus, the 0.0001 m should be

subtracted from the previous interwinding thickness to get the new value of 0.0011 m. Plugging in these values, the solution to the system is (in amperes per meter)

$$\begin{bmatrix} H_{1wu} \\ H_{2wu} \\ H_{3wu} \\ H_{c1} \\ H_{c2} \\ H_{c3} \\ H_{c4} \end{bmatrix} = \begin{bmatrix} 0 \\ 0 \\ 0 \\ 833.33 \\ 833.33 \\ 833.33 \\ 833.33 \end{bmatrix}$$

showing that there are no vertical fields between the windings at all. Taking into account the cylindrical shape of the windings and the fact that the field is constant independent of radius, the total stored energy is

$$U_{total} = \tfrac{\mu_0}{2} H^2 (Interwinding\ cylinder\ Vol.) \tag{5-21}$$

$$U_{total} = \left[\tfrac{\mu_0}{2} H^2 \pi((r_i + 4t + 4g_{w2})^2 - r_i^2) g_{w1}\right] \tag{5-22}$$

$$\therefore\ U_{total} = 2.41 \times 10^{-6}\ \text{Joules}$$

$$\therefore\ L_{leakage} = 2.41\ \mu H.$$

Even though the volume occupied by non-zero fields is 10 times smaller than in the other cases, the energy stored is proportional to the field strength squared, and the fields are much stronger in this case than any of the others. If there had been vertical interwinding fields in the Adjacent geometry case, the field integration would have been a cross between the calculations for the Helical and the Concentric cases. With only one non-zero field, however, it becomes a simplified version of the Helical geometry calculation.

5.5.2 Prototype and Simulation Analysis

The Adjacent prototype transformer was constructed identically to the Concentric prototype except that the windings reached only halfway across, so that their width was 31 mm. The distance between the two winding packs varied somewhat because of

winding inconsistencies, but was generally around 5 mm. Unfortunately, the ideal case approximations don't hold for the prototype because of the space around the windings due to the bobbin and the core size. Because of this space, the magnetic path lengths are not as short as they would be if the system looked like Figure 5.11. However, because there is nothing to constrain the fields in the large air gaps between the windings and the core, approximation of the leakage inductance becomes difficult. Using 0.4 mm as the interwinding space as in the Concentric case and pretending that the system were as in Figure 5.11, the short magnetic path lengths cause a predicted leakage inductance of **3.13 μH** with a field strength in the gap of 2222 A/m. With the opposite assumption, that all fields are still horizontal but taking into account the full distance between the core legs, the field strength drops to 200 A/m, but the volume increases. With these assumptions, the net predicted leakage inductance is **0.39 μH**. The true value is probably somewhere in between. Again assuming identical radii for each layer of the conductors to simplify the DC resistance calculation results in a value of **6.1 mΩ**. The curve fit results for this geometry from the actual prototype measurements were

Magnetizing Inductance:	**8.2 μH**
Leakage Inductance:	**0.74 μH**
Winding Resistance:	**8 mΩ**
Core Losses:	**664 Ω**
Shunt Capacitance:	**80 pF.**

Again notice that the capacitance value is larger than the Helical prototype capacitance and less than the Concentric prototype capacitance, just as the Adjacent prototype's winding widths are. The large error in the leakage inductance can be attributed to the difficulty in obtaining approximations to describe the system as expected.

When simulated at DC, values of

$$L_{mag} = 8.16\,\mu H \qquad and \qquad L_{leak} = 1.47\,\mu H$$

were obtained, both through calculation of total system energy and through the inductance matrix. Again, the open-circuit secondary result for high frequency analysis can be taken from the Helical geometry and no leakage inductance determination was attempted due to the aspect ratios of the individual conductors.

5.6 LPKF Winding

The LPKF Geometry is of interest for two reasons. First, although its interwinding field derivation turns out to be identical to the calculation for the Adjacent geometry, the field values and final leakage inductance turns out to be radically different, solely due to dimensional differences. Second, the LPKF geometry is extremely easy to construct using printed circuit board technology, and its nickname has been taken from the machine that produced the laboratory prototypes. The structure is easily fabricated from a copper plated circuit board by removing copper in a spiral pattern to form the interwinding spaces. If a double-sided board is used, etching the reverse side forms the secondary. In this way, two sets of windings are formed with precise control over all dimensions.

5.6.1 Leakage Derivation

Figure 5.13 shows the cross-section of the LPKF geometry. As suggested by the diagram, one disadvantage of the structure is that its aspect ratio for a given winding thickness is so much larger than other designs that it may not be physically practical. Comparing it's structure to that of the Adjacent geometry in Figure 5.11, however, one can immediately see that none of the conductors change position or winding style. The only differences between the two are dimensional. Note also that Figure 5.13 shows a different way from what was suggested in Figure 5.1d of cutting the core to separate the primary and secondary windings.

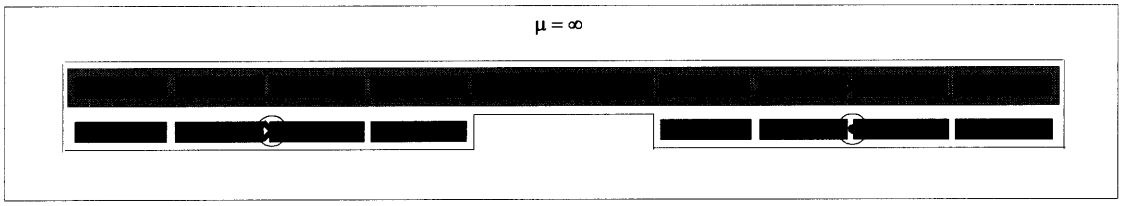

Figure 5.13: LPKF Winding Geometry

Since all of the Ampere's law contours and flux conservation pillboxes are identical to the Adjacent geometry case, this step of the derivation will be omitted. Switching the values for the winding width (y) and thickness (t), however, the horizontal field between the primary and secondary winding becomes

$$H_c = \frac{I}{(y + g_{w2})} = 47.39\ A/m$$

which is essentially the 50 A/m derived for an interwinding space in the Helical or Concentric geometries corresponding to only one conductor. The trick is in the geometry, since drawing a contour around all four conductors shows that there is four times the magnetomotive force, but also four times the length of the flux path. Again using the volume of the interwinding cylinder to compute the stored magnetic energy yields

$$U_{total} = \tfrac{\mu_0}{2} H_c^2 g_{w1} \pi (r_o^2 - r_i^2) \qquad (5\text{-}23)$$

where $r_i = 0.0383 m$

and $r_o = r_i + 4y + 4g_{w2} = 0.1227 m.$

Thus, $U_{total} = 2.711 \times 10^{-7}$ Joules

and $L_{leakage} = 0.27\ \mu H$

Thus, the same mathematical topology resulted in both the worst and the best leakage value for the standardized system, simply by changing the correspondence of the dimensions. Mathematically, for the same conductor dimensions (with t and y swapped), the Adjacent geometry has 35 times less leakage volume, but the squared field strength is lower in the LPKF geometry by a factor of 309!

5.6.2 Prototype and Simulation Analysis

The LPKF machine is designed to quickly produce custom circuit boards, but in this case was used to make the transformer windings by etching out insulation paths to make spiral windings rather than standard traces. The material used was 1/16 inch thick circuit board insulation with 1.4 mils of copper plated on each side. To make a 4:4 transformer, two, four turn spirals were created on both sides in alignment with each other. Leads were connected to both spirals, one attaching at the outer radius, and one at the inner radius.

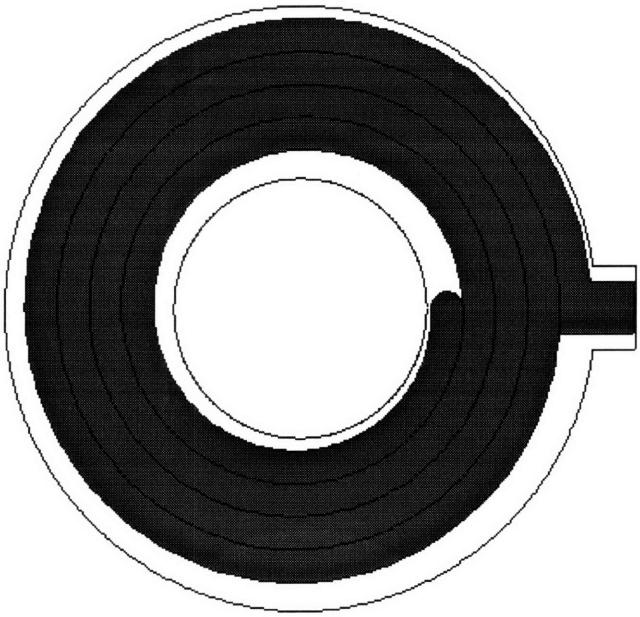

Figure 5.14: LPKF Machined Spiral Transformer Winding

Because of the sturdiness of the board material, the standard bobbin was not used in this prototype, which allowed the inner radius to be reduced to around 15 mm, thereby achieving wider windings and reducing the leakage field strength. This increase in the width helped to offset the fact that by using a true spiral shape to make the windings, 5 winding thicknesses were needed to achieve four turns, as shown in Figure 5.14. All turns in the spirals were of equal width. This results in theoretical values of 0.206 μH for

leakage inductance and 77.6 mΩ for the DC resistance. Notice that the thinner windings in this prototype result in a much higher resistance. In comparison, the curve fit results for this geometry were

Magnetizing Inductance:	**8.3 μH**
Leakage Inductance:	**0.20 μH**
Winding Resistance:	**104 mΩ**
Core Losses:	**672 Ω**
Shunt Capacitance:	**16 pF.**

Simulation of the LPKF geometry at DC yielded a value of 8.88 μH for the open circuit driving point impedance using stored energy techniques. The short circuit impedance, which determines the leakage inductance, was harder to gauge since the simulation failed to converge on one value. The value with the lowest estimated error was 0.12 μH, but the value calculated with the highest resolution mesh was 0.18 μH. Assuming the latter value to be closer to the actual number, this yields

$$L_{mag} = 8.70\,\mu H \qquad and \qquad L_{leak} = 0.18\,\mu H$$

for the two relevant inductances. Because the individual conductors were modeled, no inductance matrix could be calculated for comparison.

Repeating the simulation at 80 kHz with eddy currents in the core and windings yielded $L_{mag} = 9.07\,\mu H$ *and* $L_{leak} = 0.116\,\mu H$.

Whether the leakage value suffers from the same lack of stability as it did in the DC case is not clear since only two adaptive passes of mesh generation were possible. However, the general trend is still clear. The magnetizing inductance is once again slightly above its former value, although the increase will be assumed to be an artifact, and the leakage inductance dropped somewhat, presumably due to shielding effects around the conductors.

5.7 Winding Geometry Conclusions

The analysis in this chapter has examined each of the three basic ways leakage manifests itself in foil transformers. Every one is dependent on the notion that fields have only one significant component in any given interwinding space, so all grow increasingly inaccurate as the interwinding space grows and this approximation fails. The finding that core gap fields are generally negligible makes analysis of all these windings surprisingly simple, however. For more complicated winding geometries, such as combinations of these basic forms, the patterns described already must be generalized somewhat further, but the analysis process is the same.

The most important aspect of these geometries to realize is that the concentrated field transformers are really just simplified versions of the distributed field type. The approximations used in these derivations reduce the problem of finding the interwinding leakage fields to a simple rule that can be applied to a cross-section of the transformer. Given a slot in the core of the cross-section of a transformer that contains conductors, draw a line from one side of the core to the other such that it crosses all of the conductors and their interwinding spaces. The fields perpendicular to the line in these interwinding spaces will only be non-zero if the line crosses conductors of both primary and secondary windings. The Adjacent geometry is shown in Figure 5.15 as an example.

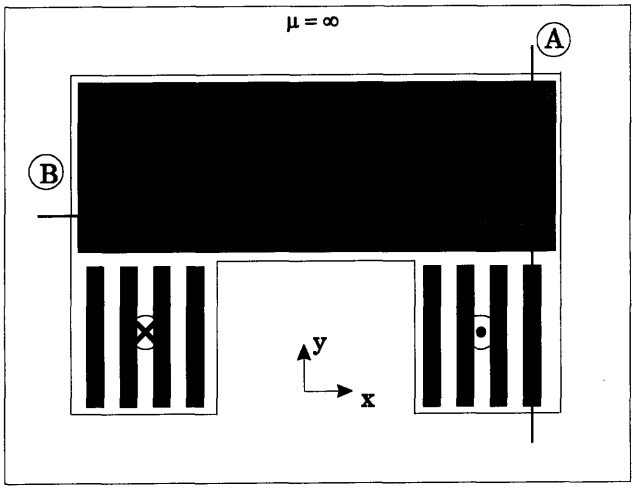

Figure 5.15: Quick Approximation of Leakage Fields

The line marked by B passes through only primary conductors before reentering the core material. The fields due to the currents in these conductors naturally cancel each other out, and the core forces the magnetic fields outside the outermost conductors to zero, thus providing the boundary conditions. Therefore, there are no vertical magnetic fields between these conductors. In A, however, the fields due to the two conductors add together in the center. Once the locations of the non-zero fields are known, contours can be found to apply Ampere's law. The observant reader will notice that for some aspect ratios, the assumptions of thin current sheets and fields that have significant components in only one direction start to break down. These nonidealities will certainly cause error in the theoretical derivations. As the simulation and prototype results show, however, the analytic derivation methods presented in this chapter are quite accurate as long as the aspect ratio of the transformer is large enough, allowing the simplifying approximations to hold.

Chapter 6

Analysis of a Commercial Charging System

In anticipation of the increased presence of electric vehicles on the market, the Society of Automotive Engineers has begun work on Electric Vehicle Inductive Coupling Recommended Practice document SAE J-1773[16], which is still in draft form at the current time. Similar specifications are the basis for at least one existing commercial system. The standard model of the MagneCharge Inductive Charger System[17], produced by Hughes Power Control Systems in conjunction with General Motors Corporation, provides up to 6.1 kilowatts at up to 92% efficiency and 99% power factor. This chapter will examine the transformer component of this charging system.

6.1. Relevant SAE Specifications

SAE document J-1773 provides specifications for the transformer characteristics in the following table[1] whose values correspond to the circuit elements found in Figure 6.1.

	Max Rp	±10% Lp	Min Rm	±10% Lm	Max Rs	±10% Ls	Min Cs
f min (100 kHz)	20mΩ	0.8μH	1.6kΩ	45 μH	20mΩ	0.8μH	0.02μF
f max (350 kHz)	40mΩ	0.5μH	1.3kΩ	55 μH	40mΩ	0.5μH	0.02μF

Table 6.1: SAE Recommended Values for Transformer Model

[1]Table and Figures 6.1 through 6.4 copied from SAE J-1773

SAE J-1773 assumes the "use of a sine wave, a resonant circuit, and a 4:4 turns ratio at 6.6 kW" for these measurements. The model ignores interwinding capacitances, presumably because they should have no effect over the frequencies of operation.

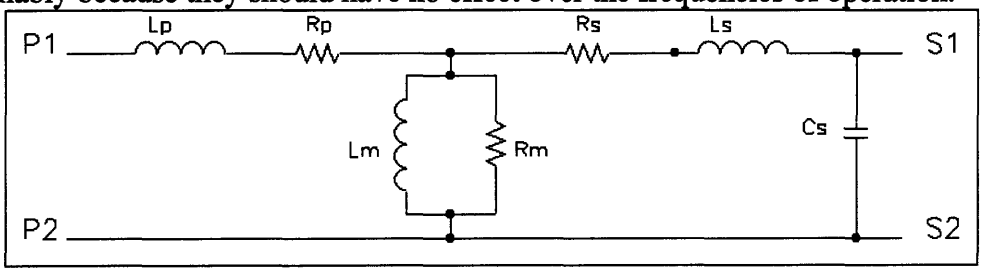

Figure 6.1: SAE Simplified Equivalent Transformer Model

The recommended practice document also provides a number of electrical and mechanical ratings that are important in the design of the transformer:

Volts per turn in the Secondary:	100 V / Turn
Maximum charging Voltage at the Vehicle Inlet:	475 Volts
Maximum charging current at the vehicle inlet:	400 Amps
Minimum charge coupling efficiency:	99.5%
Min insulation resistance (Contacts to Chassis):	100 MOhms
Maximum coupler mass (without cord):	1 kg
Min. drop height onto concrete without damage:	1 meter
Min. vehicle weight withstood when run over: (without electroshock or fire hazard)	2000 lb / wheel

Table 6.2: Recommended Electrical/Mechanical Transformer Ratings

Finally, Section 2 of SAE J-1773 states that "the intent of the Recommended Practice is to define a common electric vehicle inductive charging inlet and its mating coupler." To this end, mechanical drawings were included for a proposed common charging coupler (which houses the primary and is also called the paddle) and inlet

(containing the secondary). The coupler presented in the recommended practice document is shown in Figures 6.2 through 6.4 and a cross-section of the inlet is shown in Figure 6.5. Immediately apparent from the shape of the coupler is that design decisions were made with regard to the winding geometry in the transformer. The effects of these decisions should be apparent from the discussion in Chapter 5. The vital pieces of information to notice in the drawings of the coupler are the dimensions on the center ferrite puck and the total thickness of the coupler, since these are dimensions that were strategically modified by the Magnecharge system to improve the inductance parameters of the transformer.

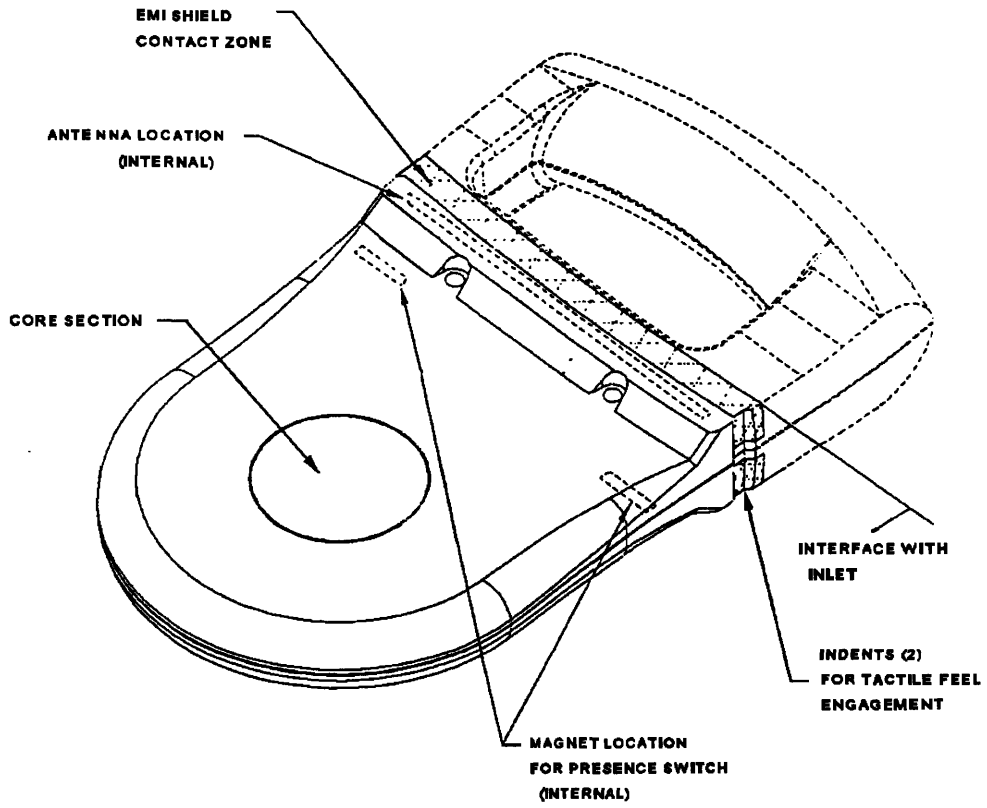

Figure 6.2: Perspective View of Coupler

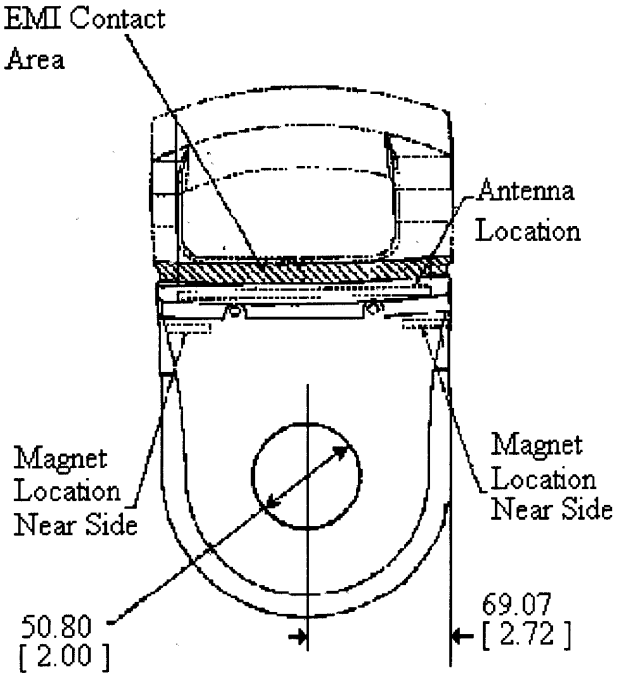

Figure 6.3: Top View of Coupler

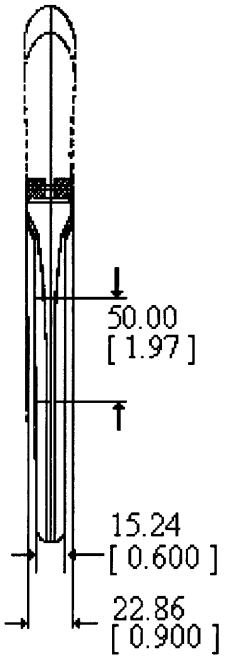

Figure 6.4: Side View of Coupler

6.2. Preliminary Analysis of the SAE Charger

Using the method described in Chapter 2, a rough calculation of the magnetizing inductance in this system can be made from just the center leg diameter and length of the total air gap in the core. The diameter is listed as 2.00 inches, and the total air gap is 0.75 millimeters plus at least 0.076 millimeters of insulation coating the puck. Plugging this into the formula,

$$L_{mag} \approx \frac{\mu_0 N^2 A}{l_{gap}} \tag{2.11}$$

a reasonable estimate of the maximum magnetizing inductance is around 49.3 mH. This is within the specifications recommended by Table 6.1.

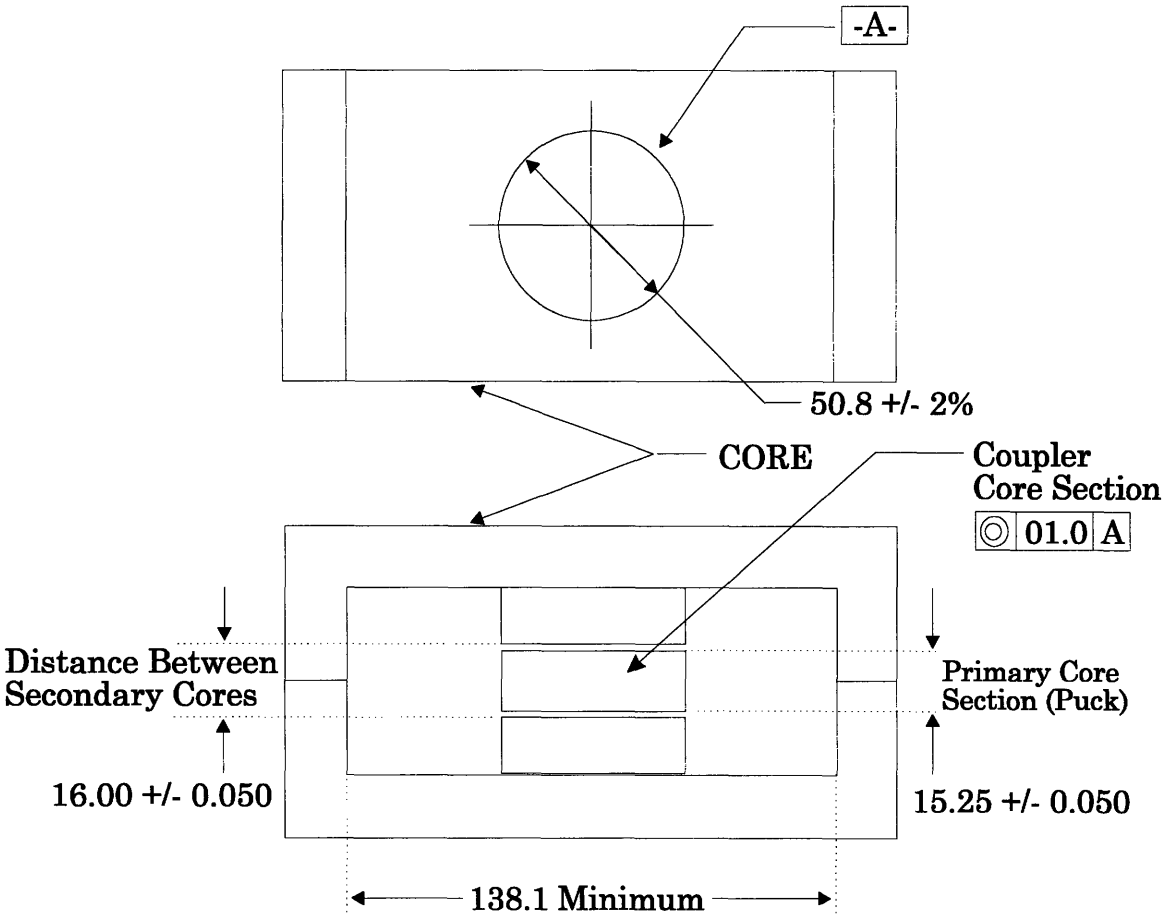

Figure 6.5: Inlet Core Dimensions from SAE J-1773

SAE J-1773 does not specify the location of the windings within either the coupler or the inlet, and the dimensions associated with the windings are critical to the calculation of leakage inductance. Minimum thicknesses for the insulation between the windings may be derived from the 100 volt per turn specification, but the actual value will probably be significantly larger than the minimum thickness required to prevent

breakdown. From the information provided, it is impossible to determine the geometries used for the primary and secondary windings, and the derivations in Chapter 5 demonstrate that this knowledge is critical for the determination of leakage inductance. What *is* obvious from Figure 6.5, however, is that the secondary is separated into two sections, one above and one below the coupler. This choice reduces the leakage inductance in the system by over a factor of two and was probably one of the main reasons for choosing the core geometry used.

A number of other issues are suggested by the shape of the coupler and the way in which it is inserted in the inlet. The first issue is mechanical robustness, where the choice of a flat paddle will not only be lighter than other designs because of the relatively little core material, but will also probably be more likely to remain intact after being accidentally run over by an automobile. Verification of this hypothesis is beyond the scope of this project, but it's hard to flatten something that is already planar to begin with. The second issue is electromagnetic radiation from the coupler when in use. Outside of the air gap around the puck, the highest concentration of magnetic energy will be the leakage fields created between the windings due to the current flowing through them. These fields are constrained between the windings where they attenuate proportionally to radius until the windings end at the outer radius where they attenuate faster. Still, of all the free space around the coupler, the highest fields will be located in the plane of the windings, which is where the person operating the coupler will hold the paddle. Measurement of the magnitude of these fields will be necessary to ensure compliance with the Electromagnetic Compatibility (EMC) requirements of GM9100P and SAE J551. Finally, when positioned so that the coupler slides into the EE core vertically, no core material is present at the bottom of the inlet and drainage of water is possible from the inlet, in accordance with Section 6.2.3.8 of SAE J-1773.

6.3. MagneCharge Dimensions and Analysis

The MagneCharge Inductive Charging System coupler is almost identical in design to the one recommended by SAE J-1773. However, a number of differences in its dimensions suggest that it has the ability to perform much better. Table 6.3 presents a comparison of relevant dimensions for the coupler of the MagneCharge system and the corresponding SAE specifications.

	SAE J-1773	MagneCharge
Puck Diameter	50.80 mm [2.00 in]	63.50 mm [2.50 in] (Lip extends to 68 mm)
Coupler Thickness	15.25 mm	8.00 mm
Coupler Width	138.1 mm	136.5 mm
Winding Width	NA	20 mm
Inner Winding Radius	NA	38.4 mm
Max Total Winding Thickness	NA	~ 3.5 mm

Table 6.3: Dimension Comparison: SAE Specs vs. MagneCharge

The most striking differences is that the area of the puck has been increased by 56% and the thickness of the coupler has been reduced by half. The effect of the first change is to increase the magnetizing inductance of the system, more or less proportionally to the increase in area. Again using equation 2-11 to provide a rough estimate, the DC magnetizing inductance in the MagneCharge system (assuming the SAE recommended gap between coupler and inlet) increases to between 80 and 90 μH, depending on the exact gap length and puck diameter used.

The decrease in thickness of the coupler corresponds to a significant decrease in the leakage inductance of the system. In order to find a good estimate for the actual value, however, the placement and dimensions of the windings must be taken into account as well. [2] identifies the winding geometry used as helical, which is the most reasonable option considering the aspect ratio of the coupler. Examination of the paddle suggests that the four primary turns fit within 3.5 mm, making the interwinding gap between each conductor around 0.887 mm, based on the conductor thickness value derived below. However, the distance between the primary and secondary winding packs depends on the dimensions of the MagneCharge secondary, which was not available for inspection. If the secondary were to have the same spacing as the primary, the winding pack separation would be around 4.5 mm, leading to a leakage inductance value of 0.38 μH. This value is only speculation, however.

In order to determine the winding resistance, impedance measurements were taken over a range of frequencies, as was done on the laboratory prototype transformers. These measurements provide information that is useful for determining both the DC and AC resistance. Making use of the derivation of the DC resistance in a helical winding, the available dimensions of the coupler windings, and the DC resistance measurements from Appendix F, an estimate for the conductor thickness can be derived. It is assumed that the helical structure has only one turn per layer, and the resulting thickness of the copper in the coupler windings is 0.21 mm, or just over 8 mils. Correspondingly, 1.16 milliohms would be present in the conductors in the paddle leading up to the helical windings, and 4.83 milliohms would be present in the windings themselves. These results were derived by the following process:

$$R_{Total} = R_{Windings} + R_{Diagonal} + R_{LeadStrip} = 5.99\,m\Omega$$

$$R_{Total} = \frac{8\pi\rho}{\ln(\frac{r_2}{r_1})t} + \frac{0.023\rho}{0.022t} + \frac{0.1\rho}{0.016t} = 5.99\,m\Omega$$

For $\rho_{copper} = 1.673 \times 10^{-8}\ \Omega - m$, the copper thickness, t, is 0.21 mm.

For a nominal operating frequency of 100 kHz, this makes the winding thickness equal to the skin depth, allowing Goldberg's conclusions to apply and making the AC resistance at 100 kHz approximately seven times higher than the DC value.

6.4 Finite Element Analysis

For a numerical estimate of the inductance of the charger, the Maxwell software package was used again to simulate the complete system. Again, the exact field profiles within the windings were of interest in this case, but the core in this system was large enough to separate the individual conductors and still achieve reasonable results.

Figure 6.6 shows a top view of the simulation geometry which only models half of the physical system because of the symmetry between the two halves of the core. Figures 6.7 and 6.8 show isometric and cross-sectional views of the same model.

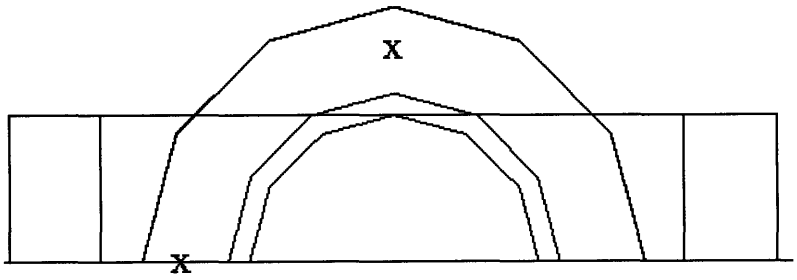

Figure 6.6: Top View of Split Secondary Transformer

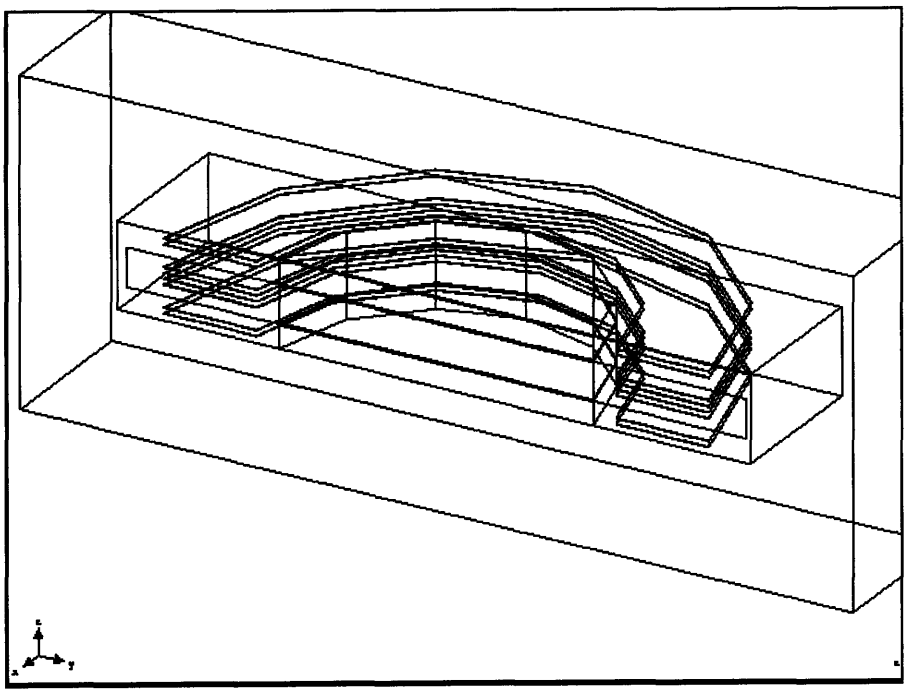

Figure 6.7: Isometric View of Split Secondary Transformer

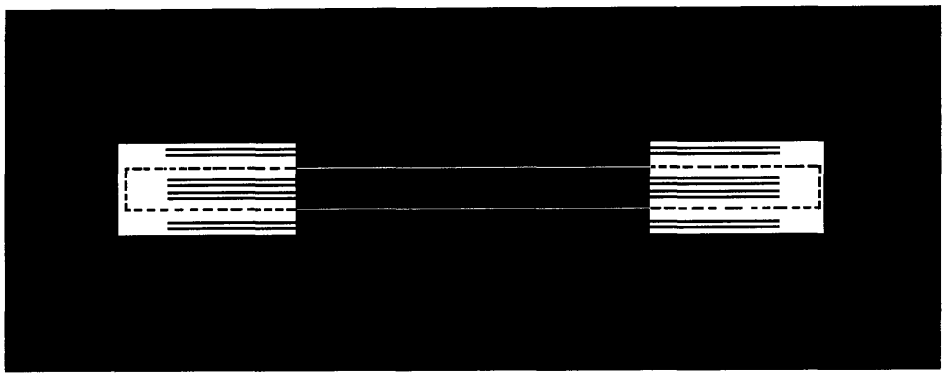

Figure 6.8: Cross-Sectional View of Split Secondary Transformer

In the cross-sectional view of the system, the shaded areas correspond to core sections, the bulk of which resides in the car and thin puck being in the center of the paddle. The dotted line in the figure denotes the boundary of the paddle, showing that there are two secondary windings on either side of the paddle which contains four stacked windings. The dimensions used in the simulations are as follows:

Winding Geometry:	Helical, Split Secondary
Puck Dimensions:	7.6 mm thick 68 mm diameter (includes lip)
Winding Dimensions:	0.1 mm thick 1.1 mm interwinding thickness 20 mm wide 38.5 mm inner radius 58.5 mm outer radius
Core Dimensions:	138 mm Inner Width 0.4 mm gaps

Table 6.4: Maxwell Charger Simulation Dimensions

Simulations were first performed at DC. These resulted in circuit inductances of

$$L_{mag} = 84.9\ \mu H \qquad and \qquad L_{leak} = 0.344\ \mu H.$$

As predicted in Section 6.3, the magnetizing inductance is between 80 and 90 μH, and comparing the theoretical leakage value of 0.38 μH obtained with the derivations in Chapter 5 with the simulated result above, the values are seen to be close although the simulated value is lower. This was expected, since the analytical value derived was an upper bound. To verify that the correspondence was due to more than simulation artifacts, values of the interwinding fields in the simulation were examined.

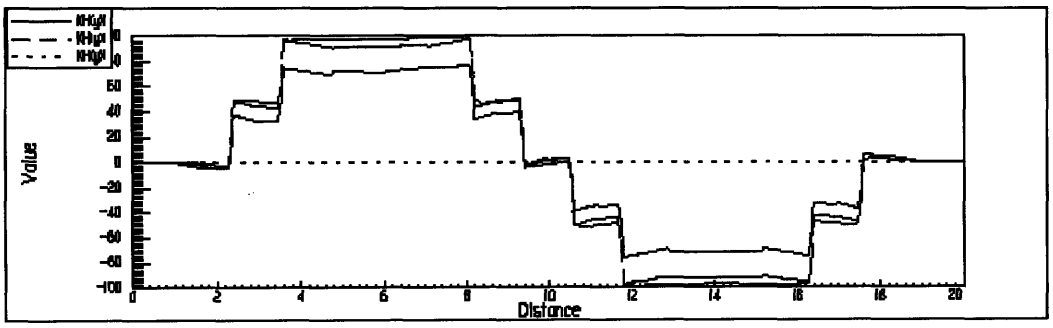

Figure 6.9: Radial Interwinding Leakage Field - Enclosed by Core

Two examples of the field results are displayed in Figures 6.9 and 6.10, where the horizontal axis spans a vertical cut through all eight windings of the transformer.

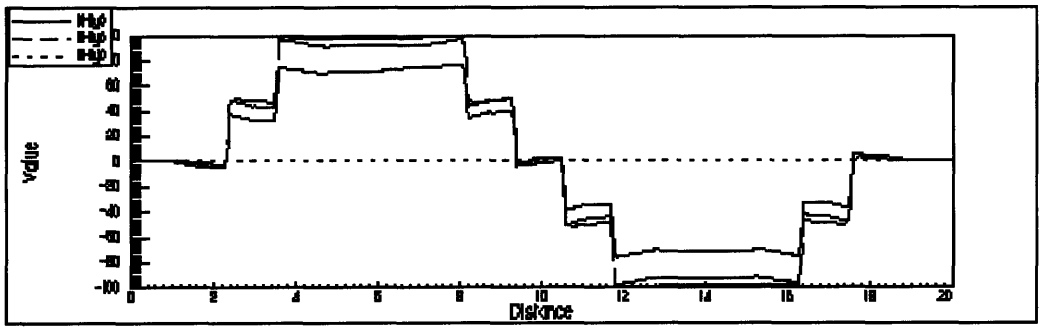

Figure 6.10: Radial Interwinding Leakage Field - Outside Core

Figure 6.9 shows the radial component of the magnetic field along a vertical contour within the core material and Figure 6.10 shows the radial component of the field where the winding is parallel to the long axis of the core (ie: where the windings are completely outside the core). These two points are denoted by x's in Figure 6.6. The three traces in each plot correspond to placing the vertical contour at three different radii, 45 mm, 50 mm, and 55 mm (5, 10, and 15 mm into the 20 mm wide windings). A bow-shaped reduction in the field values can be seen towards the center of the largest interwinding gap, located between the primary and secondary windings. In addition, the slight slope to the horizontal sections corresponding to the other interwinding spaces probably corresponds to fact that very close to a winding, the influence of the other windings is reduced since the fields still attenuate somewhat, even over short distances. The close agreement between the plot where the windings are free of the core and the one where they are enclosed supports the assumptions that allowed the field derivations to be extended beyond just the areas surrounded by the core. In addition, the separation between the three curves shows the inverse radial dependence predicted in Section

5.2.1.2. The magnetic field strengths in these plots are compared in Table 6.5 to those predicted by the derivation of the corresponding leakage fields. The larger calculated field values explain the difference between the calculated and simulated leakage inductance. Also, all field values in the table are in Amperes per meter.

Next, simulations were performed that included the effects of eddy currents at higher frequencies. Although the true resistivity of the core is unknown, 1.0 Ohm-meters was used in the simulation as with the prototypes. Note that this makes the skin depth at 80 kHz equal to 5 cm, placing the center of the puck at a radial distance of one half of a skin depth from the surface. Compared to the DC leakage inductance, the value at 80 kHz remained almost the same at 0.338 μH. The high frequency magnetizing inductance again increased insignificantly from the DC value of 84.9 μH to 85.1 μH at 80 kHz. The negligible difference in magnetizing values agrees with the prediction that there is essentially no magnetic shielding even at 80 kHz. The negligible difference in leakage inductance is more interesting. By 80 kHz, the fields cannot penetrate the conductors, so the lack of inductance change suggests that most of the field lines flow around the conductors rather than penetrating them even at DC. The field values in Table 6.5 support the leakage inductance results, in general showing the slight decrease between corresponding field amplitude measurements between the DC and 80 kHz simulations. The slight difference may be due to some shielding in the conductors, although mesh differences in the simulation are equally plausible considering the size of the reduction.

	Hw1					Hw2				
	Theoretical	DC Simulation		AC Simulation		Theoretical	DC Simulation		AC Simulation	
r	Calculation	Open	Enclosed	Open	Enclosed	Calculation	Open	Enclosed	Open	Enclosed
45 mm	53	52	50	46	47	53	52	50	46	47
50 mm	48	48	45	39	37	48	48	45	39	37
55 mm	43	35	34	33	33	43	35	34	33	33

Table 6.5: Comparison of Analytic vs. Simulated Leakage Fields

So far, the eddy current simulations have failed to demonstrate any significant differences in the high frequency inductances from their DC values. To verify that such differences *do* actually occur, eddy current simulations were repeated with the core resistivity decreased by a factor of 100, to a value of 0.01 Ohm-meters. With this resistivity, the leakage inductance remained the same at 0.343 μH, which makes sense since very little flux exists in the core in this simulation. However, the magnetizing inductance was reduced to 77.8 μH. Examination of the fields in the core for the open-circuit secondary case showed significant shielding in the core with the lower resistivity.

6.5 MagneCharge System Conclusions

It has been shown that in a number of areas, the MagneCharge system has improved on the recommended transformer element values from SAE J-1773. Because of these changes in the transformer parameters, it can be expected that the external capacitor on the secondary has been modified in the MagneCharge system as well to maintain the same resonant behavior. Unfortunately, without more information about the core material and a full harmonic analysis, the upper limit to the theoretical power transfer capability of the system cannot be evaluated. Core losses due to hysteresis and eddy currents would have to be measured empirically on an operational system as well, since they depend on the peak flux density and the exact core material. One interesting feature of the paddle which is relevant to the discussion of losses is the issue of EMI protection for a person using the coupler. The portion of the paddle casing that is toward a person's hand is made of a denser material than the rest. This suggests that this portion of the casing might have conductive material embedded in it to attenuate any fields in the direction of the user. This will increase losses slightly but lower the fields experienced by anyone using the charging system.

Chapter 7

Conclusion

Over the course of this exploration of separable core transformers, most of the basic issues required for the design of an acceptable transformer have been discussed. Although a complete design procedure is beyond the scope of this paper, the hazards that are inherent in the separable core design should be clear by now as well as strategies to avoid such pitfalls. Much of what has been presented here has been known in qualitative form to the scientific community for some time. Hopefully, the numerous derivations of the various transformer element values will provide designers with a better understanding of the basis for their intuition, as well as show when such intuition will fail.

Perhaps, it is not surprising that the most difficult steps in the exploration of this topic were the times when intuition proved incorrect. Because of the circular geometry of the core center leg, the flux density does not attenuate exponentially toward the interior. Because of fringing, the flux density levels in the center versus side legs of an E core are very different, even with identical cross-sectional areas. Because of the thinness of the conductors in the systems in this study, the winding resistance was not appreciably different at the operating frequencies despite the well-known skin effect.

Some results remain unexplained, leaving the door open to the possibility that there are significant effects left unmodeled in the derivations provided. For example, the leakage inductance did not change appreciably in the eddy current simulations, despite the intuition that the fields should pass through the conductors at DC but be forced around the conductors at high frequencies. In the absence of any other explanation, this would be even more disturbing since the foil windings were chosen precisely to try to maximize this unseen effect. However, the results suggest that the fields are being forced around the windings even at DC. One possible reason for this is the aspect ratios of the

cores involved. Since the slots between the legs of the E cores used are relatively deep, any fields that fringe across them between the two legs will be essentially parallel to the conductors, following the shortest path to the core material on the other side. In the Helical case, these fields will be parallel to the conductors, producing very little difference between low and high frequency behavior. Both cases where the high frequency leakage was successfully approximated were Helical. The result might be different for non-Helical geometries.

Finally, large areas still remain for exploration in the same vein as this study. Transformer elements such as the core losses and parasitic capacitances were largely ignored here because they were insignificant near the switching frequency. However, the industry trend is toward higher switching frequencies which will increase their importance for this type of application in the near future, and in certain situations, core losses and parasitic capacitances may be significant even now.

As a form of summary for the many derivations provided here, Appendix G provides a MATLAB script that determines the DC and high frequency transformer element values corresponding to the main elements of the equivalent circuit model. The winding geometry is assumed to be Helical and the transformer is assumed to be gapped. It does not take into account secondary details such as fringing or non-uniform flux density due to geometry effects but should be enough of a design tool for preliminary analysis. Although many of the high frequency dependencies provided by the program are non-intuitive, the basic relationships behind the DC values are simply stated and are easily recognized with an understanding of the fields in a transformer system.

The magnetizing inductance is mostly based on the energy contained in the air gap fields between the two halves of the separable core. Because of this, the inductance value is proportional to the area, as demonstrated by the increased area of the MagneCharge core over the SAE suggested specification. In contrast, increasing the footprint of the core has variable results on leakage inductance, depending on the winding

geometry. For a Helical winding, increasing the area allows the windings to become wider but also increases the volume containing leakage fields. For small cores, the net effect will reduce the leakage inductance, but the strategy has diminishing returns with increasing core size. A more straightforward leakage inductance dependency is on the thickness of the winding packs. By reducing the interwinding spaces and the gaps between the primary and secondary, the leakage field volume is decreased with no opposing trend, thereby decreasing the leakage inductance significantly. Again, every strategy has a drawback, however, and the limitation to decreasing thickness is the need to insulate the windings and, in many cases, to minimize parasitic capacitances.

For many systems, it is not the transformer that limits the power transfer, but the external power electronics which must drive the system, either because the source voltage or current is limited, or because the switching losses become significant. However, much of this paper has assumed linear behavior in the systems of interest, and this assumption can fail as well. All core materials have limitations in terms of peak flux density, excitation frequency, and temperature that prevent arbitrarily high power transfer. At levels above these limitations, the permability and the resistivity of the core can fall sharply. When this happens, the parameters in the equivalent transformer model change dramatically and the effectiveness of the power transfer can be severely reduced. For example, if the core permeability drops, the leakage fluxes in the system will grow tremendously, causing high reactive currents and a large voltage droop between the input and the output. If the resistivity plummets, large eddy currents will increase the core losses, and magnetic shielding will occur in the core, reducing the magnetizing inductance and preventing power transfer to the load. In addition, whenever large reactive currents or large eddy currents are present, the possibility of damage to the core through overheating exists as well. In all systems, therefore, it is extremely important to verify that the core parameters at the operating point of the system have not strayed too far from their nominal values.

In the end, the largest mistake a transformer designer can make is to oversimplify the system. Modern transformers are complex systems composed of non-linear materials connected to non-linear circuitry. In order to develop a suitable design, assumptions must often be made that may or may not hold true for the system in question. With a good understanding of the principles behind the elements in an equivalent transformer model, the designer has a better chance of making the right assumptions to simplify the design process. In the end, however, all aspects must be considered to determine whether the simplified model remains accurate. To ignore the realities of nature in systems as complex as a modern transformer would be shortsighted at best and unethical at worst.

Appendices

Appendix A: Magnetic Diffusion in a High Resistivity Core

This derivation is based on the discussion in Chapter 3 of Electromagnetic Waves, by Staelin, Morgenthaler, and Kong [18]. It then uses the formula for the magnetic penetration depth given in [2] to derive the full, complex wave number which is necessary for a complete formulation of the magnetic fields in the core as a function of time. As described in Chapter 3 of this paper, the skin depth can then be used to determine the magnetic flux density profile and the effect of the magnetic shielding on the magnetizing inductance. Starting from the dispersion relation for a uniform wave propagating in a lossy medium, given by

$$k^2 = \omega^2 \mu\varepsilon(1 - \frac{j\sigma}{\omega\varepsilon}) \tag{A-1}$$

let k = k' - jk", where both k' and k" are real numbers. Substituting this into A-1, the equations

$$(k')^2 - (k")^2 = \omega^2 \mu\varepsilon \tag{A-2}$$

and

$$2k'k" = \omega\mu\sigma \tag{A-3}$$

are produced by matching the real and imaginary parts.

[2] provides an formula for the penetration depth, which is the inverse of k". This equation can be reorganized to yield

$$k" = \frac{\sqrt{\sqrt{(\omega\varepsilon\rho)^2 + 1} - \omega\varepsilon\rho}}{\sqrt{2\rho/\omega\mu}}. \tag{A-4}$$

At this point, there is no guarantee that this formula is exact rather than an approximation. The way to find out is to plug it into (A-3), determine the value of k', and then plug both into (A-2) to see if it is satisfied. Using this method, k' is given by

$$k' = \frac{\sqrt{\sqrt{(\omega\varepsilon\rho)^2 + 1} + \omega\varepsilon\rho}}{\sqrt{2\rho/\omega\mu}} \qquad \text{(A-5)}$$

and (A-1) is indeed satisfied.

The difference between this formula and the standard skin depth formula is the result of the high resistivity in the core. The displacement current source term in Ampere's law can usually be ignored when analyzing the magnetic fields in conductors because the time-changing voltage associated with any induced eddy currents isn't large enough to significantly affect the resulting magnetic field. The omission of the displacement current greatly simplifies the determination of the magnetic penetration distance and results in the standard skin depth formula. (A-4) provides the true skin depth for the high resistivity ferrite cores, which is actually larger than the simpler formulation predicts.

Having calculated the skin depth in the core, the flux profile in the core must be determined in order to find the high frequency magnetizing inductance. The wave number formulation assumed a propagating wave of the form

$$\overline{B} = B_0 e^{-jkx}\hat{z} \qquad \text{(A-6)}$$

with the complex wave number, k, described above. In the absence of any special boundary conditions, the magnetic field would be free to attenuate exponentially towards the interior of the material. Splitting (A-6) to reflect the real and complex components of the wave number, this creates a magnetic field distribution that looks like

$$\mathrm{Re}\{B(x)\} = \mathrm{Re}\{B_0 e^{-k''x - jk'x}\} = B_0 e^{-x/\delta}\cos(k'x). \qquad \text{(A-7)}$$

However, the circular center leg imposes additional boundary conditions. The radial symmetry changes the magnetic field description to

$$\overline{B} = B_0 e^{-jkr}\hat{z}. \tag{A-8}$$

In addition, the induced eddy currents must vanish at the center of the leg, forcing

$$\frac{\partial B(r=0)}{\partial r} = 0. \tag{A-9}$$

With two boundary conditions, the field solution can be found with two exponential components instead of just one.

$$B := B_0 \cdot \frac{\cosh\left[(1+j)\cdot\frac{r}{\delta}\right]}{\cosh\left[(1+j)\cdot\frac{r_0}{\delta}\right]} \tag{A-10}$$

At a radius of zero, the sinh function corresponding to the derivative of the magnetic flux will vanish, and at the core radius, the magnetic flux density will become B_0. Note that even though this magnetic flux density has radial dependence, the hyperbolic characteristic makes it still essentially a rectangular solution to the magnetic diffusion equation rather than a cylindrical solution. As in the solution from Chapter 3, this will introduce an error because the curvature is not being taken into account completely. However, for the purpose of finding a close approximation, the rectangular solution is once again close enough to work with. As before, the first step in the formulation of the flux profile is to extract off the real portion of this expression. This is given by

$$Re(B) := B_0 \cdot \frac{\cos\left(\frac{r}{\delta}\right)\cdot\cosh\left(\frac{r}{\delta}\right)\cdot\cos\left(\frac{r_0}{\delta}\right)\cdot\cosh\left(\frac{r_0}{\delta}\right) + \sin\left(\frac{r}{\delta}\right)\cdot\sinh\left(\frac{r}{\delta}\right)\cdot\sin\left(\frac{r_0}{\delta}\right)\cdot\sinh\left(\frac{r_0}{\delta}\right)}{\cos\left(\frac{r_0}{\delta}\right)^2\cdot\cosh\left(\frac{r_0}{\delta}\right)^2 + \sin\left(\frac{r_0}{\delta}\right)^2\cdot\sinh\left(\frac{r_0}{\delta}\right)^2} \tag{A-11}$$

This is the expression that is plotted in Chapter 3 and represents the magnetic flux profile in the core at a specific instant of time. This formula can be split into two parts to simplify the rest of the calculations. Such a simplification yields

$$\mathrm{Re}(B) := B_0 \cdot K_c \cdot \cos\left(\frac{r}{\delta}\right) \cdot \cosh\left(\frac{r}{\delta}\right) + B_0 \cdot K_s \cdot \sin\left(\frac{r}{\delta}\right) \cdot \sinh\left(\frac{r}{\delta}\right) \tag{A-12}$$

where

$$K_c := \frac{\cos\left(\frac{r_0}{\delta}\right) \cdot \cosh\left(\frac{r_0}{\delta}\right)}{\cos\left(\frac{r_0}{\delta}\right)^2 \cdot \cosh\left(\frac{r_0}{\delta}\right)^2 + \sin\left(\frac{r_0}{\delta}\right)^2 \cdot \sinh\left(\frac{r_0}{\delta}\right)^2} \tag{A-13}$$

and

$$K_s := \frac{\sin\left(\frac{r_0}{\delta}\right) \cdot \sinh\left(\frac{r_0}{\delta}\right)}{\cos\left(\frac{r_0}{\delta}\right)^2 \cdot \cosh\left(\frac{r_0}{\delta}\right)^2 + \sin\left(\frac{r_0}{\delta}\right)^2 \cdot \sinh\left(\frac{r_0}{\delta}\right)^2}. \tag{A-14}$$

With this formulation, the next step is to integrate over the cross-sectional area of the magnetic core leg.

$$\Phi_{core} = 2\pi \int_0^{r_0} B(r) r \, dr \tag{A-15}$$

Evaluating this integral produces

$$\begin{aligned} \Phi_{AC\_core} = {} & B_0 K_c \pi \delta^2 \left[\tfrac{r_0}{\delta} \left(\cos(\tfrac{r_0}{\delta}) \sinh(\tfrac{r_0}{\delta}) + \sin(\tfrac{r_0}{\delta}) \cosh(\tfrac{r_0}{\delta}) \right) - \sin(\tfrac{r_0}{\delta}) \sinh(\tfrac{r_0}{\delta}) \right] \\ & + B_0 K_s \pi \delta^2 \left[\tfrac{r_0}{\delta} \left(\sin(\tfrac{r_0}{\delta}) \cosh(\tfrac{r_0}{\delta}) - \cos(\tfrac{r_0}{\delta}) \sinh(\tfrac{r_0}{\delta}) \right) + \cos(\tfrac{r_0}{\delta}) \cosh(\tfrac{r_0}{\delta}) - 1 \right] \end{aligned} \tag{A-16}$$

which must be compared to the flux formulation at DC in order to determine the relationship between the AC and DC magnetizing inductances. Ignoring geometric causes of non-uniform flux, the DC flux value is given by

$$\Phi_{DC\_core} = B_0 \pi r_0^2. \tag{A-17}$$

Thus, the ratio between the two levels of flux is given by

$$\begin{aligned} K_{AC} = K_c \frac{\delta^2}{r_0^2}\left[\frac{r_0}{\delta}\left(\cos(\tfrac{r_0}{\delta})\sinh(\tfrac{r_0}{\delta}) + \sin(\tfrac{r_0}{\delta})\cosh(\tfrac{r_0}{\delta})\right) - \sin(\tfrac{r_0}{\delta})\sinh(\tfrac{r_0}{\delta})\right] \\ + K_s \frac{\delta^2}{r_0^2}\left[\frac{r_0}{\delta}\left(\sin(\tfrac{r_0}{\delta})\cosh(\tfrac{r_0}{\delta}) - \cos(\tfrac{r_0}{\delta})\sinh(\tfrac{r_0}{\delta})\right) + \cos(\tfrac{r_0}{\delta})\cosh(\tfrac{r_0}{\delta}) - 1\right]. \end{aligned} \tag{A-18}$$

Because the magnetizing inductance can be expressed by

$$L_{mag} = \frac{N\Phi}{i}$$

and K_{AC} gives the ratio between the AC and DC flux levels in the core, the high frequency value of the magnetizing inductance can be found from

$$L_{mag\_AC} = K_{AC} \cdot L_{mag\_DC}.$$

Notice also that the conversion factor can be fully determined from the skin depth and the radius of the core leg. K_{AC} is plotted in Chapter 3 as a function of the ratio between the skin depth and the core radius, showing a fairly sharp threshold in the attenuation characteristic.

Appendix B: Theoretical DC Prototype Magnetizing Inductance

The prototype transformers, because of the placement of the air gaps in the core, have a different magnetizing inductance derivation from the MagneCharge transformer. In the MagneCharge system, both air gaps are located in the center leg of the core. In the prototype core, however, the second air gap is split into two gaps, one in each side leg. Reluctances can be calculated for each of the gaps as presented before, and then combined into one equivalent reluctance treating the magnetic circuit like an electrical one. The center leg has an area of $7.069 \times 10^{-4} m^2$ which results in a reluctance of 1.126×10^6. Each side leg has an area of $3.131 \times 10^{-4} m^2$, corresponding to a reluctance of 2.542×10^6. Since the flux must pass through the two side leg reluctances in parallel, they form an equivalent reluctance of half their individual values, creating a total equivalent series reluctance of 2.397×10^6. If the two air gaps had equivalent cross-sectional areas, the total reluctance would have been exactly twice the value of either one, as in the series circuit. There are four turns, so the flux linkage resulting from one amp flowing through the primary winding is 6.675×10^{-6}. Thus, the magnetizing inductance of the transformer is **6.68 μH**.

Note that if the strongest fringing effect, around the air gaps, is taken into account, a much closer approximation of the magnetizing inductance can be obtained. As suggested by [10], adding one gap width to each dimension of the cross-sections results in a center leg effective area of: $8.042 \times 10^{-4} m^2$ and a reluctance of 9.895×10^5, and for the side legs, an effective area of around $3.84 \times 10^{-4} m^2$ and a reluctance of 2.072×10^6. Thus, the total equivalent reluctance is 2.026×10^6 and the new approximation for the magnetizing inductance is **7.90 μH**.

Appendix C: Flux Tube Simulation - Helical Prototype

3-Dimensional Flux Tube Model for Pancake Transformer

Complexity Level: 3

Dimensions

Lengths (1/4 modelling area)

gap := .001 fringe := gap center_len := .035 rad_center := .015

leg_width := .01 leg_depth := .015 leg_len := .035

top_len := .02 top_depth := .015 top_height := .01

Cross-Sectional Areas (1/4 modelling area)

$A_{center} := \frac{\pi \cdot rad\_center^2}{4}$ $A_{center\_gap} := \frac{\pi \cdot (rad\_center + fringe)^2}{4}$

$A_{leg} := leg\_depth \cdot leg\_width$

$A_{top} := top\_depth \cdot top\_height$

Values

$A_{center} = 1.767 \cdot 10^{-4}$

$A_{center\_gap} = 2.010 \cdot 10^{-4}$

$A_{leg} = 1.5 \cdot 10^{-4}$

$A_{top} = 1.5 \cdot 10^{-4}$

Material and Driving Properties

$mu_0 := 4 \cdot \pi \cdot 10^{-7}$ $mu_{core} := 2500$ $mu_{air} := 1$

Windings := 4 Amps := 1

Reluctance Definition

$$Reluct(Area, Length, mu_{relative}) := \frac{Length}{Area \cdot mu_{relative} \cdot mu_0}$$

Model Reluctances

Core Regions

$R_{center} := Reluct\left(A_{center}, \frac{leg\_len}{3}, mu_{core}\right)$ $R_{corner\_center} := 17797.1$

$R_{topbar} := Reluct\left(A_{top}, \frac{top\_len}{3}, mu_{core}\right)$ $R_{corner\_leg} := 13839.6$

$R_{leg1} := Reluct\left(A_{leg}, \frac{leg\_len}{3}, mu_{core}\right)$ $R_{leg2} := Reluct\left(A_{leg}, \frac{leg\_len}{3} - .005, mu_{core}\right)$

$R_{leg3} := Reluct(A_{leg}, 0.0005, mu_{core})$ $R_{leg4} := Reluct(A_{leg}, 0.001, mu_{core})$

Gaps

$R_{gap\_center} := Reluct(A_{center\_gap}, gap, mu_{air})$

$R_{gap\_leg} := Reluct(A_{leg}, gap, mu_{air})$

$R_{gap\_return} := Reluct(gap \cdot leg\_depth, top\_len, mu_{air})$

Fringing Regions

Side Leg Fringing Reluctances (inside square and outside curved)

$A_{side1} := 0.001 \cdot leg\_depth$

$A_{corner1} := 0.001^2$

$A_{side2} := \left(\frac{leg\_len}{3}\right) \cdot leg\_depth$

$A_{corner2} := \left(\frac{leg\_len}{3}\right)^2$

$A_{back1} := 0.001 \cdot leg\_width$

$A_{back2} := \frac{leg\_len}{3} \cdot leg\_width$

$A_{fr1\_side} := A_{side1} + \frac{1}{2} \cdot A_{corner1}$ $R_{fr1\_side} := Reluct(A_{fr1\_side}, 0.002 + gap, mu_{air})$

$A_{fr2\_side} := A_{side1} + \frac{3}{2} \cdot A_{corner1}$ $R_{fr2\_side} := Reluct(A_{fr2\_side}, 0.006 + gap, mu_{air})$

$A_{fr3\_side} := A_{side1} + \frac{5}{2} \cdot A_{corner1}$ $R_{fr3\_side} := Reluct(A_{fr3\_side}, 0.010 + gap, mu_{air})$

$A_{fr4\_side} := A_{side1} + \frac{7}{2} \cdot A_{corner1}$ $R_{fr4\_side} := Reluct(A_{fr4\_side}, 0.014 + gap, mu_{air})$

$A_{fr5\_side} := A_{side1} + \frac{9}{2} \cdot A_{corner1}$ $R_{fr5\_side} := Reluct(A_{fr5\_side}, 0.018 + gap, mu_{air})$

$A_{fr6\_side} := A_{side2} + \frac{1}{2} \cdot A_{corner2}$ $R_{fr6\_side} := Reluct\left[A_{fr6\_side}, \left(\frac{leg\_len}{3} + \frac{gap}{2}\right) \cdot \pi, mu_{air}\right]$

$A_{fr7\_side} := A_{side2} + \frac{3}{2} \cdot A_{corner2}$ $R_{fr7\_side} := Reluct\left[A_{fr7\_side}, \left(\frac{2 \cdot leg\_len}{3} + \frac{gap}{2}\right) \cdot \pi, mu_{air}\right]$

$A_{fr8\_side} := A_{side2} + \frac{5}{2} \cdot A_{corner2}$ $R_{fr8\_side} := Reluct\left[A_{fr8\_side}, \left(\frac{3 \cdot leg\_len}{3} + \frac{gap}{2}\right) \cdot \pi, mu_{air}\right]$

$A_{fr1\_back} := A_{back1} + \frac{1}{2} \cdot A_{corner1}$ $R_{fr1\_back} := Reluct(A_{fr1\_back}, 0.002 + gap, mu_{air})$

$A_{fr2\_back} := A_{back1} + \frac{3}{2} \cdot A_{corner1}$ $R_{fr2\_back} := Reluct(A_{fr2\_back}, 0.006 + gap, mu_{air})$

$A_{fr3\_back} := A_{back1} + \frac{5}{2} \cdot A_{corner1}$ $R_{fr3\_back} := Reluct(A_{fr3\_back}, 0.010 + gap, mu_{air})$

$$A_{fr4\_back} := A_{back1} + \frac{7}{2}\cdot A_{corner1} \qquad R_{fr4\_back} := Reluct\left(A_{fr4\_back}, 0.014 + gap, mu_{air}\right)$$

$$A_{fr5\_back} := A_{back1} + \frac{9}{2}\cdot A_{corner1} \qquad R_{fr5\_back} := Reluct\left(A_{fr5\_back}, 0.018 + gap, mu_{air}\right)$$

$$A_{fr6\_back} := A_{back2} + \frac{1}{2}\cdot A_{corner2} \qquad R_{fr6\_back} := Reluct\left[A_{fr6\_back}, \left(\frac{leg\_len}{3} + \frac{gap}{2}\right)\cdot\pi, mu_{air}\right]$$

$$A_{fr7\_back} := A_{back2} + \frac{3}{2}\cdot A_{corner2} \qquad R_{fr7\_back} := Reluct\left[A_{fr7\_back}, \left(\frac{2\cdot leg\_len}{3} + \frac{gap}{2}\right)\cdot\pi, mu_{air}\right]$$

$$A_{fr8\_back} := A_{back2} + \frac{5}{2}\cdot A_{corner2} \qquad R_{fr8\_back} := Reluct\left[A_{fr8\_back}, \left(\frac{3\cdot leg\_len}{3} + \frac{gap}{2}\right)\cdot\pi, mu_{air}\right]$$

Combining Side and Back Fringing Regions for the Side Leg:

$$Parallel(A, B) := \left(A^{-1} + B^{-1}\right)^{-1}$$

$$R_{side\_fr1} := Parallel\left(R_{fr1\_side}, R_{fr1\_back}\right) \qquad R_{side\_fr2} := Parallel\left(R_{fr2\_side}, R_{fr2\_back}\right)$$

$$R_{side\_fr3} := Parallel\left(R_{fr3\_side}, R_{fr3\_back}\right) \qquad R_{side\_fr4} := Parallel\left(R_{fr4\_side}, R_{fr4\_back}\right)$$

$$R_{side\_fr5} := Parallel\left(R_{fr5\_side}, R_{fr5\_back}\right) \qquad R_{side\_fr6} := Parallel\left(R_{fr6\_side}, R_{fr6\_back}\right)$$

$$R_{side\_fr7} := Parallel\left(R_{fr7\_side}, R_{fr7\_back}\right) \qquad R_{side\_fr8} := Parallel\left(R_{fr8\_side}, R_{fr8\_back}\right)$$

Center Leg Fringing Regions (circular length assumption)

$$A_{center\_fr1} := \left(\frac{center\_len}{3}\cdot rad\_center\right)$$

$$R_{cntr\_fr1} := Reluct\left[A_{center\_fr1}, \left(\frac{center\_len}{3} + \frac{gap}{2}\right)\cdot\pi, mu_{air}\right] \qquad R_{cntr\_fr1} = 1.7381\cdot 10^{8}$$

$$R_{cntr\_fr2} := Reluct\left[A_{center\_fr1}, \left(\frac{2\cdot center\_len}{3} + \frac{gap}{2}\right)\cdot\pi, mu_{air}\right] \qquad R_{cntr\_fr2} = 3.4048\cdot 10^{8}$$

$$R_{cntr\_fr3} := Reluct\left[A_{center\_fr1}, \left(\frac{3\cdot center\_len}{3} + \frac{gap}{2}\right)\cdot\pi, mu_{air}\right] \qquad R_{cntr\_fr3} = 5.0714\cdot 10^{8}$$

Horizontal Leakage Flux between Side and Center Legs

$$R_{hz1} := Reluct\left(0.02\cdot leg\_depth, top\_len, mu_{air}\right) \qquad R_{hz1} = 5.3052\cdot 10^{7}$$

$$R_{hz2} := Reluct\left(.012\cdot leg\_depth, top\_len, mu_{air}\right) \qquad R_{hz2} = 8.8419\cdot 10^{7}$$

Top Bar to Bottom Bar Fringing Regions (4 of these)

$$A_{tbfr} := \frac{top\_height}{2} \cdot \frac{top\_len}{3}$$

$R_{tbfr1} := Reluct\left(A_{tbfr}, 2 \cdot leg\_len + \frac{4}{4} \cdot top\_height + gap, mu_{air}\right)$ $R_{tbfr1} = 1.9337 \cdot 10^{9}$

$R_{tbfr2} := Reluct\left(A_{tbfr}, 2 \cdot leg\_len + \frac{12}{4} \cdot top\_height + gap, mu_{air}\right)$ $R_{tbfr2} = 2.4112 \cdot 10^{9}$

$R_{tbfr} := Parallel\left(R_{tbfr1}, R_{tbfr2}\right)$ $R_{tbfr} = 1.0731 \cdot 10^{9}$

Final Reluctance Values

$R_{center} = 2.1015 \cdot 10^{4}$	$R_{gap\_center} = 3.9579 \cdot 10^{6}$	$R_{cntr\_fr1} = 1.7381 \cdot 10^{8}$
$R_{corner\_center} = 1.7797 \cdot 10^{4}$	$R_{gap\_leg} = 5.3052 \cdot 10^{6}$	$R_{cntr\_fr2} = 3.4048 \cdot 10^{8}$
$R_{topbar} = 1.4147 \cdot 10^{4}$	$R_{gap\_return} = 1.061 \cdot 10^{9}$	$R_{cntr\_fr3} = 5.0714 \cdot 10^{8}$
$R_{corner\_leg} = 1.384 \cdot 10^{4}$		
$R_{leg1} = 2.4757 \cdot 10^{4}$	$R_{hz1} = 5.3052 \cdot 10^{7}$	$R_{tbfr} = 1.0731 \cdot 10^{9}$
$R_{leg2} = 1.4147 \cdot 10^{4}$	$R_{hz2} = 8.8419 \cdot 10^{7}$	
$R_{leg3} = 1.061 \cdot 10^{3}$		
$R_{leg4} = 2.122 \cdot 10^{3}$		

$R_{fr1\_side} = 1.5402 \cdot 10^{8}$	$R_{fr1\_back} = 2.2736 \cdot 10^{8}$	$\rightarrow$	$R_{side\_fr1} = 9.182 \cdot 10^{7}$
$R_{fr2\_side} = 3.376 \cdot 10^{8}$	$R_{fr2\_back} = 4.8438 \cdot 10^{8}$	$\rightarrow$	$R_{side\_fr2} = 1.9894 \cdot 10^{8}$
$R_{fr3\_side} = 5.002 \cdot 10^{8}$	$R_{fr3\_back} = 7.0028 \cdot 10^{8}$	$\rightarrow$	$R_{side\_fr3} = 2.9178 \cdot 10^{8}$
$R_{fr4\_side} = 6.4522 \cdot 10^{8}$	$R_{fr4\_back} = 8.8419 \cdot 10^{8}$	$\rightarrow$	$R_{side\_fr4} = 3.7302 \cdot 10^{8}$
$R_{fr5\_side} = 7.7537 \cdot 10^{8}$	$R_{fr5\_back} = 1.0427 \cdot 10^{9}$	$\rightarrow$	$R_{side\_fr5} = 4.447 \cdot 10^{8}$
$R_{fr6\_side} = 1.2514 \cdot 10^{8}$	$R_{fr6\_back} = 1.6466 \cdot 10^{8}$	$\rightarrow$	$R_{side\_fr6} = 7.1104 \cdot 10^{7}$
$R_{fr7\_side} = 1.5714 \cdot 10^{8}$	$R_{fr7\_back} = 1.857 \cdot 10^{8}$	$\rightarrow$	$R_{side\_fr7} = 8.5119 \cdot 10^{7}$
$R_{fr8\_side} = 1.7224 \cdot 10^{8}$	$R_{fr8\_back} = 1.9422 \cdot 10^{8}$	$\rightarrow$	$R_{side\_fr8} = 9.1286 \cdot 10^{7}$

The following file listing is the Spice simulation output for the prototype transformer. The voltage corresponds to the magneto-motive force of 4 ampere-turns, and the resulting current is equivalent to the flux in webers. Note that if some of the fringing flux tubes were removed, the total equivalent reluctance of the model would increase and the total flux in the system would decrease.

******** H S P I C E -- H93A.02 12:32:33 96/07/10 pmax**
3d flux tubes model for 4:4 pancake transformer with leakage: complexity 3
****

v_mmf	1	0	4	r_tpbr2l	30	31	1.4147e+4
				r_tpbr1l	31	32	1.4147e+4
r_center1u	1	2	2.1015e+4	r_crnr2l	32	33	1.7797e+4
r_center2u	2	3	2.1015e+4	r_center3l	33	34	2.1015e+4
r_center3u	3	4	2.1015e+4	r_center2l	34	35	2.1015e+4
r_crnr2u	4	5	1.7797e+4	r_center1l	35	36	2.1015e+4
r_tpbr1u	5	6	1.4147e+4	r_gapcntr	36	0	3.9579e+6
r_tpbr2u	6	7	1.4147e+4	r_hz1u	3	10	5.3052e+7
r_tpbr3u	7	8	1.4147e+4	r_hz2u	2	11	8.8419e+7
r_crnr1u	8	9	1.3840e+4	r_hz1l	27	34	5.3052e+7
r_leg1au	9	10	2.4757e+4	r_hz2l	26	35	8.8419e+7
r_leg1bu	10	11	2.4757e+4	r_gaprtn	18	0	1.0610e+9
r_leg2u	11	12	1.4147e+4	r_sd_fr1	17	20	9.1820e+7
r_leg3au	12	13	1061	r_sd_fr2	16	21	1.9894e+8
r_leg4au	13	14	2122	r_sd_fr3	15	22	2.9178e+8
r_leg4bu	14	15	2122	r_sd_fr4	14	23	3.7302e+8
r_leg4cu	15	16	2122	r_sd_fr5	13	24	4.4470e+8
r_leg4du	16	17	2122	r_sd_fr6	11	26	7.1104e+7
r_leg3bu	17	18	1061	r_sd_fr7	10	27	8.5119e+7
r_gapleg	18	19	5.3052e+6	r_sd_fr8	9	28	9.1286e+7
r_leg3bl	19	20	1061				
r_leg4dl	20	21	2122	r_ctrfr1	2	35	1.7381e+8
r_leg4cl	21	22	2122	r_ctrfr2	3	34	3.4048e+8
r_leg4bl	22	23	2122	r_ctrfr3	4	33	5.0714e+8
r_leg4al	23	24	2122				
r_leg3al	24	25	1061	r_tb_fr1	5	32	1.0731e+9
r_leg2l	25	26	1.4147e+4	r_tb_fr2	6	31	1.0731e+9
r_leg1bl	26	27	2.4757e+4	r_tb_fr3	7	30	1.0731e+9
r_leg1al	27	28	2.4757e+4	r_tb_fr4	8	29	1.0731e+9
r_crnr1l	28	29	1.3840e+4	.op			
r_tpbr3l	29	30	1.4147e+4	.end			

****** operating point information tnom= 25.000 temp= 25.000

node = voltage	node = voltage	node = voltage
0:1 = 4.0000	0:2 = 3.9896	0:3 = 3.9794
0:4 = 3.9693	0:5 = 3.9609	0:6 = 3.9542
0:7 = 3.9476	0:8 = 3.9410	0:9 = 3.9345
0:10 = 3.9235	0:11 = 3.9130	0:12 = 3.9074
0:13 = 3.9069	0:14 = 3.9061	0:15 = 3.9053
0:16 = 3.9045	0:17 = 3.9037	0:18 = 3.9033
0:19 = 2.0480	0:20 = 2.0476	0:21 = 2.0468
0:22 = 2.0460	0:23 = 2.0452	0:24 = 2.0444
0:25 = 2.0439	0:26 = 2.0384	0:27 = 2.0280
0:28 = 2.0170	0:29 = 2.0106	0:30 = 2.0041
0:31 = 1.9975	0:32 = 1.9908	0:33 = 1.9825
0:34 = 1.9725	0:35 = 1.9624	0:36 = 1.9521

**** voltage sources

subckt

element	0:v_mmf
volts	4.0000
current	-496.8835n
power	1.9875µ

total voltage source power dissipation= 1.9875µ watts

**** resistors

subckt

element	0:r_center	0:r_center	0:r_center	0:r_crnr2u	0:r_tpbr1u	0:r_tpbr2u
r value	21.0150k	21.0150k	21.0150k	17.7970k	14.1470k	14.1470k
v drop	10.4420m	10.1787m	10.0327m	8.4267m	6.6725m	6.6467m
current	496.8835n	484.3547n	477.4073n	473.4895n	471.6537n	469.8302n
power	5.1885n	4.9301n	4.7897n	3.9900n	3.1471n	3.1228n

element	0:r_tpbr3u	0:r_crnr1u	0:r_leg1au	0:r_leg1bu	0:r_leg2u	0:r_leg3au
r value	14.1470k	13.8400k	24.7570k	24.7570k	14.1470k	1.0610k
v drop	6.6211m	6.4525m	11.0222m	10.4969m	5.6376m	422.8079u
current	468.0190n	466.2202n	445.2147n	423.9985n	398.4994n	398.4994n
power	3.0988n	3.0083n	4.9072n	4.4507n	2.2466n	168.4887p

element	0:r_leg4au	0:r_leg4bu	0:r_leg4cu	0:r_leg4du	0:r_leg3bu	0:r_gapleg
r value	2.1220k	2.1220k	2.1220k	2.1220k	1.0610k	5.3052x
v drop	836.7280u	826.1418u	812.6201u	792.8053u	374.9553u	1.8553
current	394.3110n	389.3223n	382.9501n	373.6123n	353.3980n	349.7191n
power	329.9311p	321.6354p	311.1929p	296.2018p	132.5085p	648.8444n

element	0:r_leg3bl	0:r_leg4dl	0:r_leg4cl	0:r_leg4bl	0:r_leg4al	0:r_leg3al
r value	1.0610k	2.1220k	2.1220k	2.1220k	2.1220k	1.0610k
v drop	371.0520u	784.9987u	804.8135u	818.3352u	828.921u	418.9046u
current	349.7191n	369.9334n	379.2712n	385.6434n	390.632n	394.8205n
power	129.7640p	290.3973p	305.2426p	315.5855p	323.803p	165.3921p

element	0:r_leg2l	0:r_leg1bl	0:r_leg1al	0:r_crnr1l	0:r_tpbr3l	0:r_tpbr2l
r value	14.1470k	24.7570k	24.7570k	13.8400k	14.1470k	14.1470k
v drop	5.5855m	10.4060m	10.9315m	6.4018m	6.5692m	6.5949m
current	394.8205n	420.3265n	441.5510n	462.5564n	464.3553n	466.1664n
power	2.2053n	4.3739n	4.8268n	2.9612n	3.0505n	3.0743n

element	0:r_tpbr1l	0:r_crnr2l	0:r_center	0:r_center	0:r_center	0:r_gapcnt
r value	14.1470k	17.7970k	21.0150k	21.0150k	21.0150k	3.9579x
v drop	6.6207m	8.3615m	9.9557m	10.1015m	10.3647m	1.9521
current	467.9899n	469.8258n	473.7436n	480.6827n	493.2046n	493.2046n
power	3.0984n	3.9284n	4.7165n	4.8556n	5.1119n	962.7621n

element	0:r_hz1u	0:r_hz2u	0:r_hz1l	0:r_hz2l	0:r_gaprtn	0:r_sd_fr1
r value	53.0520x	88.4190x	53.0520x	88.4190x	1.0610g	91.8200x
v drop	55.8743m	76.5500m	55.4352m	75.9428m	3.9033	1.8561
current	1.0532n	865.7637p	1.0449n	858.8967p	3.6789n	20.2143n
power	58.8468p	66.2742p	57.9255p	65.2270p	14.3598n	37.5193n

element	0:r_sd_fr2	0:r_sd_fr3	0:r_sd_fr4	0:r_sd_fr5	0:r_sd_fr6	0:r_sd_fr7
r value	198.9400x	291.7800x	373.0200x	444.7000x	71.1040x	85.1190x
v drop	1.8577	1.8593	1.8609	1.8626	1.8746	1.8955
current	9.3378n	6.3722n	4.9888n	4.1884n	26.3648n	22.2694n
power	17.3463n	11.8476n	9.2837n	7.8012n	49.4248n	42.2127n

element	0:r_sd_fr8	0:r_ctrfr1	0:r_ctrfr2	0:r_ctrfr3	0:r_tb_fr1	0:r_tb_fr2
r value	91.2860x	173.8100x	340.4800x	507.1400x	1.0731g	1.0731g
v drop	1.9175	2.0271	2.0069	1.9869	1.9701	1.9568
current	21.0054n	11.6630n	5.8942n	3.9178n	1.8359n	1.8235n
power	40.2780n	23.6424n	11.8288n	7.7841n	3.6168n	3.5682n

element	0:r_tb_fr3	0:r_tb_fr4
r value	1.0731g	1.0731g
v drop	1.9435	1.9304
current	1.8112n	1.7989n
power	3.5201n	3.4724n

Appendix D: Prototype Driving-Point Impedance Tests

Driving point impedance measurements were performed on the four basic transformers examined in Chapter 5: Helical, Concentric, Adjacent, and LPKF. Two frequency sweeps were done, first with the secondary open circuited and the second with it short-circuited. As the magnitude of the measurements changed, the resolution of the HP 4192 Impedance Analyzer used changed, resulting in a variable number of significant digits in the data. The test connections were made with a four lead probe where the driving leads were connected at the ends of leads that were approximately 1.5 to 2 inches in length. However, the sense leads were attached as closely to the actual windings as possible by stripping a centimeter of the leads flush with the transformer body and connecting the sense leads there.

	Helical Prototype		Concentric Prototype		Adjacent Prototype		LPKF Prototype	
Frequency	Open Circuit	Short Circuit	Open Circuit	Short Circuit	Open Circuit	Short Circuit	Open Circuit	Short Circuit
5 Hz.	0.023 - 0.001i	0.023 - 0.001i	0.004 - 0.001i	0.005 - 0.001i	0.007 - 0.001i	0.007 - 0.001i	0.102 + 0.000i	0.104 + 0.000i
7	0.024 - 0.001i	0.024 - 0.001i	0.005 - 0.001i	0.005 - 0.001i	0.008 - 0.001i	0.008 - 0.001i	0.103 + 0.000i	0.104 + 0.000i
10	0.025 - 0.001i	0.025 - 0i	0.006 - 0.001i	0.006 - 0.001i	0.008 - 0.001i	0.008 - 0.001i	0.103 + 0.000i	0.103 + 0.000i
30	0.026 + 0.001i	0.026 + 0.001i	0.007 + 0.001i	0.007 + 0.001i	0.009 + 0.001i	0.009 + 0.001i	0.103 + 0.002i	0.103 + 0.002i
70	0.025 + 0.004i	0.026 + 0.004i	0.006 + 0.004i	0.007 + 0.004i	0.009 + 0.004i	0.009 + 0.004i	0.103 + 0.005i	0.104 + 0.004i
100	0.025 + 0.005i	0.026 + 0.005i	0.006 + 0.005i	0.007 + 0.005i	0.008 + 0.006i	0.009 + 0.005i	0.103 + 0.006i	0.104 + 0.005i
300	0.026 + 0.017i	0.033 + 0.013i	0.007 + 0.016i	0.015 + 0.008i	0.010 + 0.018i	0.016 + 0.014i	0.104 + 0.016i	0.105 + 0.016i
700	0.026 + 0.039i	0.042 + 0.016i	0.008 + 0.037i	0.021 + 0.007i	0.010 + 0.041i	0.024 + 0.021i	0.103 + 0.037i	0.114 + 0.034i
1 kHz.	0.026 + 0.056i	0.045 + 0.017i	0.008 + 0.053i	0.022 + 0.005i	0.011 + 0.058i	0.027 + 0.024i	0.103 + 0.053i	0.123 + 0.044i
3	0.027 + 0.167i	0.049 + 0.028i	0.008 + 0.160i	0.023 + 0.003i	0.014 + 0.171i	0.039 + 0.047i	0.103 + 0.160i	0.175 + 0.059i
7	0.028 + 0.389i	0.050 + 0.058i	0.008 + 0.372i	0.024 + 0.005i	0.018 + 0.393i	0.052 + 0.086i	0.103 + 0.374i	0.202 + 0.049i
10	0.029 + 0.555i	0.050 + 0.081i	0.008 + 0.532i	0.024 + 0.006i	0.020 + 0.559i	0.058 + 0.115i	0.104 + 0.533i	0.207 + 0.049i
30	0.037 + 1.659i	0.056 + 0.235i	0.010 + 1.594i	0.024 + 0.016i	0.029 + 1.660i	0.082 + 0.294i	0.111 + 1.598i	0.211 + 0.087i
70	0.050 + 3.853i	0.066 + 0.535i	0.013 + 3.718i	0.025 + 0.035i	0.042 + 3.859i	0.111 + 0.640i	0.139 + 3.718i	0.214 + 0.186i
100 kHz.	0.058 + 5.499i	0.073 + 0.758i	0.018 + 5.315i	0.026 + 0.050i	0.050 + 5.509i	0.128 + 0.894i	0.168 + 5.299i	0.217 + 0.262i
200	0.091 + 11.088i	0.089 + 1.494i	0.039 + 10.683i	0.028 + 0.097i	0.085 + 11.038i	0.172 + 1.726i	0.273 + 10.547i	0.227 + 0.514i
300	0.15 + 16.59i	0.101 + 2.227i	0.09 + 16.18i	0.031 + 0.143i	0.15 + 16.66i	0.203 + 2.548i	0.39 + 15.83i	0.236 + 0.761i
400	0.24 + 22.28i	0.111 + 2.958i	0.19 + 21.87i	0.033 + 0.189i	0.25 + 22.43i	0.228 + 3.368i	0.52 + 21.20i	0.244 + 1.007i
500	0.44 + 28.16i	0.120 + 3.691i	0.40 + 27.87i	0.035 + 0.235i	0.47 + 28.43i	0.251 + 4.188i	0.75 + 26.75i	0.253 + 1.252i
600	0.95 + 34.28i	0.130 + 4.428i	0.95 + 34.30i	0.037 + 0.280i	1.03 + 34.75i	0.274 + 5.009i	1.25 + 32.53i	0.260 + 1.496i
700	2.16 + 40.17i	0.143 + 5.165i	2.37 + 40.74i	0.039 + 0.326i	2.36 + 40.89i	0.300 + 5.829i	2.42 + 38.13i	0.267 + 1.739i
800	2.91 + 45.26i	0.154 + 5.898i	3.47 + 46.28i	0.041 + 0.370i	3.24 + 46.23i	0.320 + 6.641i	3.20 + 42.92i	0.273 + 1.981i
900	3.25 + 51.02i	0.161 + 6.632i	3.91 + 52.81i	0.043 + 0.416i	3.65 + 52.35i	0.335 + 7.462i	3.52 + 48.34i	0.278 + 2.223i
1 MHz.	3.96 + 57.14i	0.170 + 7.358i	4.90 + 60.15i	0.045 + 0.461i	4.50 + 58.96i	0.352 + 8.287i	4.19 + 54.13i	0.283 + 2.466i
1.2	6.32 + 69.44i	0.193 + 8.844i	8.53 + 76.05i	0.049 + 0.551i	7.38 + 72.60i	0.393 + 9.942i	6.45 + 65.82i	0.293 + 2.952i
1.4	9.38 + 81.60i	0.219 + 10.327i	14.05 + 93.58i	0.052 + 0.641i	11.32 + 86.60i	0.438 + 11.605i	9.37 + 77.42i	0.303 + 3.438i
1.6 MHz.	12.99 + 93.90i	0.247 + 11.804i	21.95 + 113.67i	0.056 + 0.732i	16.30 + 101.37i	0.49 + 13.28i	12.83 + 89.20i	0.312 + 3.924i

Table A1: Laboratory Measurements of Prototype Driving Point Impedances

Appendix E: Determination of Transformer Model Parameters

The non-linear regression procedure that determined the transformer model element values used the MATLAB code below. Two sets of empirical measurements are required, the complex driving point impedance values over the frequency range of interest when the secondary is open-circuited and when it is short-circuited. The regression is based on MATLAB's "fmins" function, which lists its functionality as

> FMINS Minimize a function of several variables.
> FMINS('F',X0) attempts to return a vector x which is a local minimizer of F(x) near the starting vector X0. 'F' is a string containing the name of the objective function to be minimized. F(x) should be a scalar valued function of a vector variable.

The "ZinFit" function below takes an array of values which correspond to the circuit elements of the transformer model. Using these values, it theoretically calculates the driving point impedance values for the circuit shown below, and produces an error value from the actual laboratory measurements. This value is returned to the fmins function which modifies the input array and calls ZinFit again, iterating until the error is minimized. To execute the optimization, the following steps must be taken:

1. "Datao" and "Datas" must be declared as global in the main workspace and contain the open and short circuit driving point impedances values in complex form.
2. "Hz" must be declared as a global and contain the array of frequency values.
3. "X0" must contain the array of initial guesses for the transformer parameters.
4. The optimization is run with the command: "Parms = fmins('zinfit'),X0)"

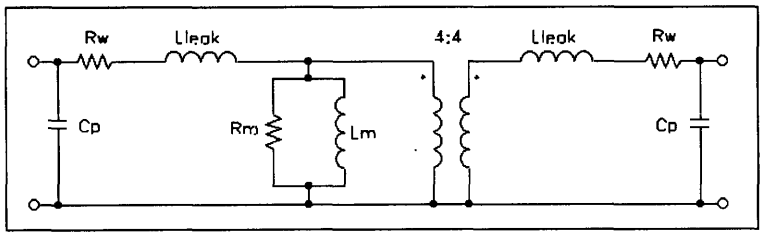

Figure A-1: Simplified Standard Transformer Model

```
function [error] = zinfit(parms)
%ZINFIT takes a vector of transformer parameters:
%       PARMS = [Lmag,Lleak,Rwind,Rcore,Cparasitic]
% and minimizes the error between the driving impedance vector produced over a frequency range
% (5 Hz to 1 MHz) and a vector of  measured values

global Hz;
global Datao;
global Datas;

% Set transformer parameters from argument vector
Lm = parms(1);
Ll = parms(2);
Rw = parms(3);
Rm = parms(4);
Cp = parms(5);

% Loop 24 times for 24 frequency points (5 Hz to 1.0 MHz)
for loop1 = 1:24
        s = i*2*pi*Hz(loop1);

%-----------------------
% Simple Topology Model
%-----------------------
%       Zin_open(loop1) = Rw + (Ll+Lm)*s;
%       Zin_short(loop1) = Ll*s + Rw + (Lm*s*(Ll*s + Rw)/((Lm+Ll)*s + Rw));
% -- End Simple Model --

%------------------------
% Complex Topology Model
%------------------------
  % Open Circuit Calculations
        Z1 = Ll*Cp*s^2 + Rw*Cp*s + 1;
        Z2 = Z1*(Lm*s+Rm) + (Lm*Rm*Cp*s^2);
        Zin_open(loop1) = (Lm*Rm*s*Z1 + (Rw+Ll*s)*Z2)/(Z2 + Cp*s*(Lm*Rm*s*Z1 +
(Rw+Ll*s)*Z2));

  % Short Circuit Calculations
        Z3 = (Lm*s + Rm)*(Ll*s + Rw) + Lm*Rm*s;
        Zin_short(loop1) = ((Lm*Rm*s+Z3) * (Ll*s+Rw))/(Z3 + Cp*s*(Ll*s+Rw)*(Z2+Lm*Rm*s));
% -- End Complex Model --

end

Zin_theory = [Zin_open.'; Zin_short.'];
Zin_lab = [Datao(1:24); Datas(1:24)];
e = (Zin_lab - Zin_theory) ./ abs(Zin_lab);

error = norm(e)
```

4:4 Helical Geometry

For the complex topology plots that follow, the markers correspond to the measured data points in the laboratory and the solid lines correspond to the values theoretically derived from the best fit parameters.

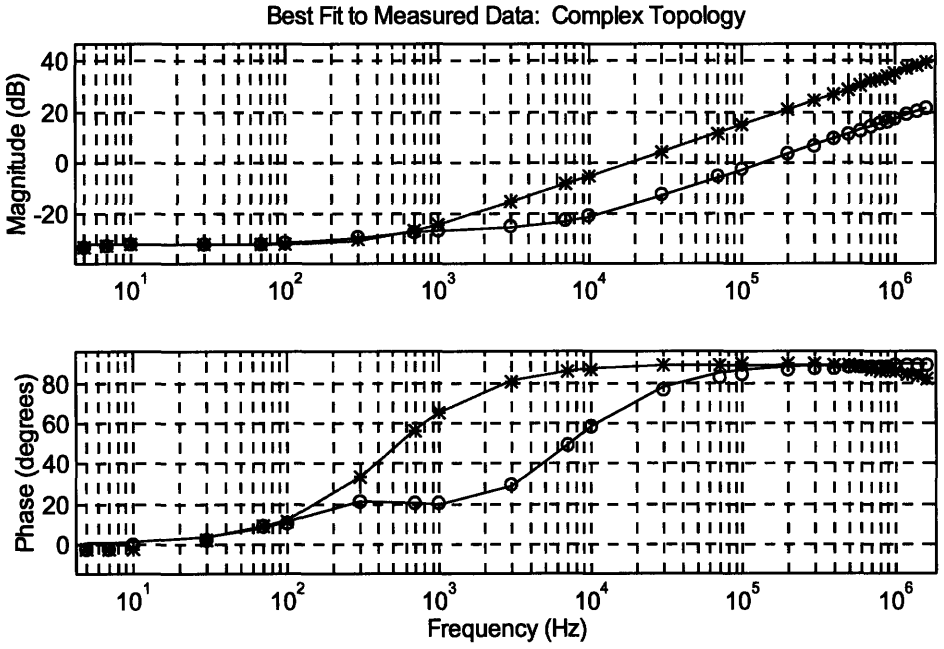

Best Fit Parameters:

Lm = 8.2358 μH	Lleak = 0.61915 μH
Rw = 25.1 mΩ	Rm = 760.6442 Ω
Cp = 53.330 pF	

Corresponding Driving Point Impedances for Best Fit Parameters

Zin_open =		Zin_short =	
	0.0424 + 3.8952i		0.0469 + 0.5257i
0.0251 + 0.0003i	0.0603 + 5.5654i	0.0251 + 0.0003i	0.0470 + 0.7509i
0.0251 + 0.0004i	0.1663 +11.1410i	0.0251 + 0.0004i	0.0475 + 1.5018i
0.0251 + 0.0006i	0.3439 +16.7371i	0.0251 + 0.0006i	0.0484 + 2.2528i
0.0251 + 0.0017i	0.5946 +22.3639i	0.0252 + 0.0017i	0.0496 + 3.0039i
0.0251 + 0.0039i	0.9204 +28.0320i	0.0256 + 0.0038i	0.0512 + 3.7553i
0.0251 + 0.0056i	1.3240 +33.7521i	0.0261 + 0.0053i	0.0531 + 4.5069i
0.0251 + 0.0167i	1.8089 +39.5352i	0.0318 + 0.0123i	0.0554 + 5.2589i
0.0251 + 0.0389i	2.3789 +45.3927i	0.0404 + 0.0151i	0.0580 + 6.0113i
0.0251 + 0.0556i	3.0392 +51.3363i	0.0431 + 0.0156i	0.0610 + 6.7641i
0.0251 + 0.1669i	3.7955 +57.3783i	0.0463 + 0.0257i	0.0644 + 7.5173i
0.0253 + 0.3895i	5.6237 +69.8090i	0.0467 + 0.0540i	0.0721 + 9.0256i
0.0255 + 0.5564i	7.9313 +82.7948i	0.0468 + 0.0761i	0.0813 +10.5365i
0.0283 + 1.6692i	10.8076 +96.4580i	0.0468 + 0.2256i	0.0920 +12.0504i

4:4 Helical Geometry

Using the best fit parameters from the complex model, omitting the parasitic capacitances and the core losses produces the following curves of the driving point impedances. Rather than comparing the calculated values to the lab measurements, the markers correspond to the values calculated with the complex topology and the solid lines the simple topology.

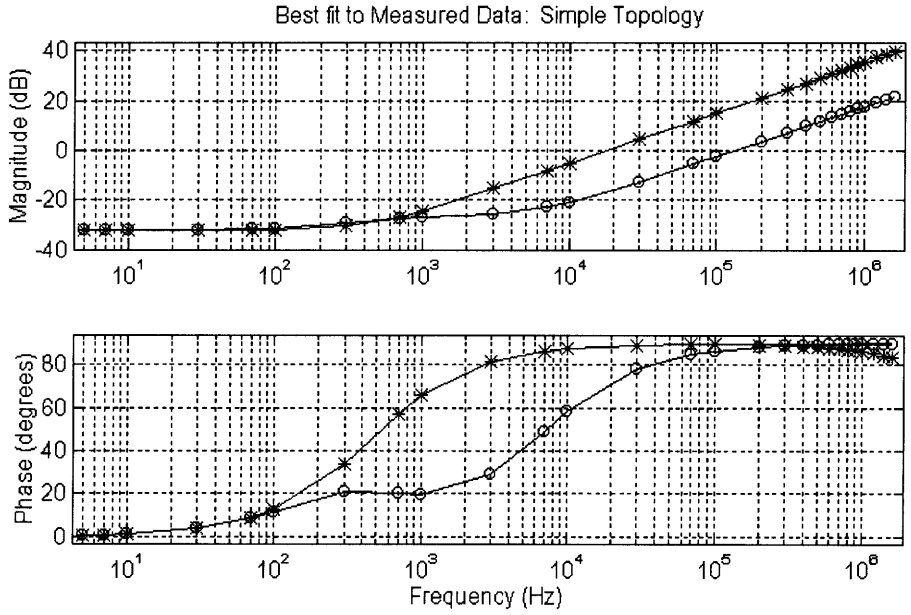

Notice that the correlation between the points derived with the two methods is very good except around 1 MHz, where the phase fails to track.

High Frequency Region Zoom

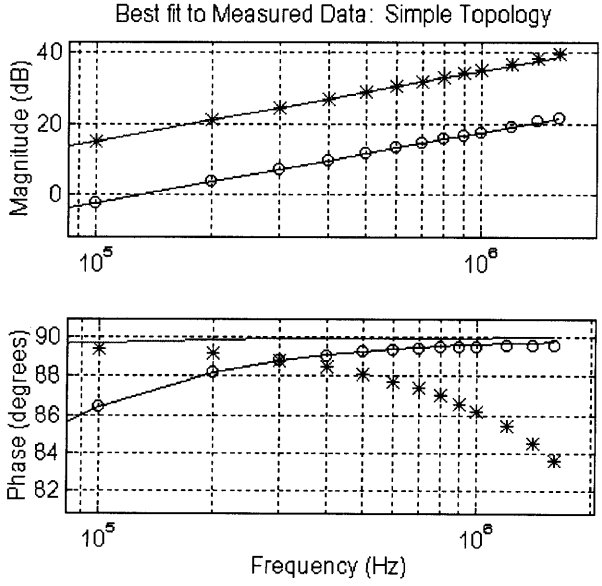

4:4 Concentric Geometry

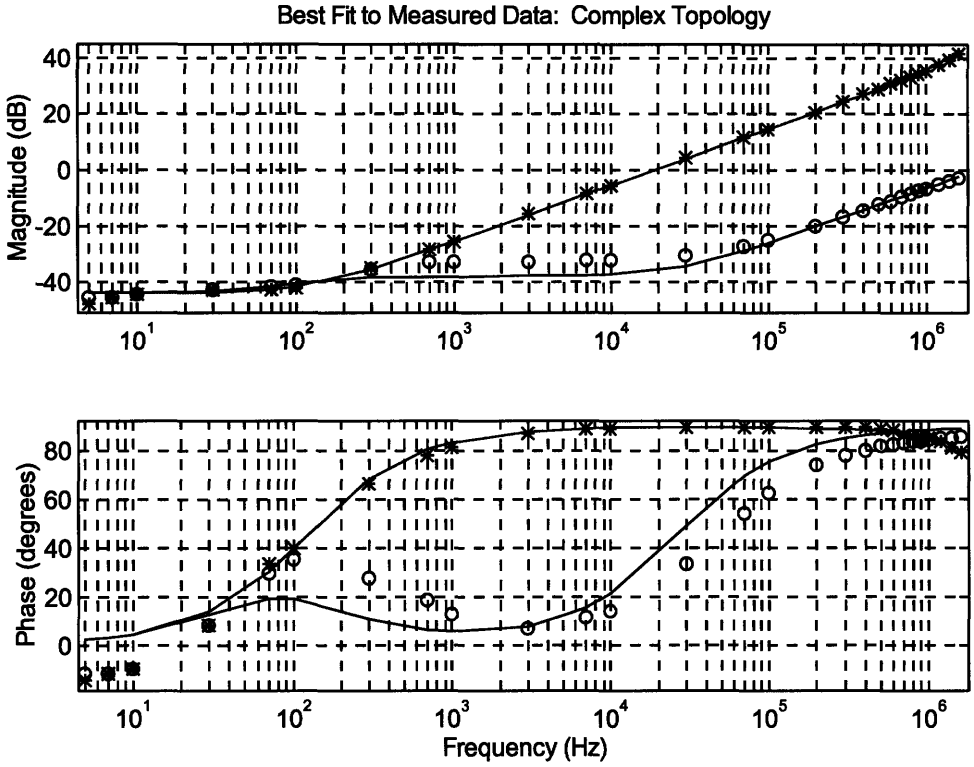

Best Fit Parameters:

Lm = 8.2989 μH	Lleak = 37.893 nH
Rw = 6.215 mΩ	Rm = 790.5561 Ω
Cp = 233.36 pF	

Corresponding Driving Point Impedances for Best Fit Parameters

Zin_open =		Zin_short =	
	0.023097 + 3.669363i		0.012375 + 0.0332668i
0.006215 + 0.0002619i	0.040722 + 5.245924i	0.006226 + 0.0002614i	0.012375 + 0.0475165i
0.006215 + 0.0003667i	0.145501 + 10.53886i	0.006236 + 0.0003654i	0.012378 + 0.0950230i
0.006215 + 0.0005238i	0.324423 + 15.92721i	0.006259 + 0.0005202i	0.012382 + 0.1425340i
0.006215 + 0.0015714i	0.584232 + 21.46218i	0.006585 + 0.0014779i	0.012388 + 0.1900485i
0.006215 + 0.0036667i	0.935034 + 27.19947i	0.007806 + 0.0027286i	0.012395 + 0.2375673i
0.006215 + 0.0052381i	1.391046 + 33.20112i	0.008773 + 0.0030825i	0.012404 + 0.2850911i
0.006216 + 0.0157144i	1.971716 + 39.53790i	0.011541 + 0.0022490i	0.012415 + 0.3326210i
0.006217 + 0.0366669i	2.703364 + 46.29217i	0.012202 + 0.0013474i	0.012427 + 0.3801578i
0.006219 + 0.0523813i	3.621575 + 53.56175i	0.012289 + 0.0011957i	0.012441 + 0.4277026i
0.006246 + 0.1571442i	4.774727 + 61.46483i	0.012365 + 0.0016685i	0.012457 + 0.4752563i
0.006384 + 0.3666720i	8.077854 + 79.78915i	0.012373 + 0.0034300i	0.012493 + 0.5703947i
0.006559 + 0.5238211i	13.54136 + 102.9455i	0.012374 + 0.0048240i	0.012536 + 0.6655807i
0.009312 + 1.571650i	23.14669 + 133.7492i	0.012374 + 0.0142771i	0.012585 + 0.7608224i

4:4 Concentric Geometry

Simple Topology Theoretical Plot with Points Derived from Complex Topology

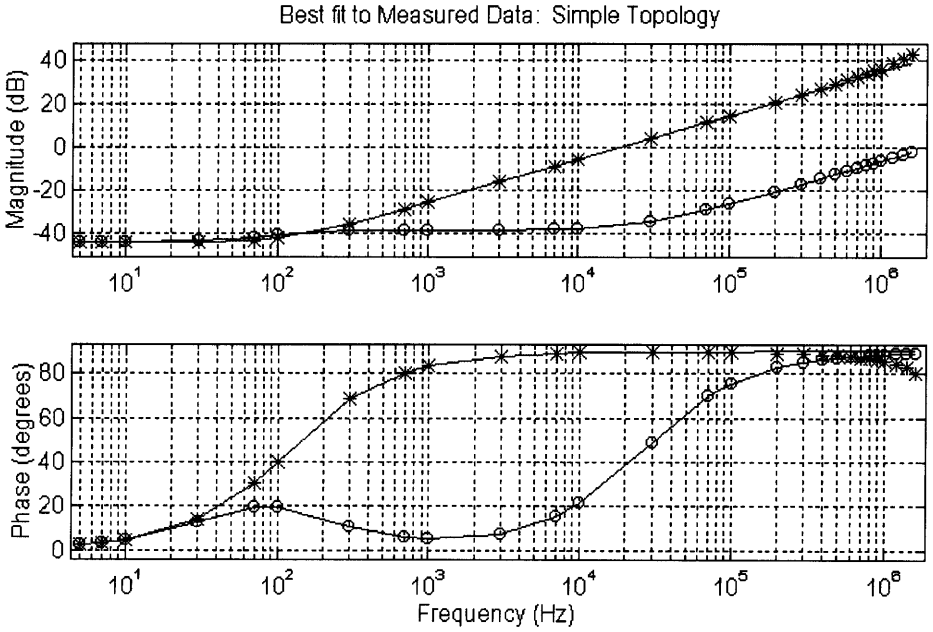

High Frequency Region Zoom

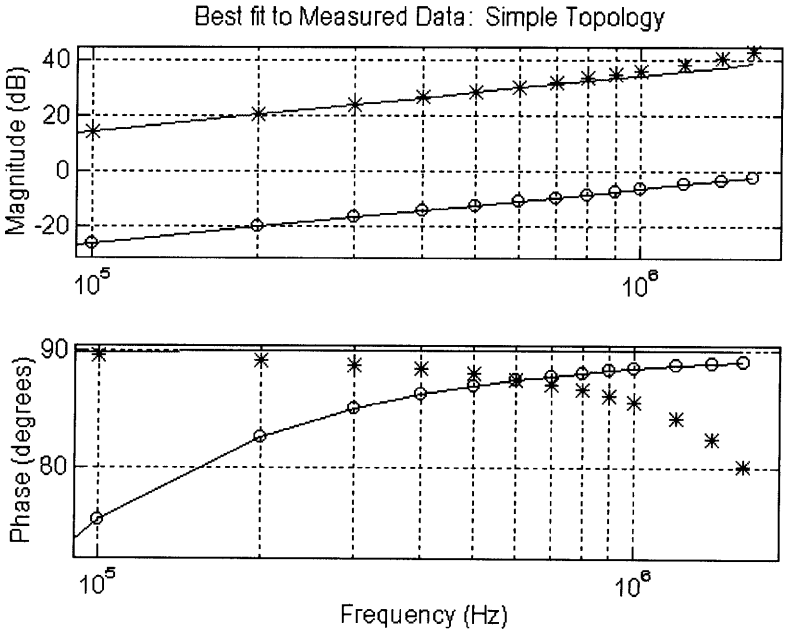

4:4 Adjacent Geometry

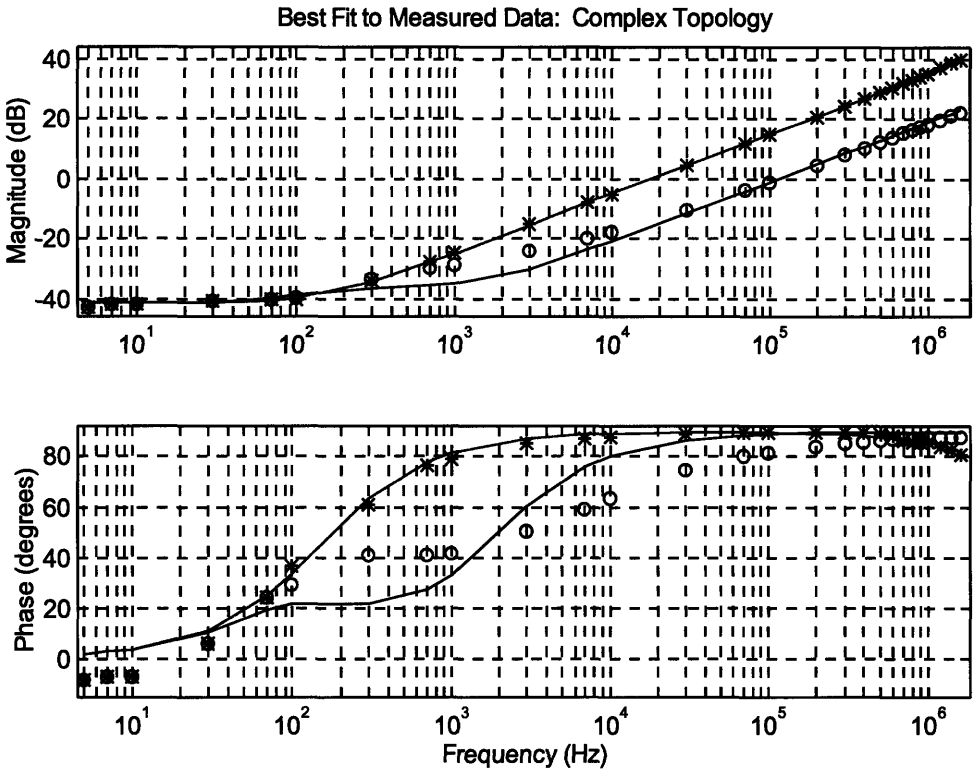

Best Fit Parameters:

Lm = 8.1787 μH	Lleak = 0.7452 μH
Rw = 8.4032 mΩ	Rm = 664.1380 Ω
Cp = 80.3984 pF	

Corresponding Driving Point Impedances for Best Fit Parameters

Zin_open =		Zin_short =	
	0.027899 + 3.9258250i		0.015599 + 0.6281468i
0.008403 + 0.0002804i	0.048211 + 5.6096556i	0.008411 + 0.0002801i	0.015743 + 0.8973515i
0.008403 + 0.0003925i	0.168125 + 11.235031i	0.008419 + 0.0003918i	0.016589 + 1.7948029i
0.008403 + 0.0005607i	0.369631 + 16.891981i	0.008434 + 0.0005586i	0.017998 + 2.6924894i
0.008403 + 0.0016821i	0.655241 + 22.596627i	0.008675 + 0.0016277i	0.019973 + 3.5905244i
0.008403 + 0.0039249i	1.028550 + 28.365500i	0.009667 + 0.0033345i	0.022515 + 4.4890235i
0.008403 + 0.0056070i	1.494320 + 34.215686i	0.010578 + 0.0041561i	0.025625 + 5.3881027i
0.008404 + 0.0168211i	2.058591 + 40.164974i	0.014052 + 0.0055138i	0.029307 + 6.2878784i
0.008405 + 0.0392493i	2.728824 + 46.232026i	0.015152 + 0.0077262i	0.033562 + 7.1884676i
0.008407 + 0.0560704i	3.514084 + 52.436545i	0.015306 + 0.0100078i	0.038395 + 8.0899872i
0.008439 + 0.1682113i	4.425268 + 58.799467i	0.015444 + 0.0272714i	0.043808 + 8.9925549i
0.008598 + 0.3924937i	6.679914 + 72.091681i	0.015460 + 0.0629636i	0.056392 +10.801307i
0.008801 + 0.5607066i	9.629101 + 86.309079i	0.015463 + 0.0898379i	0.071355 +12.615674i
0.011983 + 1.6821826i	13.46503 + 101.68693i	0.015487 + 0.2692323i	0.088739 +14.436617i

4:4 Adjacent Geometry

Simple Topology Theoretical Plot with Points Derived from Complex Topology

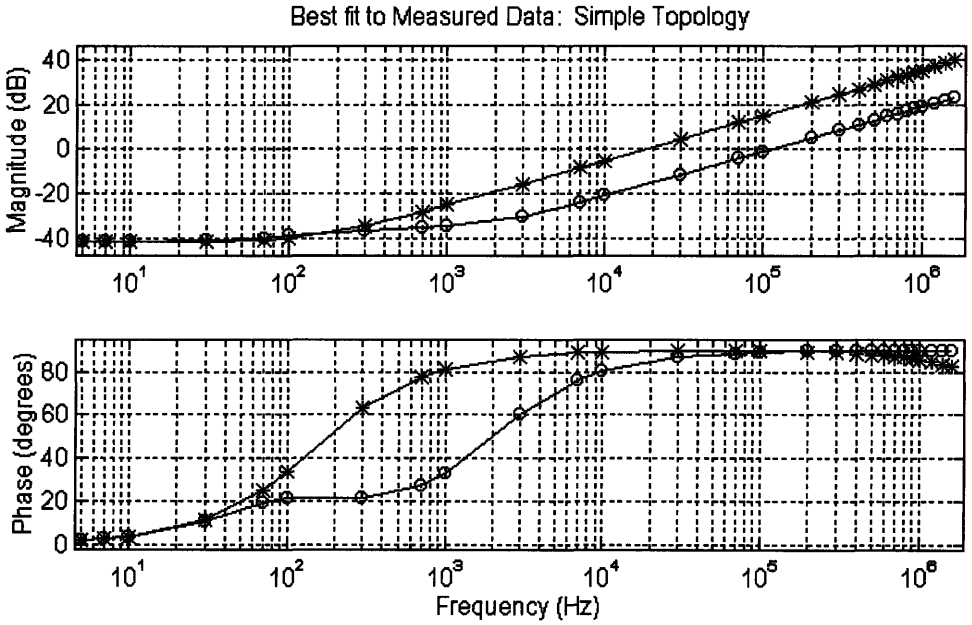

High Frequency Region Zoom

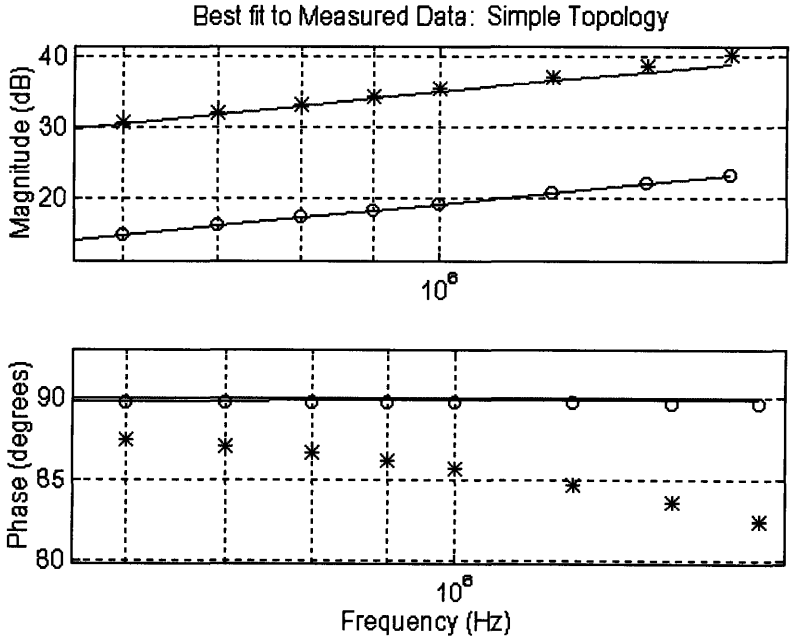

4:4 LPKF Geometry

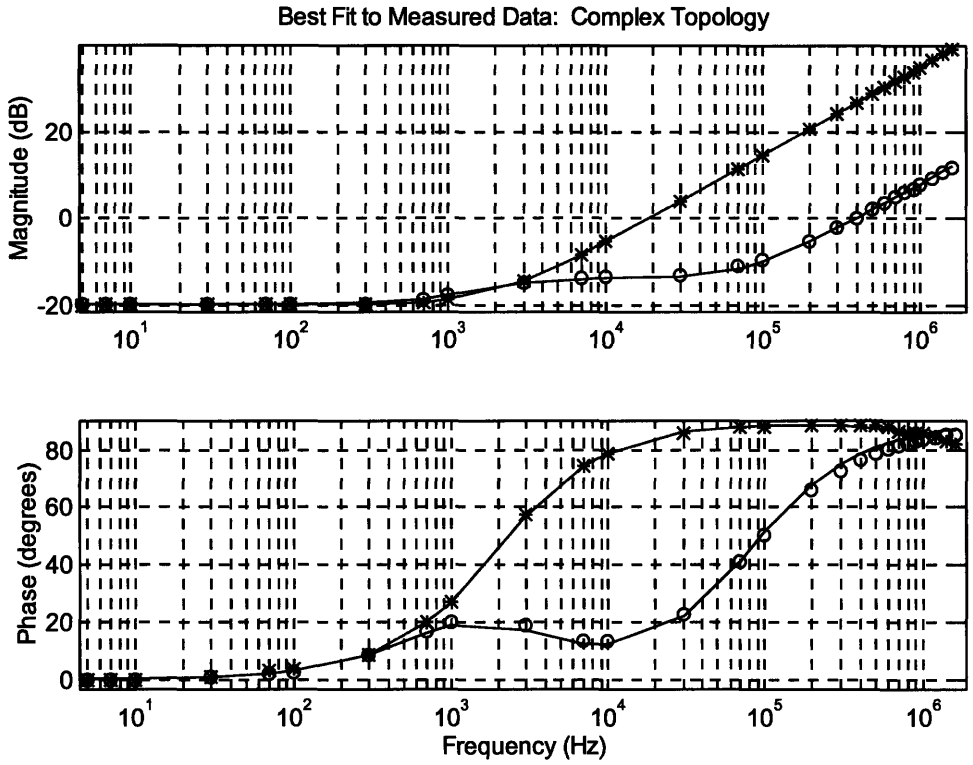

Best Fit Parameters:

Lm = 8.2935 μH Lleak = 0.2025 μH
Rw = 104.217 mΩ Rm = 672.9959 Ω
Cp = 15.961 pF

Corresponding Driving Point Impedances for Best Fit Parameters

Zin_open =		Zin_short =	
	0.123994 + 3.7368191i		0.203444 + 0.1787866i
0.104217 + 0.0002669i	0.144582 + 5.3384382i	0.104217 + 0.0002669i	0.203495 + 0.2533946i
0.104217 + 0.0003737i	0.265750 + 10.678349i	0.104218 + 0.0003737i	0.203594 + 0.5038851i
0.104217 + 0.0005338i	0.467942 + 16.021204i	0.104219 + 0.0005338i	0.203717 + 0.7550249i
0.104217 + 0.0016015i	0.751526 + 21.368467i	0.104240 + 0.0016011i	0.203883 + 1.0063316i
0.104217 + 0.0037367i	1.117018 + 26.721597i	0.104344 + 0.0037322i	0.204096 + 1.2577104i
0.104217 + 0.0053382i	1.565086 + 32.082040i	0.104477 + 0.0053249i	0.204354 + 1.5091308i
0.104217 + 0.0160146i	2.096546 + 37.451231i	0.106508 + 0.0156624i	0.204660 + 1.7605808i
0.104219 + 0.0373673i	2.712369 + 42.830587i	0.115531 + 0.0333101i	0.205013 + 2.0120553i
0.104221 + 0.0533819i	3.413682 + 48.221507i	0.124859 + 0.0428072i	0.205412 + 2.2635523i
0.104253 + 0.1601458i	4.201768 + 53.625365i	0.173976 + 0.0529337i	0.205859 + 2.5150714i
0.104415 + 0.3736736i	6.044209 + 64.477265i	0.196346 + 0.0432928i	0.206893 + 3.0181780i
0.104620 + 0.5338195i	8.253247 + 75.396687i	0.199866 + 0.0438163i	0.208116 + 3.5213830i
0.107849 + 1.6014644i	10.84520 + 86.393397i	0.203093 + 0.0818705i	0.209528 + 4.0246978i

4:4 LPKF Geometry

Simple Topology Theoretical Plot with Points Derived from Complex Topology

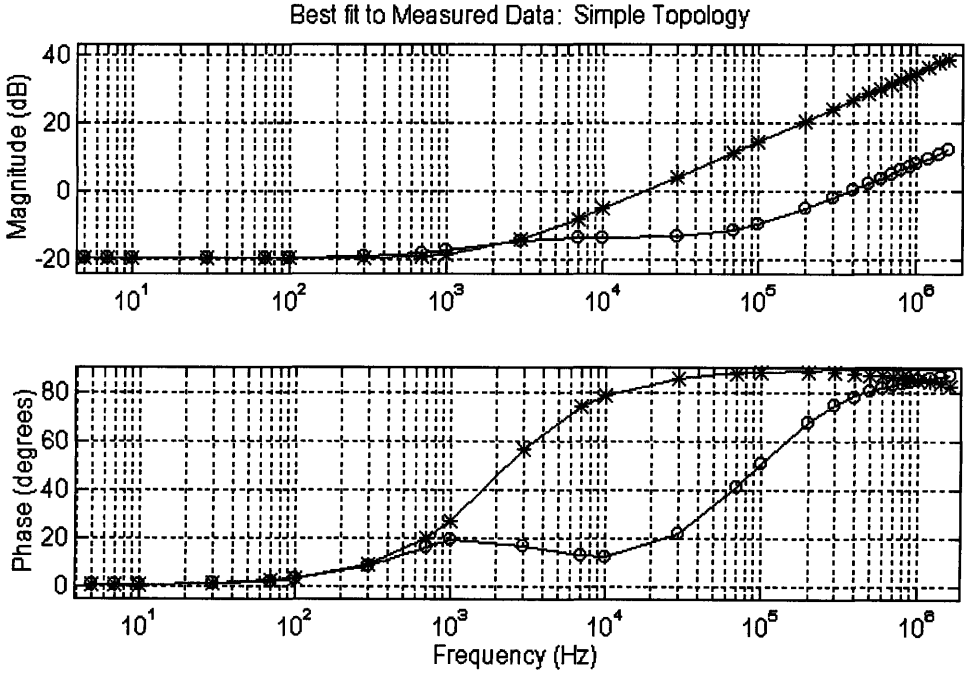

High Frequency Region Zoom

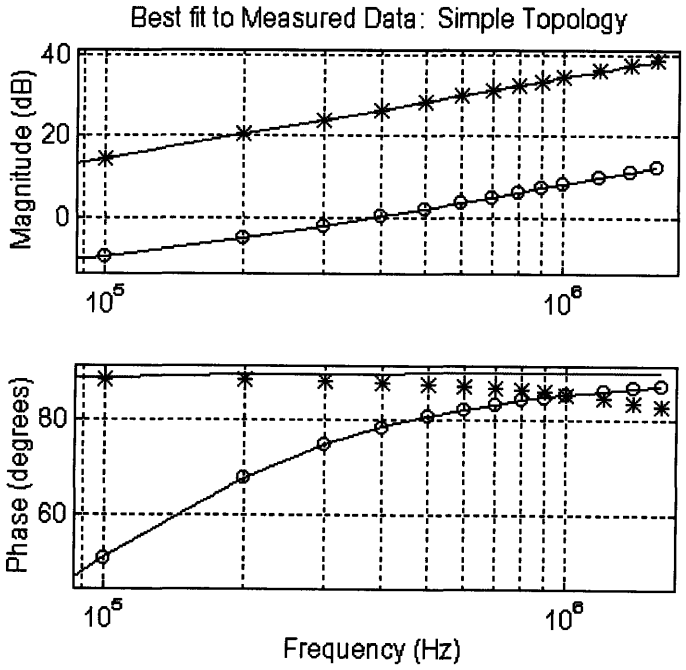

From the comparison of these four systems, it can be concluded that the parasitic capacitances and shunt resistances can be ignored in analyses around 100 kHz. In all four cases above, the correlation between the driving point impedances derived using the simplified instead of the complex circuit topology was extremely close, except in one area. The phase of the short circuit driving point impedance showed a droop characteristic of about 10 degrees around one MHz in both the laboratory measurements and the complex topology derived points but not the points derived with simplified topology. The difference was rarely much more than two degrees by 500 kHz, which is above the operating region of interest, so for systems similar to the prototypes, these circuit elements can be ignored.

The two geometries with large winding resistances (Helical and LPKF) had very close theoretical derivations with both the simple and complex circuit topologies. The two with small winding resistances (Concentric and Adjacent) had similar problems on the short-circuit driving point impedance plots for both magnitude and phase. The analyzer accurately measured the DC resistance of all four prototypes, so the error should not be attributed to lack of measurement precision. Alternative explanations are that another circuit elements needed to be added to the model, or that a non-linear effect was significant in the two concentrically wound prototypes but not in the adjacent prototypes.

Appendix F: Paddle DC Resistance Measurements

The measurement tools used for these experiments were an HP 6010A power supply capable of providing 200 volts at 17 amps, and a Fluke Series 77 multimeter. Measurements were taken by driving a fixed current through two of the four wires of the cable of the coupler and measuring the resulting voltages across various combinations of wires with the Fluke multimeter. Both five amps and eight amps were used as driving currents to compare answers. For the most part, the answers given by both currents were equivalent. Because of the larger values involved with the 8 amp tests, these values were used as the "official" results. In the conclusion sections of each measurement, W1 and W2 stand for the resistance of white wires numbers one and two, with the same coding scheme for the black wires. C stands for the coil resistance.

Driving Current: 5.00 Amps

Driving	Measurement	Conclusion
B1 to B2	B1 to B2 = 159 mV	B1 + B2 = 31.8 mOhms
W1 to W2	W1 to W2 = 158 mV	W1 + W2 = 31.6 mOhms
W1 to B2	W1 to B2 = 186 mV	W1 + C + B2 = 37.2 mOhms
	B1 to W2 = 29.8 mV	C = 5.96 mOhms
	W1 to W2 = 77.8 mV	W1 = 15.56 mOhms
	B1 to B2 = 74.6 mV	B2 = 14.92 mOhms
B1 to W2	B1 to W2 = 189 mV	B1 + C + W2 = 37.8 mOhms
	W1 to B2 = 2.8 mV	C = 5.96 mOhms
	W1 to W2 = 76.2 mV	W2 = 15.24 mOhms
	B1 to B2 = 76.2 mV	B1 = 15.24 mOhms

Driving Current: 8.00 Amps

Driving	Measurement	Conclusion
B1 to W2	B1 to W2 = 292.1 mV	B1 + C + W2 = 36.51 mOhms
	W1 to B2 = 47.9 mV	C = 5.99 mOhms
	W1 to W2 = 122.1 mV	W2 = 15.26 mOhms
	B1 to B2 = 122.2 mV	B1 = 15.28 mOhms

W1 to B2	W1 to B2 = 287.8 mV	W1 + C + B2 = 35.98 mOhms
	B1 to W2 = 47.9 mV	C = 5.99 mOhms
	W1 to W2 = 120.2 mV	W1 = 15.03 mOhms
	B1 to B2 = 119.6 mV	B2 = 14.95 mOhms
B1 to B2	B1 to B2 = 241.8 mV	B1 + B2 = 30.23 mOhms
	W1 to W2 = 0 mV	
	B1 to W2 = 122.1 mV	B1 = 15.26 mOhms
	W1 to B2 = 119.6 mV	B2 = 14.95 mOhms
W1 to W2	B1 to B2 = 0 mV	
	W1 to W2 = 241.9 mV	W1 + W2 = 30.24 mOhms
	W1 to B2 = 120.4 mV	W1 = 15.05 mOhms
	B1 to W2 = 122.1 mV	W2 = 15.26 mOhms

Results were chosen from the measurements where the single resistive component was isolated. The conclusions were drawn assuming that both cable wires of the same color were electrically connected at the point where they attached to the winding. Thus, the two black wires formed two resistors in parallel connected to one end of the helical coil, and the two white wires formed two resistors in parallel connected to the other end of the coil. An alternate hypothesis was that there were two independent coil windings as well, with one set of wires running connecting to one winding, and the second set of wires connecting to the other. The fact that cross-measurements can be taken, driving one set of wires and measuring voltages on the other set, mean that the two sets are not independent, and from the data it is clear that the assumed electrical connections are correct.

Thus, from these measurements, it is possible to conclude that at DC, the resistive components of the coupler are as follows:

White Wire #1 = 15.05 milliohms
White Wire #2 = 15.26 milliohms
Black Wire #1 = 15.26 milliohms
Black Wire #2 = 14.95 milliohms
Helical Coil = 5.99 milliohms

Appendix G: Preliminary Design Program

```
%=========================================================================%
%                                                                         %
% DETERMINATION OF TRANSFORMER EQUIVALENT CIRCUIT PARAMETERS %
%       FROM GEOMETRY AND MATERIAL PROPERTIES                             %
%                                                                         %
%=========================================================================%
%                                                                       %
% Assumptions:                                                          %
%  * A pot core or EE core is used.                                     %
%  * The significant dimension for the core is the radius of the center leg.  %
%  * The core is gapped                                                 %
%  * A helical winding geometry is used                                 %
%  * The secondary is split in two parts around the primary             %
%                                                                       %
%=======================================================================%

%-------------------------------------------------------------------------
% Since there is no interface at this time, change the values
% in the "Parameters" section here to modify the program
%-------------------------------------------------------------------------

% Parameters
%-------------------------------------------------------------------------
G_L     = 0.8;          % Total Gap Length                      (in mm)
C_R     = 34.0;         % Core Center Leg Radius        (in mm)
IW_R    = 39.0;         % Inner Winding Radius                  (in mm)
OW_R    = 59.0;         % Outer Winding Radius                  (in mm)
C_T     = 0.21;         % Conductor Thickness                   (in mm)
WP_T    = 3.5;          % Thickness of Primary Winding Pack     (in mm)
WP_S    = 4.5;          % Separation between Winding Packs      (in mm)
rho_core= 1.0;          % Nominal Core Resistivity              (in Ohm-m)
eps_r   = 200000;       % Relative Permittivity of Core
mu_r    = 2000;         % Relative Permeability of Core
f       = 80000;        % frequency of operation                (in Hz)
Zload   = 10;           % load impedance                        (in Ohms)
PTurns  = 4;            % Number of Primary turns
STurns  = 4;            % Number of Secondary turns             (even #'s only)

%-------------------------------------------------------------------------

% Physics Constants and Unit Adjustments
%-------------------------------------------------------------------------

mu0     = 4*pi*1e-7;
eps0    = 8.854e-12;
mu      = mu_r * mu0;
eps     = eps_r * eps0;
rho_cu  = 1.673e-8;
```

```
w       = 2 * pi * f;
G_L     = G_L / 1000;
C_R     = C_R / 1000;
IW_R    = IW_R / 1000;
OW_R    = OW_R / 1000;
C_T     = C_T / 1000;
WP_T    = WP_T / 1000;
WP_S    = WP_S / 1000;
WP_G    = (WP_T - (PTurns*C_T)) / (PTurns-1);

if WP_G <= 0
        disp ('Error:  No gaps exist between conductors.')
        disp ('Increase thickness of winding packs or reduce number of turns')
        disp ('Program aborted')
        return
end
%-------------------------------------------------------------------------------

%=============================================================================%
%                                  Calculations                               %
%=============================================================================%

%-------------------------------------------------------------------------------
% Calculation of the Skin Depth in the Core
%-------------------------------------------------------------------------------

        % High Conductivity Skin Depth
delta_hc = sqrt((2*rho_core)/(w*mu));

        % Correction Factor for high resistivity materials
delta_correction = 1 / sqrt(sqrt(1+(w*eps*rho_core)^2) - w*eps*rho_core);

        % Final skin depth
sd_core = delta_hc * delta_correction        % Real Skin depth

% sd_core = delta_hc;              % Maxwell skin depth (Maxwell ignores displacement currents)

%-------------------------------------------------------------------------------
% Open Circuit Secondary Inductance (Lopen - primary side)
%-------------------------------------------------------------------------------

        % DC Estimate
        %   Drive the primary with 1 ampere, making N*i amp-turns of MMF
        %       For a uniform field in the gap (ignoring crowding due to geometry)
        %       the reluctance of the gap is R = gap_length / (mu0 * A_gap)

DC_Gap_Reluctance = G_L / (mu0 * pi * C_R^2);
Lopen_DC = PTurns^2 / DC_Gap_Reluctance;
```

```
        % Conservative AC Estimate
sd_ratio = C_R / sd_core;
K_denom = cos(sd_ratio)^2 * cosh(sd_ratio)^2 + sin(sd_ratio)^2 * sinh(sd_ratio)^2;
K_c = cos(sd_ratio) * cosh(sd_ratio) / K_denom;
K_s = sin(sd_ratio) * sinh(sd_ratio) / K_denom;

K_AC1 = K_c * (sd_ratio * (cos(sd_ratio)*sinh(sd_ratio) + sin(sd_ratio)*cosh(sd_ratio)) -
        sin(sd_ratio)*sinh(sd_ratio));
K_AC2 = K_s * (sd_ratio * (sin(sd_ratio)*cosh(sd_ratio) - cos(sd_ratio)*sinh(sd_ratio)) +
        cos(sd_ratio)*cosh(sd_ratio) - 1);
K_AC = (K_AC1 + K_AC2) / sd_ratio^2

Lopen_AC = K_AC * Lopen_DC;

%-------------------------------------------------------------------------------------
% Short Circuit Equivalent Leakage Inductance (Lshort)
%-------------------------------------------------------------------------------------

        % AC and DC Estimates are the same

        % Clear array variables
clear U;
clear U2;

        % First determine the number of winding gaps in the triangle
        % Split the gaps into gaps with rising field levels and falling field levels
TRatio = PTurns/STurns;
Rslots = STurns/2;
Fslots = floor((PTurns-1)/2);

        % Determine the magnetic stored energies in each level of the triangle
        % Because of the split secondary, the 2nd (negative) triangle will be identical

        % Rising levels
for i = 1:Rslots
        U(i) = mu0*pi*WP_G*TRatio^2*i^2 / log(OW_R/IW_R);
end
        % Peak level with larger gap distance
U(Rslots) = U(Rslots) * WP_S / WP_G;
        % Falling levels
for i=(Rslots+1):(Rslots+Fslots)
        U(i) = mu0*pi*WP_G*(Rslots*(TRatio+1)-i)^2 / log(OW_R/IW_R);
end

U_total = 2 * sum(U);
Leq_leak = 2*U_total;

%-------------------------------------------------------------------------------------
% Solve for Lmag, Llp, Lls
%-------------------------------------------------------------------------------------

% Unfortunately, the estimation method used to find the open circuit inductance
```

```
% does not include any leakage components.  This can be seen by the fact that the
% same process performed from the secondary side to find Lopen modifies the result
% by exactly TRatio^2, not TRatio^2 plus some leakage adjustment.  Thus, Lopen using
% this method corresponds to only Lmag, and we have no method of separating Leq_leak
% into its two components.

% Instead, we'll just divide by 2 and accept the fact that for non-unity turns ratios
% the accuracy of the answer goes down.

Lmag_DC = Lopen_DC;
Lmag_AC = Lopen_AC;
Lleak   = Leq_leak/2;
disp('  Lmag_DC   Lmag_AC    Lleak')
disp([Lmag_DC*1e+6,Lmag_AC*1e+6,Lleak*1e+6])

%-------------------------------------------------------------------------------------
% Resistance Calculations
%-------------------------------------------------------------------------------------

% Estimate the DC resistance based on # of turns and resistance per turn

R_DC1 = 2*pi*rho_cu / (C_T * log(OW_R/IW_R));
R_pmy_DC = R_DC1 * PTurns;
R_sdy_DC = R_DC1 * STurns;
disp('  R_pmy_DC  R_sdy_DC');
disp([R_pmy_DC,R_sdy_DC]);

% AC Calculations
        % Each turn experiences self-induced eddy currents
        % Proximity effects are assumed to be only within the driven conductor

sd_foil = sqrt((2*rho_cu)/(w*mu0));
x = C_T/sd_foil;
K_skin = (sinh(2*x) + sin(2*x))/(cosh(2*x) - cos(2*x));
K_proximity = (2*sinh(2*x) + 2*sin(2*x) - 4*cos(x)*sinh(x) - 4*sin(x)*cosh(x))/(cosh(2*x) - cos(2*x));
proximity_sump = sum([1:PTurns-1].^2);
proximity_sums = sum([1:STurns-1].^2);

R_pmy_AC = R_DC1 * x * (K_proximity*proximity_sump + K_skin*PTurns);
R_sdy_AC = R_DC1 * x * (K_proximity*proximity_sums + K_skin*STurns);

disp('  R_pmy_AC  R_sdy_AC');
disp([R_pmy_AC,R_sdy_AC]);
```

Bibliography

[1] Esser, A., and Skudelny, H. "A New Approach to Power Supplies for Robots." *IEEE Transactions on Industry Applications*. Vol 27, No. 5, 1991. pp. 872-875.

[2] Severns, R., Yeow, E., Woody, G., Hall J., and Hayes, J. "An Ultra-Compact Transformer for a 100 W to 120 kW Inductive Coupler for Electric Vehicle Battery Charging." *IEEE PESC*. IEEE, 1996. pp. 32-38.

[3] Esser, A. "Contactless Charging and Communication System for Electric Vehicles." *IEEE Industry Applications Society Annual Meeting*. October, 1993.

[4] Kelley, A., and Owens, W. "Connectorless Power Supply for an Aircraft-Passenger Entertainment System." *IEEE Transactions on Power Electronics*. Vol. 4, No. 3, July 1989, pp. 348-354.

[5] Divan, D., Klontz, K., Lorenz, R., and Novotny, D. "Contactless Power Delivery System for Mining Applications." *IEEE Industry Applications Society Annual Meeting*. October 1991. pp. 1263-1269.

[6] Lashkari, K., Shladover, S., and Lechner, E. "Inductive Power Transfer to an Electric Vehicle," *8th International Electric Vehicle Symposium*. Oct. 1986, pp.258-267.

[7] Kutkut, N., Divan, D., Novotny, D., and Marion, R. "Design Considerations and Topology for a 120 kW IGBT Converter for EV Fast Charging," *IEEE PESC*. 1990. pp. 238-244.

[8] Electronics Transformer Technical Committee of the IEEE Magnetics Society. *An American National Standard: IEEE Standard for Pulse Transformers*. 1987.

[9] Connelly, F.C. *Transformers: Their Principles and Design for Light Electrical Engineers*. London: Sir Isaac Pitman & Sons, Ltd., 1950.

[10] Staff of the MIT Department of Electrical Engineering. *Magnetic Circuits and Transformers*. Cambridge: The MIT Press, 1943.

[11] Grossner, N. *Transformers for Electronic Circuits*. New York: McGraw-Hill Book Co., 1967.

[12] Slemon, G. *Magnetoelectric Devices: Transducers, Transformer, and Machines*. New York: John Wiley & Sons, Inc., 1966.

[13] Kirtley, J. "On Turbine-Generator Rotor Equivalent Circuits." *IEEE Power Engineering Society Meeting.* 1993.

[14] Snelling, E., and Giles, A. Ferrites for Inductors and Transformers. New York: John Wiley & Sons, Inc. 1983. p 31.

[15] Goldberg, A. *Development of Magnetic Components for 1-10 MHz DC/DC Converters.* MIT ScD. Thesis, EECS Department. 1988

[16] SAE Electric Vehicle Inductive Coupling Recommended Practice - SAE Document J-1773, Draft 5.2, February 1, 1995.

[17] Riezenman, M., and Wouk, V. "EV Watch." IEEE Spectrum, September 1995. pp. 72-75.

[18] Staelin, D., Morgenthaler, A., and Kong, J. *Electromagnetic Waves.* New Jersey: Prentice Hall, 1994.

[19] Dai, N. and Lee, F. "Design of a High Density Low-Profile Transformer." *IEEE APEC.* 1996. pp. 434-440.

Related Reading:

Mweene, L., Otten, D., and Schlecht, M. "A High-Efficiency 1.5 kW, 390-50 V Half-Bridge Converter Operated at 100% Duty-Ratio." IEEE APEC Proceedings, 1992. pp. 723-730.

Sakamoto, H., and Harada, K. "A Novel High-Power Converter for Non-contact Charging with Magnetic Coupling." IEEE Transactions on Magnetics, 1994. pp. 4755-4757.

Heeres, B., Novotny, D., Divan, D., and Lorenz, R. "Contactless Underwater Power Delivery." IEEE PESC, 1994. pp. 418-423.

Klontz, K., Esser, A., Wolfs, P., and Divan, D. "Converter Selection for Electric Vehicle Charger Systems with a High-Frequency High-Power Link," IEEE PESC, June 1993. pp. 855-861.

Kassakian, P. "Design and Testing of A Mechanical Arm for Use with Polymer Gel Muscles," MIT S.B. Thesis in Mechanical Engineering, May 1995.

Kheraluwala, M., Novotny, D., and Divan, D. "Design Considerations for High Power High Frequency Transformers," IEEE PESC Conference Record 1990, pp. 734-742.

Rauls, M., Novotny, D., and Divan, D. "Design Considerations for High Frequency Co-Axial Winding Power Transformers," IEEE Industry Applications Society 1991 Conference Record, pp. 946-952.

Wiegman, H., Divan, D., Novotny, D., and Mohan, R. "A ZVS Dual Resonant Converter for Battery Charging Applications," IEEE PESC 1991. pp. 202-208.

Barnard, J., Ferreira, J., van Wyk, J. "Optimising Sliding Transformers for Contactless Power Transmission Systems," IEEE PESC 1995. pp. 245-251.

Schoenung, S., Bieri, R., and Meier, W. "Energy Storage Options for Electric Vehicle Recharging Stations," Electric Vehicle Power Systems: SAE-SP984. pp. 44-47.